Effect of Age on the Mechanical Behavior and Molecular Structure of Human Meniscus:

An Experimental and Computational Analysis.

by

Derek Q. Nesbitt

A dissertation

submitted in partial fulfillment

of the requirements for the degree of

Doctor of Philosophy in Biomedical

Engineering Boise State University

August 2023

BOISE STATE UNIVERSITY GRADUATE COLLEGE

DEFENSE COMMITTEE AND FINAL READING APPROVALS

of the dissertation submitted by

Derek Quentin Nesbitt

Dissertation Title:	Effect of Age on the Mechanical Behavior and Molecular Structure of Human Meniscus: An Experimental and Computational Analysis.
Date of Final Oral Examination:	01 May 2023

The following individuals read and discussed the dissertation submitted by student Derek Quentin Nesbitt, and they evaluated the student's presentation and response to questions during the final oral examination. They found that the student passed the final oral examination.

Trevor J. Lujan, Ph.D.	Chair, Supervisory Committee
Clare Fitzpatrick, Ph.D.	Member, Supervisory Committee
Gunes Uzer, Ph.D.	Member, Supervisory Committee
Julia Oxford, Ph.D.	Member, Supervisory Committee
Tracye Lawyer, M.D, Ph.D.	Member, Supervisory Committee

The final reading approval of the dissertation was granted by Trevor J. Lujan, Ph.D., Chair of the Supervisory Committee. The dissertation was approved by the Graduate College.

DEDICATION

I would like to dedicate this dissertation to my parents: Nancy, Bob, Kevin, and Sarah for their everlasting support. I also dedicate this work to my close friends and siblings: Cody, Josh, Alex, and Patrick for only *occasionally* deriding me for spending 15 years in school. I dedicate this dissertation to my lovely girlfriend Mytch, who helped me to focus and accelerate publication time lines to the end. Finally, I dedicate this work to Bill Nye the science guy, whose TV show taught me the scientific method while inspiring a young and inquisitive mind.

ACKNOWLEDGMENTS

I would like to acknowledge the other students who assisted with this research: Danielle Siegel, Zach Pinkley, Sean Nelson, Miranda Nelson, Dylan Burruell, Bradley Henderson, and Matthew Turner. I also acknowledge the Pirates of the Caribbean musical score for providing the soundtrack to most of the writing work contained herein, just as it did for my Masters thesis. Additionally, I would like to acknowledge my fellow graduate students who were not directly involved with this work, but provided a good sounding board and opportunities to commiserate the struggles of life as a graduate student: Maddie Wale, John Everingham, Kate Benfield, Amevi Semodji, and Scott Birks. I would also like to acknowledge several Boise State staff members who supported this work, including: Kyle Shannon, Shin Pu, Laura Bond, Julia Oxford, and Annamaria Zavala. Lastly, I would like to acknowledge my advisor, Trevor Lujan, who gave me the opportunity and support to do this work.

ABSTRACT

The knee meniscus is a soft fibrous tissue with a high incidence of injury in older populations. Surgical treatments do not fully restore the functionality of the meniscus, and the meniscus lacks native healing capacity, leading to a 40% increase in the probability of developing osteoarthritis once torn. Meniscus injury prevention is thus paramount to reducing the onset of osteoarthritis. Despite the importance of the meniscus in joint health, its mechanical properties, and how these change with age, are poorly understood. In order to quantify these properties, and how they change with age, we performed uniaxial tensile tests on two age groups of human menisci: under 40 and over 65 years old. We found that tissue from the older donor groups had significantly reduced strength and toughness. We refined the data analysis techniques used in this work to build a free web application to provide to the scientific community to standardize the calculation of mechanical properties found in soft tissue tensile testing, and to provide a convenient tool to reduce the time to analyze data. We then used the mechanical testing data to build and validate a finite element model of tissue failures with continuum damage mechanics. This work showed that using von Mises stress to evolve damage produced excellent fits to the experimental data, and was able to mimic the failure behavior from the previous experiments. Finally, we performed biochemical analysis on the tissue in order to evaluate the changing structure-function relationship with age. This showed changes to the meniscus proteome with age, and that changes to collagen crosslinks correlated to changes to the strength of the tissue. Collectively, this work has

detailed potential reasons as to how and why the meniscus becomes more susceptible to tears with age, detailed computational methods to analyze these tears, and provided a tool to further analyze tears of the meniscus and other soft tissues in a lab setting.

TABLE OF CONTENTS

LIST OF TABLES

LIST OF FIGURES

CHAPTER ONE: INTRODUCTION

1.1 Motivation

The knee meniscus is one of the most frequently torn soft tissues in the body, with more than a half-million surgeries performed in the U.S. annually [1]. Once torn, the capability of the meniscus to attenuate loads and stabilize the knee can become permanently compromised. This leads to a 40% increase in risk of developing osteoarthritis[2], a painful swelling of the knee joint that can cause a loss of mobility[3], which effects approximately 10% of all U.S. adults by age 60[4]. The meniscus has little ability to heal once torn, and surgical interventions are unable to restore the native function due to limited vasculature[5]. The lack of treatment options for meniscus tear injuries makes prevention of the utmost importance in combatting osteoarthritis.

One important step in tear prevention is the understanding of the structural cause, and mechanical effect, of age-related changes to tear incidence. While studies of the mechanical properties of human meniscus exist[6–8] , no study has evaluated the changes to human meniscus mechanical properties due to age. This information is needed to understand the potential mechanisms behind the increase of tear injury with age. By showing how the different mechanical properties change as we age, we begin to understand the mechanisms behind an increased tear incidence, and clinicians may be better informed to design strategies to help patients reduce tear risk.

Tissue mechanical properties are directly related to the underlying structural composition, and therefore a key aspect to understanding the cause of age-related changes in meniscal tear probability is the quantification of how the structural composition changes with age. Previous research has shown a reduction of vasculature of the meniscus with age[5], but no other study has evaluated how the structure changes on the molecular level. Once we have identified structural changes with age, therapeutic strategies may be designed to combat or prevent these changes.

The use of computational tools like finite element analysis (FEA) can be utilized to help inform the development of meniscus tear prevention therapies, similar to what has been done to inform patient specific aortic aneurysm[9] or ACL tear risks[10]. However, the calibration and validation of an appropriate constitutive framework requires model comparisons to experimental data[11], and experimental data highlighting failure behavior is lacking. By developing and validating these computational models, more refined models can be built to evaluate the meniscus within the joint, and study the different loading configurations that lead to an increased risk of sustaining an injury. This may help clinicians and athletes understand high risk movements, and design ways to avoid or mitigate the risk posed by these movements.

There also exists no standardized method to evaluate certain mechanical properties in soft fibrous tissues. Methods to calculate properties of interest differ across research groups[12–14], creating the potential of increasing variability in reported mechanical properties. Providing an automated tool to assist the standardization of these calculation methods could aid in reducing variability of mechanical properties reported group-to-group, as well as decrease the time and computational burden that can be required to analyze complex tensile data of soft tissues without linear stress-strain curves.

1.2 Research Goals

The overall objective of this research was to quantify the effect of age on the human meniscus. Once completed, this body of work is expected to further our understanding of the mechanisms behind the increase of meniscus tear injuries with age. This understanding is pivotal to the design of interventions and therapies to reduce the prevalence of this debilitating injury within the population. This work will also further the general understanding of the mechanical environment of the knee by better defining the mechanics of the meniscus. These research objectives were met by utilizing experimental and computational techniques: by assessing the biomechanical properties and biochemical makeup of human lateral meniscus tissue, as well as mathematically modelling the failure behavior of both young and older tissue relative to the reinforcing fiber network. Additionally, we provide an automated tool to the scientific community to aid in standardizing the evaluation of biomechanical properties of soft fibrous tissues.

1.3 Summary of Chapters

The mechanics of tissue tears are investigated and described before evaluating the biochemical structure of the tissue. The purpose of Chapter 2 was to provide sufficient background information pertinent to the remaining chapters. This background information includes an overview of the structure of the meniscus and its role in the knee joint, along with injury demographics and pathology. This structural description includes macroscale detail of the tissues normal function, as well as the microscale composition.

In order to describe the changes of meniscus biomechanics with age, as well as characterize the mechanics of tissue tears, a novel experimental technique was developed and described in Chapter 3. This technique measures the full-field strains on a sample surface while undergoing tensile pull to failure testing, giving the orientation and magnitude of tear region strains. The anisotropic tear mechanics and tensile mechanical properties were evaluated relative to donor age group. Half of the experiments described in this chapter were conducted when I was pursuing my MS, so the work in this chapter is not entirely from my PhD.

Chapter 4 describes the development of a free, web-based application for analyzing soft tissue tensile curves. The computational algorithms developed to analyze the mechanical data in Chapter 3 were quite robust, and can help to establish the standards for evaluating soft tissue tensile curves which are lacking. The publication of this web application stands to reduce the variability of analysis between research cohorts, and reduce the time investment required to analyze data thoroughly.

The mechanics of tissue tears from Chapter 3 were also used to inform the development of a finite element model in Chapter 5. This model was calibrated to the tensile stress-strain character of the tissue, and validated against the tear region strains measured from Chapter 3. This was the first model to describe failures of meniscus tissue, and provides needed detail towards improving knee analysis models.

Chapter 6 then evaluates the structural composition of the tissue that was mechanically tested in Chapter 3. This includes characterization of the extracellular matrix proteins, as well as measuring crosslinks between the collagen fibers, which have been theorized to increase with age and adversely affect tissue mechanics[15]. These age-related changes to the biochemical makeup of the tissue are then compared to the changing mechanics with age. This narrows down the potential molecular level changes that could result in changes to the mechanics of the tissue.

The final chapter reviews the contributions this research has made to the field of soft tissue mechanics, as well as comments on the future work that is needed to expand on this research. The desired outputs from each study objective and how each project is connected is outlined in Figure 1.

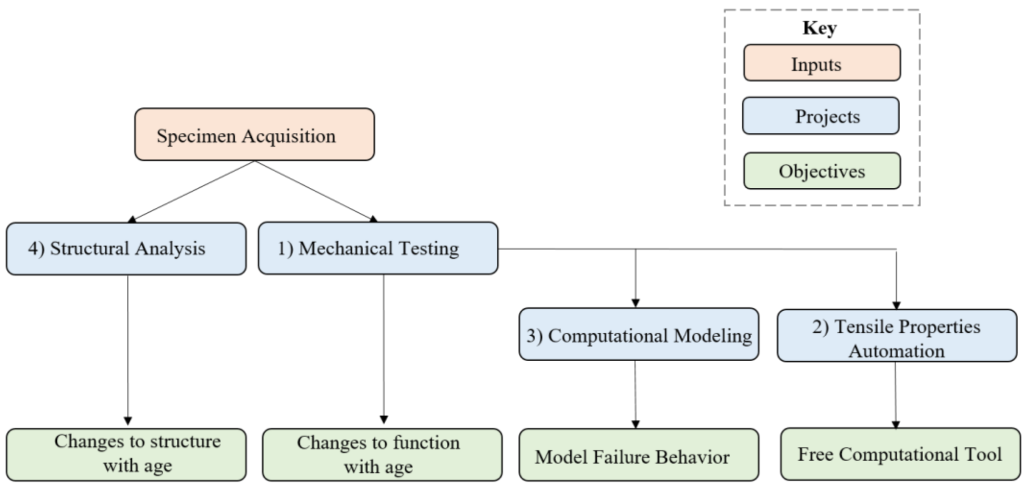

Figure 1: The required inputs and desired outputs from each of the projects covered in this dissertation.

CHAPTER TWO: BACKGROUND

2.1 Meniscus Structure and Tear Etiology

The meniscus is a soft tissue of the knee, that resides distally to the femur and proximal to the tibia, between the femoral condyles and the tibial plateau (Figure 2). There are two menisci in each knee, the lateral and medial meniscus, associated with each of the femoral condyles. The knee meniscus is one of the most frequently torn soft tissues in the body, with more than a half-million surgeries performed in the U.S. annually.[1] Once torn, the capability of the meniscus to attenuate loads and stabilize the knee can become permanently compromised. This leads to a 40% increase in risk of developing osteoarthritis,[2] a painful swelling of the knee joint that can cause a loss of mobility,[3] which effects approximately 10% of all U.S. adults by age 60.[4] The meniscus has little ability to heal once torn, and surgical interventions are unable to restore the native function due to limited vasculature.[16] The lack of treatment options for meniscus tear injuries makes prevention of the utmost importance in combatting osteoarthritis.

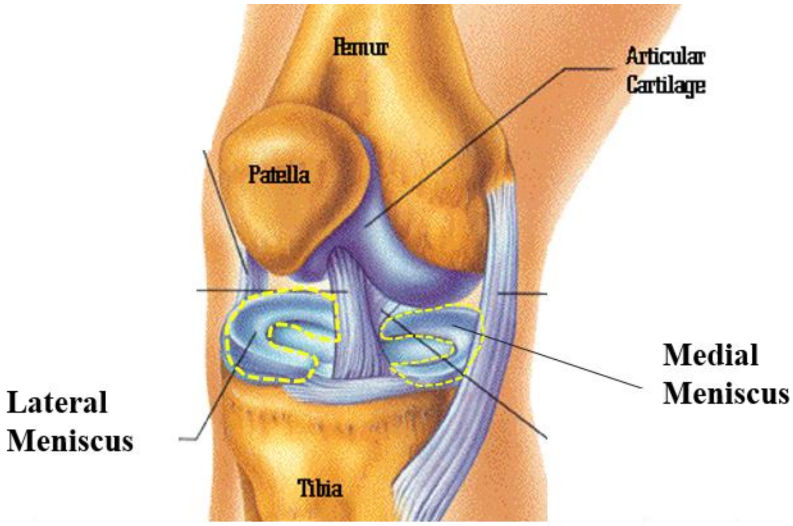

Figure 2: Location of the medial and lateral meniscus within the human knee joint.

The meniscus itself is a fibrous soft tissue, comprised of a hydrated proteoglycan rich ground substance reinforced by a primarily circumferentially aligned collagen type 1 fiber matrix.[17] Tears of the menisci are classified by their shape relative to this fiber matrix (Figure 3).[18] Vertical tears occur between the fibers and may be caused by tensile loads occurring perpendicular or transverse to the circumferential fibers (Figure 3A). These tears can progress to bucket handle tears that obstruct joint articulation (Figure 3B). Radial tears occur across the fibers and are caused by hoop stresses that create tensile loads longitudinal to the circumferential fibers (Figure 3C). Radial tears can obstruct joint articulation once a flap forms in the shape of a parrot beak type tear (Figure 3D). Interestingly, the meniscus becomes more susceptible to tear injuries with aging,[19,20] and radial tears longitudinal to the fibers become more common in patients over the age of 50.[18,21] However, whether the effect of age on meniscus injury epidemiology is due to age-related changes in mechanical properties, or other physiological factors, has yet to be elucidated.

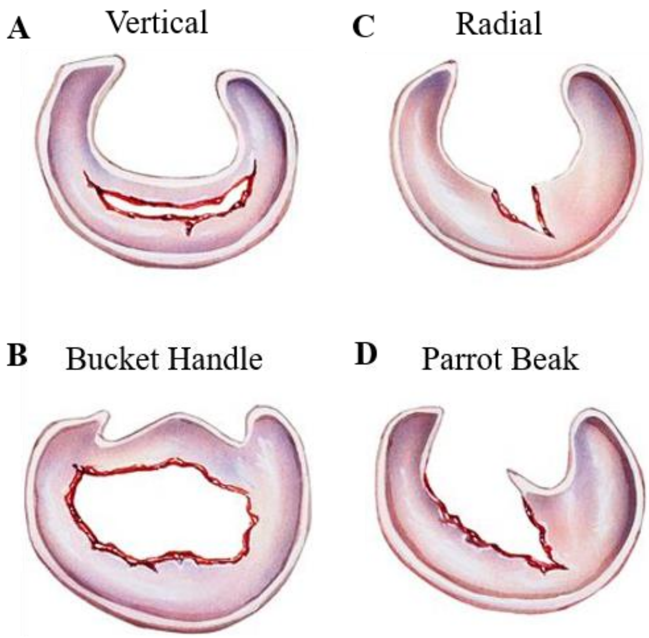

Figure 3: Meniscus tear types, including A) vertical tears between the fibers which can progress to B) bucket handle tears, as well as C) radial tears which can progress to complex D) Parrot beak tears.

2.2 Mechanical Characterization

Previous work in mechanical testing of human meniscus is limited. The work by Tissakht and Ahmed[7] was one of the most comprehensive of these studies, which measured a wide variety of the anisotropic tensile mechanical properties of meniscus tissue, both along the reinforcing fibers, and perpendicular to them. Other previous research has covered a narrower scope of mechanical behavior, like a specific mechanical property,[22–24] the effects of degeneration,[25] effects of sample preparation,[26] or comparisons to other species menisci.[27] While some of these studies compared the differences of mechanical properties relative to the fiber network,[7,23,24] none of these previous studies commented on the failure plane of the tissue to inform failure criteria for computational modeling.

Research on the effect of age on meniscus is lacking as well, with only a single previous study that evaluated the effect of age on the tensile behavior of the human meniscus.[28] However, this study evaluated only the change of tensile modulus over a very limited age range of under 45. This singular previous study ultimately found no significant change in this age range, but the limited scope was insufficient for capturing the potential changes in mechanical performance due to age. The effect of age has been successfully measured in other similar tissues. Articular cartilage, for example, is a tissue in direct contact with the meniscus and has shown reduced mechanical strength due to age.[29] A number of other soft fibrous tissues of the body have also shown reduced mechanical properties with age, including: soft tissues of the human spine,[30] various tendons,[31–33] and the anterior cruciate ligament (ACL).[34] These studies regarding other soft fibrous tissues suggest that a wide variety of mechanical properties should be examined when trying to measure the effect of age on mechanical performance.

2.3 Computational Modeling of Soft Tissues

Previous studies have used computational models to predict failure in soft tissue, but not in the meniscus. Patient specific models of the ascending aorta have been utilized to determine patient risk of aortic aneurysm based off of physiological characteristics, like systolic pressure.[9] A similar approach with finite element modeling was used to assess the risk for ACL tears in patients using geometry obtained from MRI and evaluating their natural gait.[10] Studies like these that assess injury risk require validated models regarding the failure behavior of the tissue of interest, such has been done for both the aorta and ACL.[35,36] No validation study yet exists for the human meniscus, and in fact, models that exist of the human meniscus seem to primarily focus on the stresses across the structure within the knee joint, and disregard any kind of failure behavior.[37–39] While these studies can help to inform motions that increase tear risk of the meniscus due to increased stress, they fail at being able to identify when, or how, a meniscus tear injury could occur.

Continuum damage mechanics (CDM) models have been used to describe the failure of a wide variety of similar fibrous soft tissues in previous research, including non-specific formulations for any soft tissue with fibers,[40–42] as well as specific soft fibrous materials, like ligaments,[43] tendon,[44] and rectus sheath tissue.[45] The selection of proper model formulations for a tissue can be informed by understanding material isotropy, the type of loading, and what stresses govern failure.[46] By using DIC to identify the failure plane during mechanical testing, we identify the appropriate failure criteria to implement into a potential model. The rising popularity of digital image correlation in research has also led some groups to recognize the method's potential for validating models.[47,48] By tuning model parameters to load frame tensile data, then comparing model output of surface strain distribution to experimentally measured strain distribution by DIC, there exists the potential to calibrate and validate a computational model with the same group of experiments.

2.4 Structure-Function Analysis

Changes to soft tissue mechanics with age have been previously documented, including the reduction of mechanical properties in cartilage,[49] tendons,[50] and ligament.[34] The structural mechanisms behind the changes in some of these tissues have also been explained. For example, an age-related shift in the structural proteins making up the extra-cellular matrix of articular cartilage results in tissue that is less durable to mechanical stress.[51] Similarly, the increased stiffness of human aortic tissue has been linked to a reduction of the structural protein elastin and an increase of collagen fibers.[52] It is not just the changing of structural proteins that can cause changes to these tissues, however. Tissues rich in collagens type 1 and 2 are susceptible to non-enzymatic oxidative reactions with glucose, which form advanced glycation end-products (AGE's).[53] These bind to amino groups of the collagen, forming crosslinks that alter the mechanics of the collagen itself, as well as dramatically modifying their interaction with other molecules, such as proteoglycans and integrins.[54] One such AGE is pentosidine, which has been shown to accumulate in meniscus with age[55] and has also been seen to decrease the mechanical performance of similar tissues.[56–58] While a natural increase of the AGE pentosidine has been observed in human meniscus tissue,[55] no study has quantified the changes in collagen crosslinking and structural proteins, and related them to mechanical changes with age.

2.5 Data Analysis of Tensile Mechanical Properties

Different methods for calculating certain mechanical properties of fibrous soft tissues exist across different research groups. While definitions of the phenomena being described for these points exist, there is not yet a standardized method for identifying them when performing a tensile test. The transition point represents the straightening of collagen fibers preceding the approximately linear elastic response of the tissue, but is found in a number of different ways across research groups, including the utilization of bimodal fitting algorithms[14,59] or a set percentage of deviation from the linear region.[12,60].Similarly, the yield point, representing the onset of tissue damage ending the approximately linear region has been determined using set deviations from the linear region,[12] the point of maximum slope of the linear region,[13] or by inflection points identified by the first derivative of cubic fits to the data.[6] All of these different calculation schemes are done using in-house custom coding in a variety of programs, specific to individual research groups. While the methods being utilized are published, the programs themselves are not. This combination of non-standardized methods for calculating points, and lack of transparency of coding methods could be partially responsible for the wide deviation of reported mechanical properties that exists between research groups.

CHAPTER THREE: Effect of age on the failure properties of human meniscus: High-speed strain mapping of tissue tears.[1]

3.1 Introduction

The knee meniscus is a soft fibrous tissue that provides joint stability and helps protect the articular cartilage by distributing and attenuating forces across the tibiofemoral joint[61,62]. Due to large and repetitive joint loads, the meniscus is frequently torn, and as a result, a half-million meniscus surgeries are performed annually in the U.S. to alleviate pain and joint instability[1]. Moreover, with aging, the meniscus becomes more susceptible to injury by tearing[19,49,63]. Understanding the failure mechanisms of meniscus, and how age influences this behavior, is relevant to advancing the prevention and treatment of meniscus injuries in both young and older populations.

Meniscus tear injuries are dependent on a combination of factors including loading condition, joint geometry, and the composition and organization of the extracellular matrix. The meniscus is composed of a collagen type I fiber matrix, embedded in a hydrated ground substance. This anisotropic fiber network is primarily aligned circumferentially to resist the tensile or hoop stresses that develop in the semi-circular meniscus during joint compression[64]. Meniscus tears can either disrupt the circumferential fibers (e.g. radial and flap tears) or propagate alongside the fibers (e.g. horizontal and vertical tears). The distribution of these tear patterns in the medial and lateral meniscus is influenced by age[18], however, it is unknown whether the effect of age

---

[1] Reprinted from *Journal of Biomechanics* Vol 115 Nesbitt, D. Q., Siegel, D. N., Nelson, S. J., and Lujan, T. J. "*Effect of Age on the Failure Properties of Human Meniscus: High-Speed Strain Mapping of Tissue Tears,"* pp 110-126, 2021.[91]

on injury epidemiology is due to age-related changes in the mechanical properties of the meniscus, or is due to other physiological factors.

To accurately measure the tensile failure properties of meniscus, tissue deformation must be quantified within the localized tear region. While previous meniscus studies have measured local tissue strains during tensile loading[6,7,25,65], the instantaneous tissue strains occurring within the tear region of meniscus have not been reported, nor has the angle that tears propagate when loaded in tension. The angle of tear propagation relates to the physical mechanism of failure, and can inform mathematical models that predict failure behavior[66]. An experimental method to quantify local tissue strains, and identify tear propagation, is digital image correlation (DIC). This technology can measure full-field strains on the specimen surface, and evaluate failure properties of interest, including the 1st principal and maximum shear strains along the tear, which can help define failure mechanisms in ductile and brittle materials[46,67]. By pairing DIC with high-speed video, strains can be measured within the tear region at nearly the exact moment when tissue begins losing the capacity for load-bearing.

The objective of this study was to determine the effect of age on the anisotropic tensile failure properties in the human meniscus. We hypothesize that 1) meniscus extensibility decreases with age, and 2) meniscus tears occur near the plane of maximum shear stress.

3.2 Methods

3.2.1 Overview

The failure properties of young and older human lateral menisci were measured with the circumferential fibers oriented either parallel or perpendicular to the loading axis. Local strain magnitudes in the tear region were quantified at points of interest along the stress-strain curve using two-dimensional DIC.

3.2.2 Specimen Preparation

Lateral menisci were obtained from 10 unpaired human fresh frozen cadaveric knee joints (femur to tibia), with five knees from young donors under the age of 40 (age = 33±5 years; 3 male and 2 female), and five knees from older donors over the age of 65 (age = 72±7 years; 4 male and 1 female). All knees had no medical history of injury and the meniscus had no degenerative fraying or other signs of damage, but many of the older specimens had yellow discoloration[68]. Menisci were harvested, sectioned into anterior and posterior regions[25], packed in CelluClay, and frozen for at least 24 hours prior to being layered along the circumferential-axial plane into ~0.8 mm thick specimens using a deli slicer[13,69]. After layering, specimens were cut into dumbbell-shaped coupons (Figure 4A) by aligning the long-axis of a custom punch[70] along the circumferential fiber direction (longitudinal group) or perpendicular to the circumferential fiber direction (transverse group). To quantify the mean fiber orientation relative to the loading axis (Table 1), light microscopy images of the tensile coupons were captured after punching (Figure 4B), and were analyzed with FiberFit software[71]. A total of 40 specimens were tested and analyzed, with four sets of ten specimens representing unique combinations of

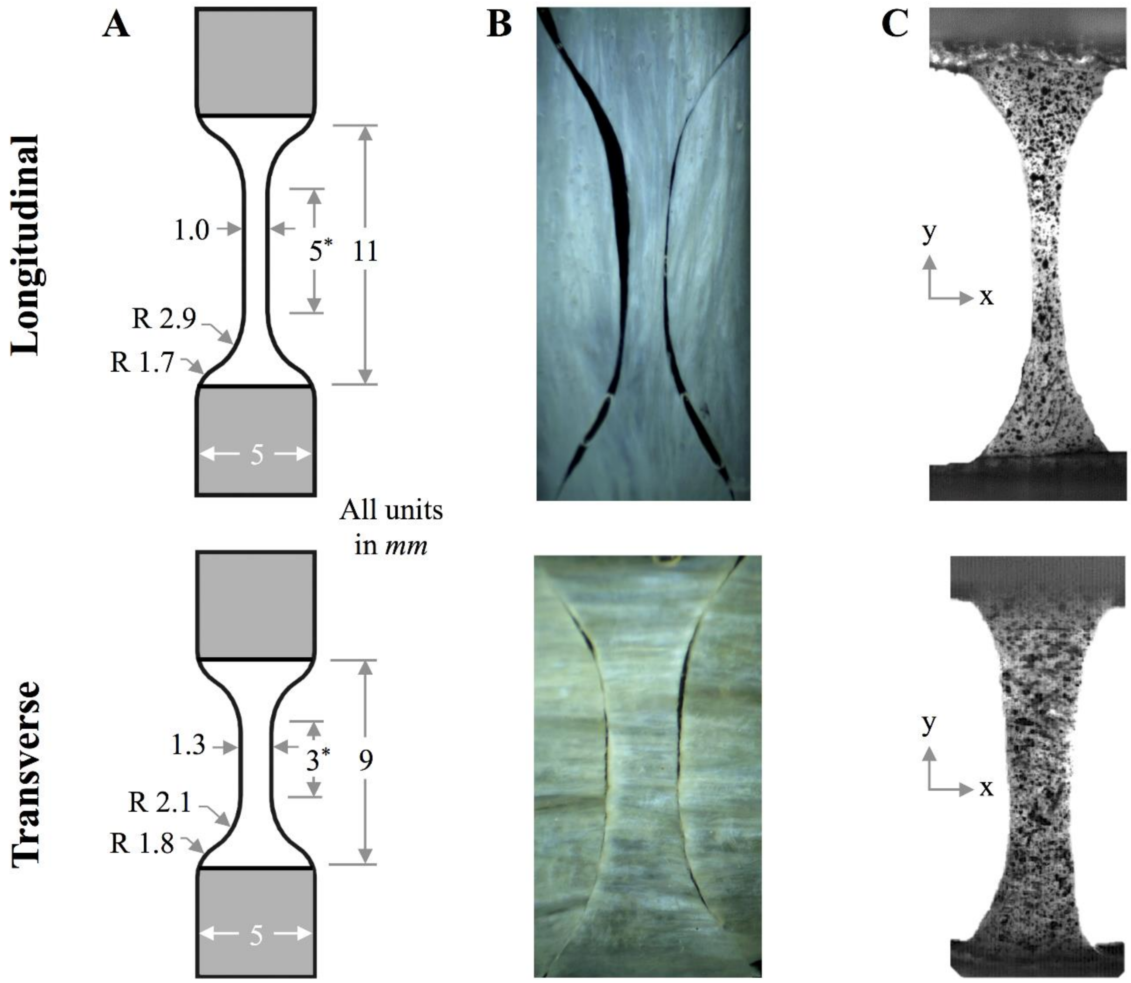

Figure 4: Longitudinal and transverse tensile specimens from human meniscus. A) Dimensions of dumbbell coupons in mm (gray = region being gripped, * = gauge section). B) Light microscopy of tissue coupons captured the visible fiber orientation prior to mechanical testing. The mean fiber orientation was quantified using FiberFit software. C)Specimens with a sprayed speckle pattern for DIC analysis.

age (young, older) and fiber orientation (longitudinal, transverse). Each testing set was equally composed of specimens from the posterior and anterior regions, where the five specimens from each region were acquired from at least four different cadavers.

Specimens were prepared for mechanical testing by gluing emery cloth tabs to the specimen grip section to reduce slipping, and by applying a random speckle pattern of black India ink (Figure 4C) using an airbrush set to 15 psi at a spraying distance of 27.5 cm. The Shannon entropy[72] of each speckle pattern was calculated to estimate speckle quality. Specimens tested in this study had an average Shannon entropy of 4.8 ± 0.3, a moderate value.

Table 1: Physical characteristics of meniscus tensile test specimens

Fiber Orientation	Age Group	Width[a] (mm)	Thickness[a] (mm)	Cross-Sectional Area[a] (mm^2)	Grip-to-Grip Length (mm)	Mean Fiber Orientation[b] (deg)
Longitudinal	Young	1.08 ± 0.12	0.73 ± 0.09	0.79 ± 0.13	10.65 ± 0.90	2.6 ± 3.7
	Older	1.08 ± 0.13	0.70 ± 0.15	0.76 ± 0.22	11.20 ± 1.2	2.4 ± 2.3
Transverse	Young	1.41 ± 0.19	0.80 ± 0.15	1.15 ± 0.31	6.20 ± 1.34	89.1 ± 3.7
	Older	1.45 ± 0.14	0.81 ± 0.21	1.18 ± 0.37	6.95 ± 1.77	90.8 ± 6.3

[a] Measured in the gauge section
[b] Measured relative to the loading axis

3.2.3 Tensile Mechanical Testing

All mechanical tests were conducted using an electrodynamic test system (Instron, Norwood MA, USA; ElectroPuls E10000). Specimens were preloaded, mechanically preconditioned for 20-cycles (triangle wave, 8% strain, 1 Hz), and then preloaded again to remove laxity (preload = 0.1 N for longitudinal, 0.03 N for transverse). Front and side digital images were taken to measure gauge width and thickness (Table 1)[69].

Specimens were pulled to failure in tension at a rate of 1% strain/second while filming at 500 frames per second (fps) using a high-speed camera (Photron, Tokyo, Japan; fastcam mini UX50; resolution = 50 pixels/mm), polarized lenses, and an LED floodlight (Energysaver LED, St. Louis, MO; PHSI3060-120W)(Figure 5). During testing, specimens were kept moist by spraying with 0.9% saline solution. Each test was

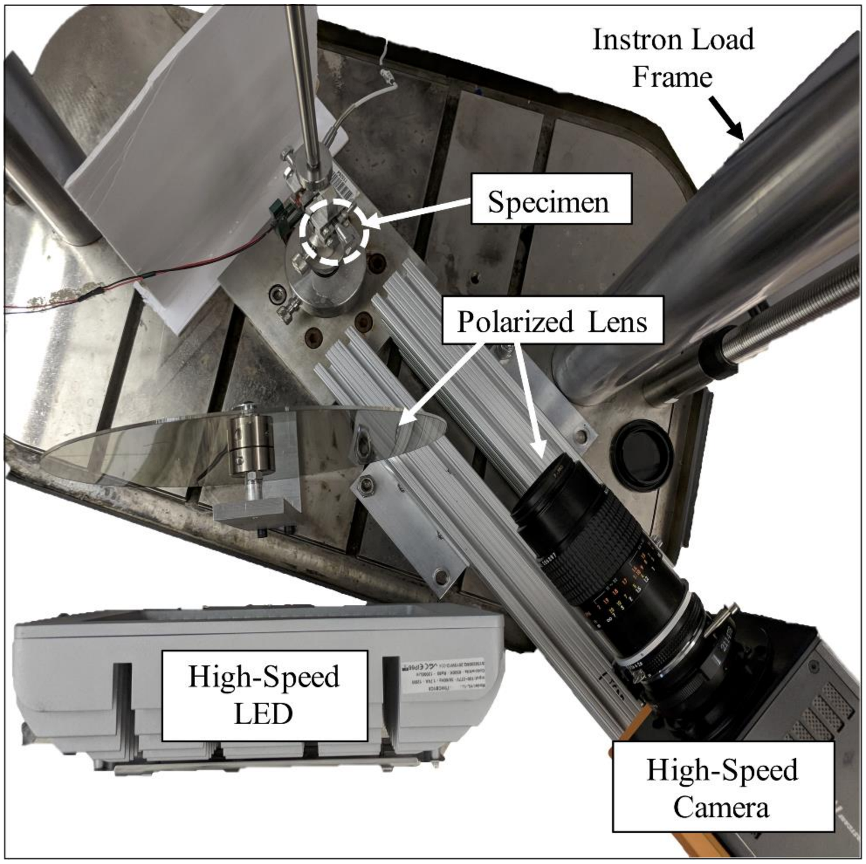

Figure 5: Top view of the tensile test setup for high-speed measurement of full-field strain. In order to minimize glare on the specimen surface, two polarized lenses were positioned between the LED and camera with polarization angles in 90° opposition to each other.

prescribed one of five failure modes (Figure 6): midsubstance, fillet, multimode, grip, or slip. Specimens with a grip or slip failure were excluded from further analysis.

The axial force and displacement at the grips were converted to engineering stress (1st Piola-Kirchoff) and engineering strain[73]. Stress-strain curves for the longitudinal group were split into three regions[6] with four points of interest (Figure 7A): transition, yield, ultimate, and rupture. The transition point represents the straightening of the

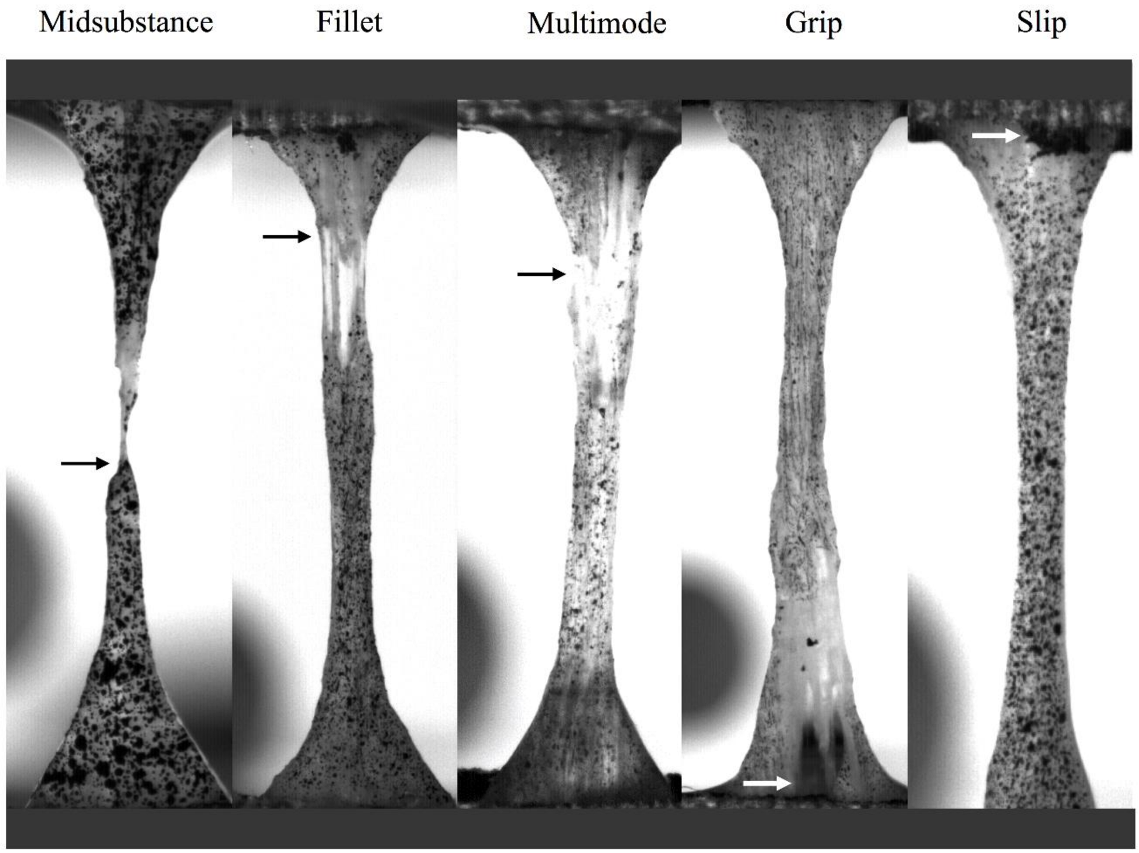

Figure 6: Different failure modes classified in this study, with arrows indicating the location of tear initiation. Midsubstance failures (n = 6 longitudinal, n = 18 transverse) had tears inside the gauge section, while fillet failures (n = 9 longitudinal, n = 2 transverse) had tears at the radius of the width tapered region. Multimode failures had tears that initiated in either the midsubstance or fillet and propagated to the grip (n = 5 longitudinal, n = 0 transverse). Grip failures (n = 29 longitudinal, n = 11 transverse) had tears along the grip line and slip failures (n = 7 longitudinal, n = 0 transverse) occurred when the specimen slipped at the grip interface prior to tissue rupture. The white arrow forthe slip failure shows the black residue from the emery cloth that detached from the grip interface. Grip and slip failures were discarded and excluded from further analysis.

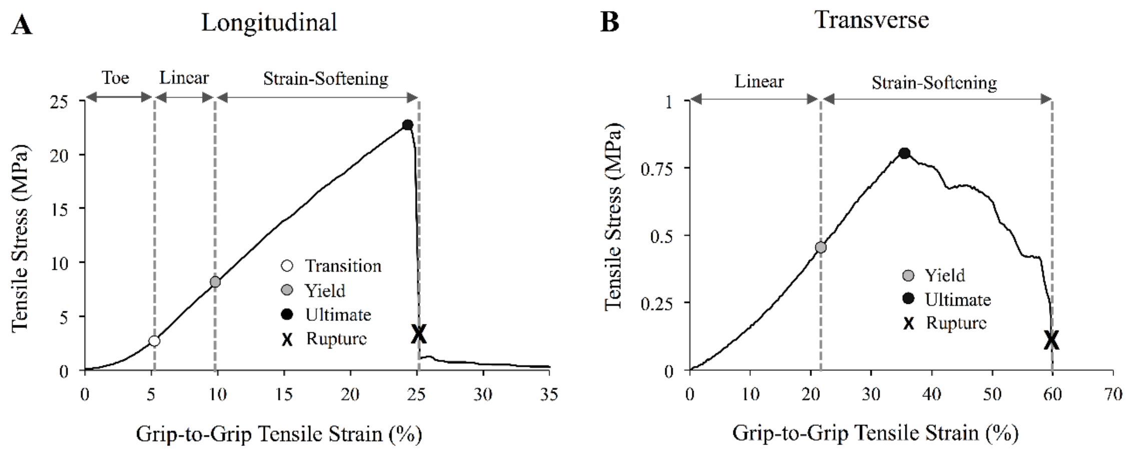

Figure 7: Representative stress–strain curve for a A) longitudinal and B) transverse specimen with marked points of interest (transition, yield, ultimate, rupture). Grip-to-grip tensile strain was measured as the grip displacement divided by the grip-to-grip reference length.

crimped collagen fibers, the yield strength may indicate where damage accumulation begins to soften the tissue, the ultimate tensile strength (UTS) signifies the loss of load-bearing capacity, and represents tissue separation. The yield, ultimate, and rupture point were similarly selected for the transverse group (Figure 7B). See Appendix A for details on the automated selection of these points. Material toughness (energy absorption for the whole specimen) was approximated using trapezoidal integration of the grip-to-grip strain relative to stress up to UTS, and from UTS to tissue rupture.

3.2.4 Two-Dimensional Strain Measurement with Digital Image Correlation

The high-speed film was synchronized to the force-displacement data to analyze the full-field strain at transition, yield, and UTS. Synchronization was achieved by filming an LED that was triggered when the Instron actuator began and stopped moving. Additional details on the high-speed film and DIC analysis are in Appendix A.

The line where a tear propagated at UTS was estimated by examining the DIC strain maps in combination with the raw high-speed film. A custom Matlab script calculated the angle of tear propagation relative to the loading axis and generated a region of interest around the tear, called the tear region, that spanned 0.1 mm above and below the tear line (0.2 mm total span), with boundaries parallel to the tear line. Some tears propagated from the specimen edge to a point of inflection, and finished tearing across the specimen surface at a different angle. For these specimens with multiple tear angles (n=10), the tear region for this initial tear propagation was used for strain analysis. The average 2D Green-Lagrange strain tensor in the x-y reference basis (Figure 4C) was determined from the DIC data within this tear region using NCORR[74]. This strain tensor was transformed to the principal basis to compute the right stretch tensor, $\underset{\approx}{\mathbf{U}}$, and the engineering strain tensor $\underset{\approx}{\mathbf{E}}$ ($\underset{\approx}{\mathbf{E}}=\underset{\approx}{\mathbf{U}}-\underset{\approx}{\mathbf{I}}$), along with the 1st and 2nd principal planar strains (E_1, E_2) and the maximum planar shear strain ($\gamma_{\max}$). The strain tensor was transformed back to the x-y reference basis to calculate the $\underset{\approx}{\mathbf{E}}$ components when the surface normal is *parallel* (E_{yy}) and *perpendicular* (E_{xx}) to the loading axis, and the shear component of the orthogonal x-y surfaces (γ_{xy}). The strain components on the tear surface, E_{tear} and γ_{tear}, were calculated by transforming the strain tensor from the reference basis to the tear surface, using the tear angle measured from the high-speed film. In this study, all reported shear strain values are tensoral. Local toughness in the tear region at UTS was estimated using trapezoidal integration of the stress-strain curve generated from tensor components of $\underset{\approx}{\mathbf{U}}$ and the Biot-Lure stress tensor on the surface normal to axial loading. Tissue necking was calculated as the percentage of specimen width reduction that occurred from preload to UTS at the center of the tear region.

3.2.5 Statistical Analysis

All statistical analyses were completed with SPSS software (IBM; Armonk, NY, USA; v24). The effect of age on stress, grip-to-grip strain, local strains in the failure region, toughness, and angle of tear propagation were determined using MANOVA tests at the three points of interest (transition, yield, and ultimate) for either loading configuration. ANOVA tests were used to determine differences between distinct strain components at the same time point (e.g. E_{yy} *vs.* E_1) with Tukey post hoc testing, and a t-test was used to determine the effect of loading configuration on the angle of tear propagation. In cases where Leven's test detected variance heterogeneity, a Welch's ANOVA was used. Previously published data[27], was used to estimate the sample size needed to detect with 80% confidence (Power 0.80) a 25% change in the ultimate strength and grip-to-grip ultimate strain due to age. A posteriori, effect size and corresponding 95% confidence intervals were calculated[75]. For all statistical tests, significance was set at $p < 0.05$. All means are reported with one standard deviation.

3.3 Results

3.3.1 Tear Propagation

Tear propagation coincided with localized regions of high strains (Figure 8). The average angle of tear propagation, measured perpendicular to the loading axis, was 58±22° for longitudinal specimens and 12±9° for transverse (Table 2). The difference in tear angle between loading configurations was significant (p<0.01). However, there was no significant effect of age on the angle of tear propagation in either longitudinal

(p=0.20) or transverse specimens (p=0.14).

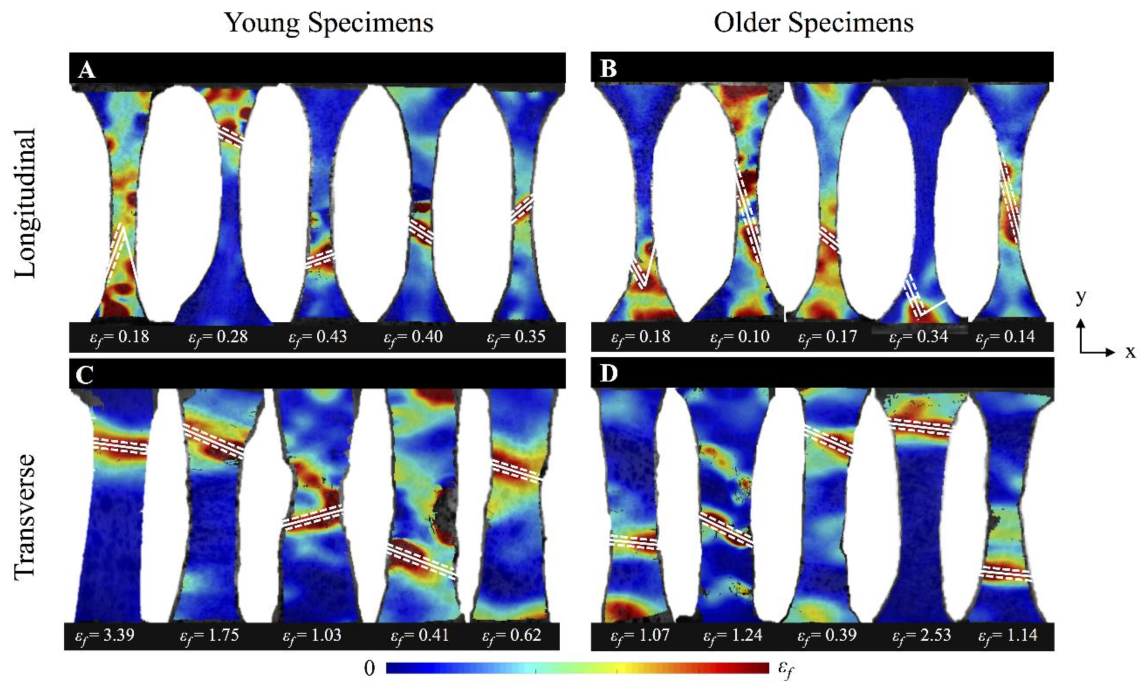

Figure 8: E_{yy} strain maps at UTS for posterior specimens. A) Tears propagated oblique to the loading axis (y-axis), near the plane of maximum shear stress, when loaded longitudinal to the fiber direction in younger and B) older specimens. C) Tears propagated perpendicular to the loading axis, near the plane of maximum tensile stress, when loaded transverse to the fiber direction in younger and D) older specimens. Solid white lines denote tear lines, dashed white boxes denote the analyzed tear region. Each specimen color map is scaled from 0 to the average E_{yy} strain in the tear region at UTS (εf).

Table 2: Comparison of tensile mechanical properties between different ages of human lateral meniscus when loaded longitudinal or transverse to the circumferential fiber direction. Effect sizes and their confidence intervals (CI) give a 95% confidence that potential differences in mechanical properties between all non-significant comparisons have an absolute effect size ≤ 1.8. Sample size for each cell = 10.

	Longitudinal			Transverse		
	Young	**Older**	**Effect Size [95% CI]**	**Young**	**Older**	**Effect Size [95% CI]**
Tangent Modulus (MPa)[a]	109.9 ± 40.8	97.2 ± 33.8	-0.34 [-1.22, 0.54]	1.7 ± 0.7	1.1 ± 1.0	-0.75 [-1.66, 0.16]
Yield Strength (MPa)	5.3 ± 2.7	4.3 ± 2.0	-0.43 [-1.32, 0.45]	0.21 ± 0.17	0.14 ± 0.12	-0.52 [-1.41, 0.37]
Yield Strain (%)[a]	7.4 ± 1.4	6.8 ± 1.0	-0.51 [-1.40, 0.38]	18.2 ± 18.9	19.5 ± 15.4	0.07 [-0.80, 0.95]
Ultimate Strength (MPa)	13.3 ± 7.3	9.9 ± 6.1	-0.51 [-1.41, 0.38]	0.47 ± 0.20	0.27 ± 0.19	*-1.03 [-1.96, 0.10]
Ultimate Strain (%)[a]	16.8 ± 4.9	13.8 ± 4.7	-0.63 [-1.52, 0.27]	54.6 ± 24.7	44.1 ± 17.1	-0.49 [-1.38, 0.40]
Rupture Strain (%)[a]	28.4 ± 10.0	20.7 ± 4.4	*-0.99 [1.92, 0.07]	108.0 ± 40.3	90.3 ± 30.0	-0.50 [-1.39, 0.39]
1st Principal Strain in Tear Region at UTS (%)[b]	41.0 ± 8.6	28.8 ± 8.8	*-1.40 [2.37, 0.42]	192.0 ±113.4	152.4 ±106.3	-0.36 [-1.24, 0.52]
2nd Principal Strain in Tear Region at UTS (%)[b]	-15.5 ± 12.2	-12.9 ± 12.1	0.22 [-0.66, 1.10]	-48.3 ± 11.8	-39.1 ± 15.2	0.67 [-0.23, 1.57]
Max Shear Strain in Tear Region at UTS (%)[b]	28.3 ± 8.3	20.8 ± 8.4	-0.89 [-1.80, 0.03]	120.1 ± 59.6	95.8 ± 59.4	-0.41 [-1.30, 0.48]
Material Toughness up to UTS (J/ml)[a]	1.2 ± 0.8	0.7 ± 0.6	-0.63 [-1.53, 0.27]	0.14 ± 0.09	0.06 ± 0.05	*-1.10 [-2.04, 0.16]
Material Toughness from UTS to Rupture (J/ml)[a]	0.46 ± 0.36	0.29 ± 0.22	-0.56 [-1.45, 0.34]	0.15 ± 0.07	0.05 ± 0.02	*-1.94 [-3.01, -0.88]
Local Toughness in Tear Region up to UTS (J/ml)[b]	2.4 ± 1.7	0.9 ± 0.8	*-1.16 [2.10, 0.21]	0.55 ± 0.46	0.26 ± 0.25	-0.79 [-1.70, 0.12]
Angle of Tear Propagation (deg)[c]	51.5 ± 25.6	64.2 ± 16.3	0.59 [-0.30, 1.49]	14.9 ± 8.3	9.1 ± 8.3	-0.70 [-1.60, 0.21]
Necking in Tear Region (%)	5.3 ± 8.3	3.4 ± 13.1	-0.18 [-1.06, 0.70]	44.6 ± 16.3	46.0 ± 23.2	0.07 [-0.81, 0.94]

3.3.2 Stress and Grip-to-Grip Strain

The tensile strength of older longitudinal specimens were on average 26%, 19%, and 15% weaker than younger specimens at ultimate, yield, and transition points, respectively (Figure 9A); although these differences were not significant (Table 2; $p>0.26$). For transverse loading, the ultimate and yield strength of older specimens were 43% and 36% weaker than young specimens, respectively (Fig. 6 B), with differences in ultimate strength being significant (Table 2; $p=0.034$). Specimen age had no significant effect on tangent modulus for either longitudinal ($p=0.46$) or transverse tests ($p=0.11$) (Table 2).

The average grip-to-grip strains of older longitudinal and transverse specimens at nearly all points of interest were less than younger specimens (Figure 9C-D), but only the 27% reduction in longitudinal rupture strain was significant (Table 2; $p=0.039$).

The material toughness (area under stress-strain curve using grip-to-grip strain) trended less in older specimens (Table 2). For transverse loading, the material toughness of older specimens was 55% less than younger specimens when measured to UTS ($p=0.008$), and 65% less when measured after UTS to rupture ($p=0.004$). For longitudinal loading, the material toughness of older specimens was 39% and 38% less (non-significant) than younger specimens when measured to UTS ($p=0.17$) and from UTS to rupture ($p=0.23$), respectively.

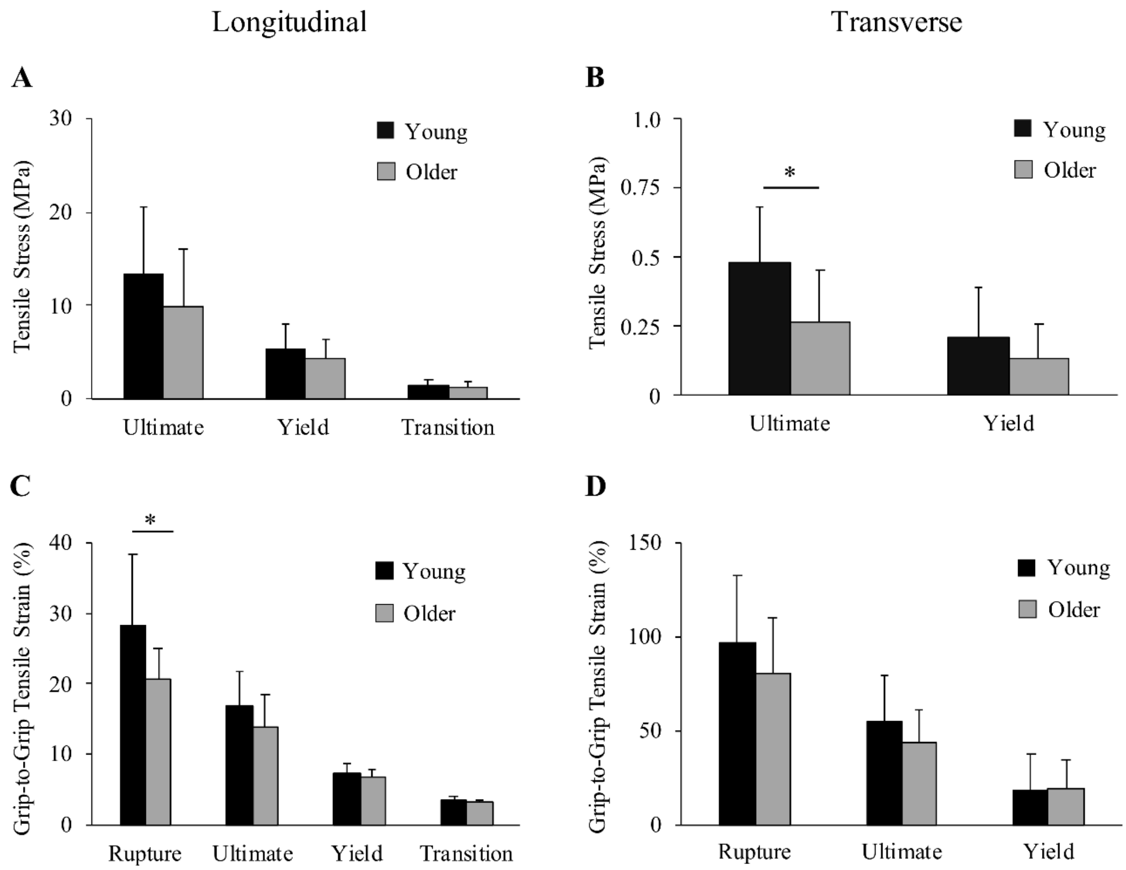

Figure 9: Comparison of grip-to-grip strain and stress for different age groups. On average, young specimens withstood greater stresses than older specimens during A) longitudinal and B) transverse loading, and were stretched to greater strains than older specimens during C) longitudinal and D) transverse loading, but most differences were not significant. Error bars represent one standard deviation. *p < 0.05.

<u>3.3.3 Local Strains in the Tear Region using DIC</u>

Older longitudinal specimens showed significantly less tensile strain (E_{yy} and E_1) in the tear region at UTS than younger specimens (p<0.05), but age had no other significant effect on local strain magnitudes (Figure 10A-E). Older specimens had approximately half the local toughness in the tear region relative to older specimens in both the longitudinal (p=0.02) and transverse groups (p=0.10) (Table 2).

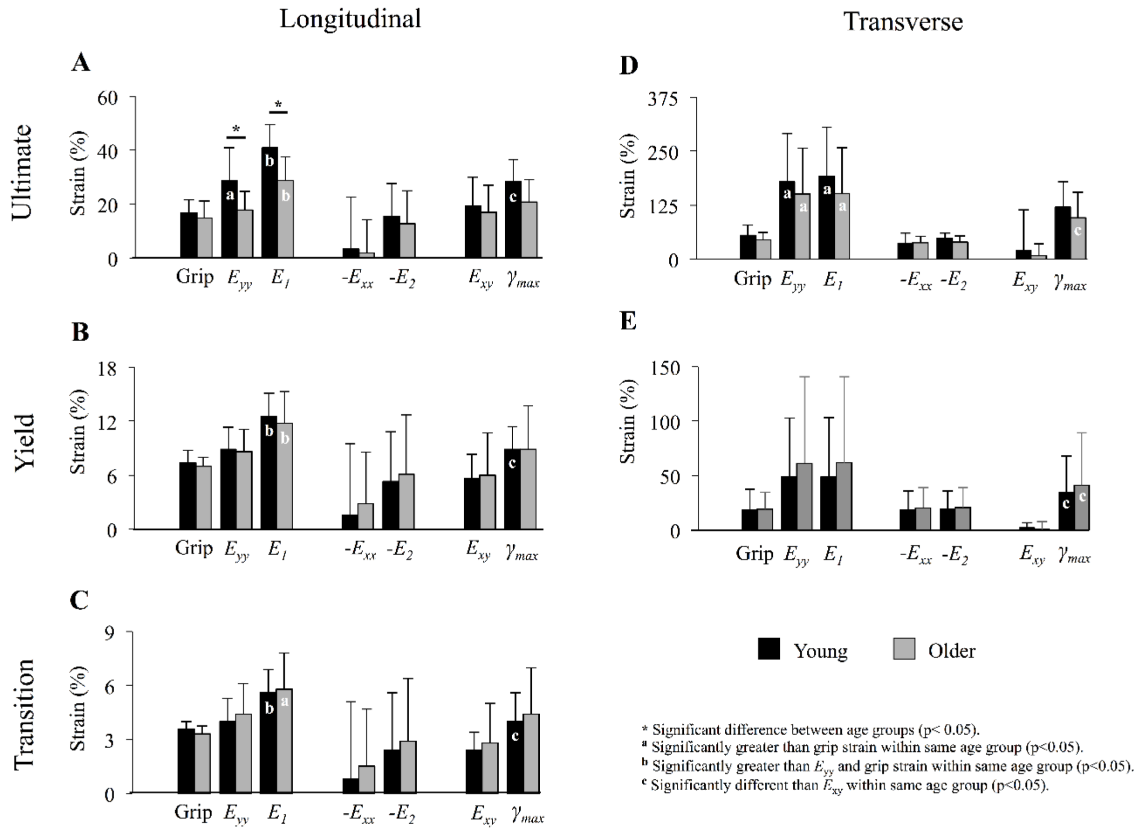

Figure 10: Comparison of engineering strains in young and older specimens within the failure region (E_{yy}, E_1, E_{xx}, E_2, E_{xy}, and γ_{max}) and between grips. Strains were analyzed during longitudinal loading at A) ultimate, B) yield, and C) transition points; and during transverse loading at D) ultimate and E) yield points. In this study, both E_{xy} and γ_{max} were calculated as tensorial shear strains. Error bars represent one standard deviation. Significance set to $p < 0.05$ for all comparisons.

First principal strains in the tear region were considerably greater than strains measured along the loading axis (grip and E_{yy}) for most points of interest (Figure 10A-E). For example, first principal strain (E_1) within the tear region at UTS was approximately 200% and 350% greater than grip-to-grip strains in the longitudinal (p<0.01) and transverse p<0.001) group, respectively (Figure 10A, D).

The 2D strains on the tear surface were also calculated (Fig. 8). For longitudinal specimens, the tear surface experienced tensile (E_{tear}) and shear strains (γ_{tear})(Figure 11A-B), where younger specimens had significantly greater tensile strains than older specimens *(*Figure 11C, *p*=0.01*)*. For transverse specimens, the tear surface experienced predominantly tensile strain (Figure 11D-E), and there was no effect of age on the strain magnitudes (Figure 11F).

Lastly, there was no significant effect of age on necking in either the longitudinal or transverse groups (*p*=0.61 and *p*=0.62, respectively) (Table 2), and meniscus location (anterior vs posterior) had no significant effect on any measured properties.

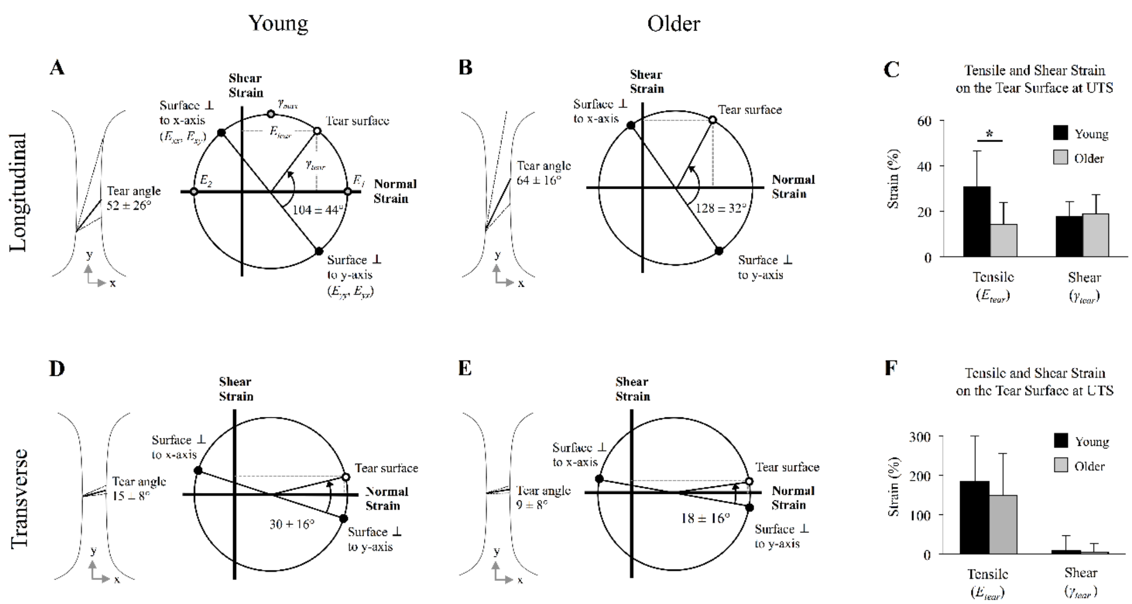

Figure 11: Mohr's circles of the average planar strain tensor within the failure region for longitudinal specimens from A) young, and B) older populations with C) average tensile and shear strains on the tear surface for the longitudinal group. Similarly, Mohr's circles for the transverse specimens in D) young and E) older populations with F) average tensile and shear strains on the tear surface for the transverse group. Error bars represent one standard deviation, and *p < 0.05. These Mohr's circles give a mathematical visualization of how tensile and shear strain on the tear surfaces (dashed lines within Mohr's circles) were calculated. Note that angles on Mohr's circle are double the physical angles.

3.4 Discussion

The primary objective of this study was to determine the effect of age on the anisotropic tensile failure behavior of human lateral meniscus. Our first hypothesis was that extensibility of the tissue would decrease with age. Extensibility is a measure of a material's ability to elongate, and was evaluated by measuring tensile strain between the grips and within the tear region at multiple points of interest (Figure 7). When stretching the circumferential fibers (longitudinal group), we found that older specimens were 27% less extensible at rupture than young specimens (Figure 9C), and were 30% less extensible within the tear region at UTS than young specimens (Figure 10A, E_1). This loss of extensibility contributed to older specimens having ~60% less toughness (energy absorption) within the tear region compared to young specimens (Table 2). When stretching the ground substance (transverse group), older specimens were approximately 20% less extensible at UTS and rupture (Figure 9D, Figure 10 D), but these differences were not significant. Nevertheless, the (non-significant) reductions in extensibility, combined with significant decreases in ultimate strength (Figure 9B), resulted in older transverse specimens having 55% less energy absorbed (toughness) up to UTS, and 65% less energy absorbed after UTS (Table 2). The deficient toughness of older specimens (longitudinal and transverse) indicates that aging populations would be more susceptible to tears from high-energy loading events. Overall, the strain results partially support our first hypothesis, in that age reduced the extensibility of the circumferential fiber network, but not the ground substance.

Our second hypothesis was that tears occur on the plane of maximum shear stress, which is 45° from the loading axis. Longitudinal specimens did indeed fail close to this plane, with tears propagating on average at 58° (Figure 11, Table 2). Conversely, tears in transverse specimens occurred closest to the 0° plane of maximum tensile stress, after a considerable amount of necking. Analysis of the tear surfaces showed good agreement between the estimated stresses and the measured strains, as the tear surface of transverse specimens had high magnitudes of tensile strains (Figure 11D-E), and the tear surface of longitudinal specimens had shear strains relatively close to the maximum shear strain (Figure 11A-B). Notably, the maximum principal strains were not well-aligned with the loading axis in longitudinal tests (Figure 11A-B), leading to significant differences in E_{yy} and E_1 (Figure 10A) which may possibly be explained by fiber sliding[76]. Collagen fiber sliding creates shear on the surface normal to the x-axis (Figure 4C), which would effectively rotate the strain tensor eigenvectors relative to the loading axis. Another notable finding was that older longitudinal specimens had nearly 50% less tensile strains on the tear surface compared to younger specimens. This is consistent with the observed reductions of extensibility in older specimens (Table 2; E_1). Overall, results from this study partially supported our second hypothesis, in that meniscus tears occurred near the plane of maximum shear stress when loaded along the circumferential fibers.

The local strains measured in this study can inform and validate the selection of failure criteria for macroscale mathematical models and provide insight into meniscus failure mechanisms. The oblique tear angle observed during longitudinal loading (Figure 8) indicates that maximum shear stress or distortion energy may be appropriate failure criteria to model tears that occur from tensile stress in the fiber direction. However, when modeling tears that occur from tensile stress transverse to the fiber direction, our results would suggest that maximum tensile stress (or strain) failure criteria are appropriate. This recommendation is consistent with matrix mode failures that occur in unidirectional fiber reinforced composites[77,78]. The observed dependence between failure behavior and fiber direction emphasizes the importance of using anisotropic failure criteria when modeling damage in soft fibrous tissue. It's interesting to note that the local *yield* strains for the transverse group (ground substance response) are greater than the local *ultimate* strains for the longitudinal group (fiber response) (Figure 10, Table 2), indicating that the ground substance is undamaged when fibers begin losing load-bearing capacity. This suggests a fiber-driven failure mechanism for meniscus, possibly similar to macroscale failure theories proposed for engineered composites that have high-strength uniaxial fibers embedded in a ductile matrix[79].

This was the first study to measure the effect of aging on mechanical failure behavior in human meniscus, but similar biomechanics studies have been performed on ligament, tendon, and cartilage[29,32,34]. Consistent with our findings, these previous studies reported reductions in modulus, ultimate strength, and failure strain with age. Since it's been shown that neither collagen content nor collagen cross-linking decrease in collagen-rich tissues as we age[55,80], the loss of strength and extensibility that has been observed in older specimens likely indicates an accumulation of structural damage. This structural damage could potentially be caused by age-dependent changes in collagen fiber organization[81] or the unfolding of collagen molecules due to repeated loading[82].

To our knowledge, this is the first study to report the (nearly) instantaneous strain behavior within the tear region of any soft fibrous tissue. This advance was made possible by pairing DIC with high-speed video. A striking discovery was that meniscus tissue is more extensible than previously reported. On average, young meniscus tissue will stretch 41% when loaded along the fibers and 192% when loaded against the fibers before losing load-bearing capacity (Table 2; E_1 in tear region at UTS). These local tensile strains were more than double our grip-to-grip ultimate strains (Table 2), and to our knowledge are greater than any previously reported ultimate tensile strains for meniscus, tendon, or ligament. The large difference between grip-to-grip and local strains can be explained by the strain maps we captured at UTS (Figure 8), which reveal that strains are concentrated in the tear region, and the majority of tissue is relatively undeformed at failure. For additional comparisons of our mechanical results with previous studies on human meniscus, please see Appendix A.

This study had limitations. Quasi-static tests were conducted on only the central region of the lateral meniscus, and meniscus failure properties may vary for different anatomical regions (e.g. medial meniscus) and loading rates. Similar to a previous ligament study[83], we used a preconditioning strain of 8% for longitudinal loading. This preconditioning strain exceeded the yield strain in six specimens by an average of 0.4 ± 0.3%. Although the failure properties of these six specimens were not significantly different from other specimens (data not shown), it's possible that some damage occurred during preconditioning. Based on the transition and yield strains from this study (Figure 9 C), we would recommend using grip-to-grip preconditioning strains between 4-6% for longitudinal tensile testing. In order to preserve the DIC speckle pattern, specimens were tested in air. While care was taken to frequently spray specimens with 0.9% saline, tissue hydration during tensile testing was likely less than physiological and this may have contributed to a higher rate of grip failures (46%) than we encountered when conducting tensile tests of bovine meniscus using a drip system (5%)[13] or human meniscus using a heated saline bath (20%)[84]. Lastly, this study used planar DIC, and may have missed important phenomena in out-of-plane strains and tear patterns.

3.5 Acknowledgements

Financial support kindly provided by the National Science Foundation under grant no. 1554353 (funded materials used in the experiment and personnel costs) and the National Institute of General Medical Sciences under award number P20GM109095 (funded some equipment used in the experiment). Many thanks to Belle Vita Funeral Home (Garden City, ID) for their help in laying donors to rest, and Greenfields Custom Meats (Meridian, ID) for providing bovine specimens used in pilot experiments for this study.

CHAPTER 4: DOTS-ON-PLOTS: A WEB APPLICATION TO ANALYZE STRESS-STRAIN CURVES FROM TENSILE TESTS OF SOFT TISSUE[2]

4.1 Introduction

Uniaxial tensile tests are conventional experiments to characterize the mechanical behavior of engineered and biological materials. Stress-strain curves generated from tensile tests provide a graphical representation of a tissue's normalized load response to axial stretch. Several key mechanical properties can be quantified from these curves, including ultimate tensile strength (UTS), yield strength, energy to failure, and the transition strain [6,7,85] (Figure 12). International testing standards for many engineered materials (e.g. plastics, polymer matrix composites)[86,87] provide guidelines for identifying and calculating relevant properties from stress-strain curves. These standards reduce the probability that the reported properties are biased by their testing environment or calculation method, thus improving reproducibility between different research groups. These standards have also led to the development of software packages [88,89] to automate the calculation of mechanical properties, further reducing the subjectivity and burden of data analysis on research groups. Unfortunately, no testing standards exist for tensile testing of soft biological tissues, and existing software packages are unable to account for soft tissue's non-linear stress-strain behavior (Figure 12).

[2] Reprinted from *Journal of Biomechanical Engineering* Nesbitt DQ, Nelson ML, Shannon KS, Lujan TJ. "*Dots-on-Plots: A Web Application to Analyze Stress-Strain Curves from Tensile Tests of Soft Tissue.*" 2023 Feb 1;145(2):024504.[133]

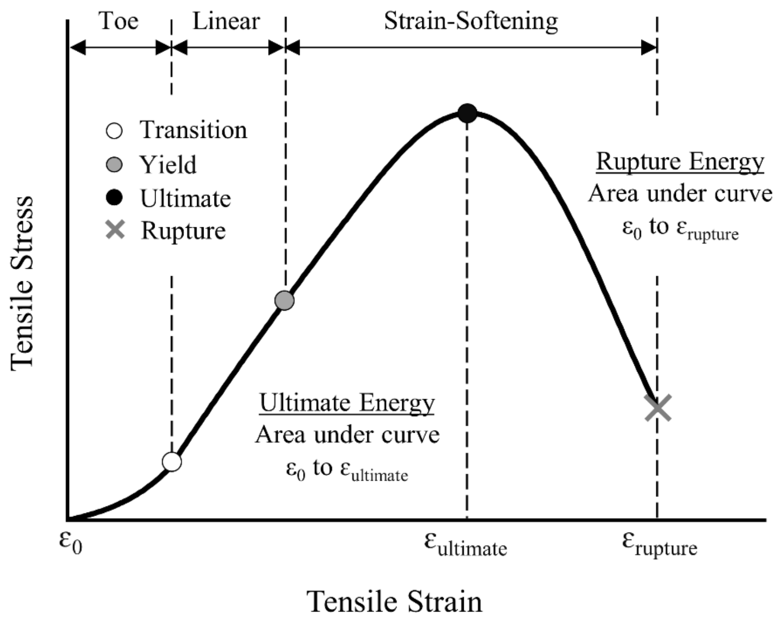

Figure 12: Representative tensile stress-strain curve of soft tissue with marked points of interest (transition, yield, ultimate, and rupture), as well as different measures of strain energy density.

The lack of standards for tensile testing of soft fibrous tissues has resulted in biomedical research groups using different methods to calculate mechanical properties. One such mechanical property, the transition strain, physically represents the straightening of collagen fibers [85]. At the transition point, soft fibrous tissue "transitions" from an exponential stress-strain response (toe region), to an approximately linear response (Figure 12). This point on the stress-strain curve is important, as the normal physiological functions of tendon and ligament occur mostly in the toe region [90], and below the transition point the tissue is highly resistant to fatigue damage [82]. Methods to calculate the transition point vary widely across research groups, and include using inflection points of a polynomial fit [13,91], bimodal linear fitting algorithms [14,59], piecewise fitting algorithms [92], or deviation of either stress or strain from a linear fit to the linear region [12,60]. While descriptions of these methods are published, the custom programs written to do the analysis are not publicly available. This lack of standardization and transparency could be contributing to the wide variance of reported transition strains that exist between research groups (Table 3)[7,12–14,91,93]. It's possible to reduce cross-lab variability and accelerate the pace of discovery by giving research groups access to a standardized computational tool that automates the calculation of transition strain and other tensile properties in soft tissue. A type of computational tool that provides exceptional accessibility is a web-based software application, which permits instant access to anyone with an internet connection. The objectives of this work are to 1) develop a free, web-based software application for the calculation of soft-tissue tensile properties, and 2) identify optimal program settings to minimize transition strain error when evaluating experimental stress-strain curves.

Table 3: Tensile transition strains for meniscus tissue from different research groups. All strain values are in engineering strain.

Study	Species	Method	Transition strain
Nesbitt et al., 2021	Human	10% stress deviation from linear fit	3.6 ± 0.4%
Tissakht & Ahmed, 1995	Human	Bimodal polynomial fitting	7.4 ± 2.6%
He et al., 2020	Porcine	Bimodal linear fitting	4.6 ± 0.7%
Abdelgaied et al., 2015	Porcine	Bimodal linear fitting	5.5 ± 0.9%
Wale et al., 2020	Bovine	5% stress deviation from linear fit	5.2 ± 1.2%
Danso et al., 2014	Bovine	0.6% strain deviation from linear fit	5.9 ± 1.9%

4.2 Materials and Methods

4.2.1 Overview

A web-based application called Dots-on-Plots was built to automatically calculate and output mechanical properties from tensile stress-strain curves. The optimal threshold setting for computing transition strain was determined by finding what threshold value resulted in the most accurate transition strains when analyzing stress-strain curves from twenty tensile tests of human meniscus. The "gold standard" transition strain used to measure accuracy was determined by curve fitting a hyperelastic-damage model, which included transition strain as a material parameter, to the experimental data using finite element parameter optimization. In addition, 27 variations of stress-strain curves were synthetically generated with a finite element solver to determine whether the calculation of transition strain was sensitive to curve shape.

4.2.2 Automated Calculation of Mechanical Properties

Dots-on-Plots calculates tensile mechanical properties by identifying four points (or dots) of interest: transition, yield, ultimate, and rupture. The transition point represents the straightening of the crimped collagen fibers [85]; the yield point marks the yield strength and may indicate where damage accumulation begins to soften the tissue; the ultimate point marks the ultimate tensile strength (UTS) which signifies the loss of load-bearing capacity; and rupture represents tissue separation. The yield point was selected at the maximum positive slope of the stress-strain curve [6,13], the ultimate point at the maximum stress, and the rupture point when stress drops below a user specified percentage of the UTS. The linear modulus was calculated as the slope of a linear fit to the stress-strain data within a 1% strain interval below the maximum slope (Figure

13)[13,91].

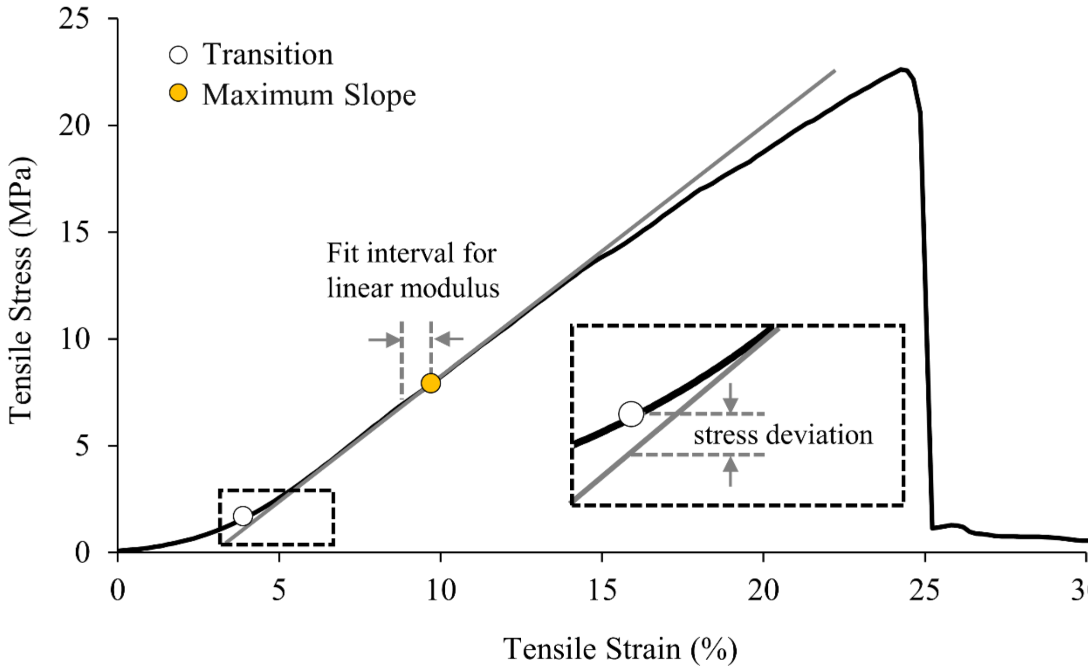

Figure 13 Graphical depiction of the method used to determine the transition point. The transition point is determined from the deviation between the stress-strain curve and the linear fit to the linear region below the maximum slope. In this study, the fit interval was 1% strain.

The transition point was then determined as the point on the stress-strain curve, below the yield point, where the stress σ deviated from the stress predicted from the linear fit σ_{linear} by a set percentage of the stress at the point of maximum positive slope σ_{ms} (Figure 13). This can be mathematically expressed as follows, where the largest value of strain ε that satisfies this equation is marked as the transition strain.

$$\left|\frac{\sigma(\varepsilon) - \sigma_{linear}(\varepsilon)}{\sigma_{ms}}\right| \times 100 \ \geq \ \text{\% Stress Deviation} \tag{1}$$

Stress and strain at each of these four points of interest are output as mechanical properties. In addition, the strain energy density at each point of interest is calculated. Strain energy density represents the potential energy absorbed by the tissue, normalized by volume, and was calculated as the area under the stress-strain curve using trapezoidal integration up to the point of interest. For example, the strain energy density that accumulates from no strain to ultimate strain would be the ultimate energy, and from no strain to the rupture strain would be the rupture energy (Figure 12). Calculations are independent of units and will display the stress and strain magnitude as provided in the input file. For example, if the stress column is calculated in MPa, the yield strength will be in MPa. Importantly, the user-input stress and strain measures must be energy conjugates to properly calculate the strain energy density (area under the stress-strain curve)[94].

4.2.3 Web Application Development

A web application was developed to satisfy four primary design criteria: efficiency, reliability, flexibility, and convenience (Table 4). These design criteria were addressed by incorporating specific design features into a program that was initially developed in Python using the aforementioned algorithms for calculating mechanical properties. This original Python code (available on GitHub: *https://github.com/ntm-bsu/dots-on-plots*) was installed on a server and a web interface was written in standard

Table 4: Dots-on-Plots design criteria and corresponding design features.

Design Criteria	Design Feature
1) Efficient	Fast, automated batch processing of multiple input files.
2) Reliable	Transparent calculations using graphical displays.
3) Flexible	Thresholds that define properties are adjustable.
4) Convenient	Accessible via the web. Properties and plots exported as CSV and PDF.

HTML, Javascript, and CSS. The server processes data files in parallel, writing out the output images and data to the client.

4.2.4 Determining an Optimal Threshold to Calculate Transition Strain

The calculation of transition strain in Dots-on-Plots is based on a user-specified threshold for percent stress deviation (Eq. 1). To determine the optimal threshold value to minimize the expected error when evaluating this property, stress-strain curves were analyzed that had a known answer for transition strain ($\varepsilon_{trans\_actual}$). This known answer was then compared to the transition strain output by Dots-on-Plots for a given threshold (ε_{trans_dots}). For this analysis, stress-strain curves were acquired from 20 monotonic uniaxial tensile tests (loading rate = 1% strain/s) taken from five young human menisci (age = 33 ± 5 years) and five older human menisci (age = 72 ± 7 years)[91]. The two age groups have significant differences in mechanical properties [91], and therefore we included both age groups to have a more diverse set of stress-strain curves. The twenty experiments were analyzed in Dots-on-Plots using five different threshold settings of percent stress deviation (1, 2, 3, 5, and 10%) to calculate transition strain (ε_{trans_dots}). We selected these settings to span the range of threshold values applied in previous studies to calculate transition strain (Table 3).

To calculate the known or actual transition strain (ε_{actual}), the experimental stress-strain curves were curve fit to a hyperelastic-damage model using the free finite element solver, FEBio [95]. For this simulation, a single hexahedral element was pulled in tension using a sliding elastic contact to allow displacement along the axial load direction. The selected material was transversely isotropic hyperelastic, where the model's strain energy density Ψ is uncoupled into a ground substance F_1 and fiber matrix F_2:

$$\Psi = F_1(\lambda) + F_2(\lambda) + \frac{K}{2}(ln(J))^2 \tag{2}$$

Here λ is stretch, J is the volume change ratio, and K is bulk modulus, which was set to 1000 to enforce near-incompressibility [96]. We used a Veronda-Westmann ground substance and a piecewise exponential function of the fiber matrix.

$$F_1(\lambda) = C_1\left(e^{(C_2(I_1-3))} - 1\right) - \frac{C_1C_2}{2}(I_2 - 3) + U(J) \tag{3}$$

$$F_2(\lambda) = \begin{cases} 0 & \lambda \leq 1 \\ C_3\left(e^{-C_4(E_i(\lambda)-E_i(C_4))}\right) - ln\,(\lambda) & 1 < \lambda < \lambda_m \\ C_5(\lambda - 1) + C_6 \ln(\lambda) & \lambda \geq \lambda_m \end{cases} \tag{4}$$

The strain energy of the ground substance is dependent on two user specified material constants (C_1, C_2), the first and second invariants of the deviatoric portion of the right Cauchy Green deformation tensor (I_1, I_2), and the dilational term (U). The strain energy contribution of the fibers is a piecewise function dependent on stretch. Importantly, the transition stretch λ_m is included as a material parameter that defines the transition between the exponential and linear regions[92]. When the stretch is below λ_m, the function is dependent on two user specified fiber straightening constants (C_3, C_4), and is calculated using the exponential integral function (E_i). At a stretch above λ_m, the fibers take on an approximately linear character, and are dependent on one user specified constant for fiber modulus C_5 and one calculated constant C_6 to ensure stress is continuous at the transition stretch. The strain energy density is converted to an effective Cauchy stress $\boldsymbol{\sigma_0}$ [95].

In order to model strain softening (Figure 12), a quintic polynomial cumulative distribution function was implemented to apply damage evolution to the stress-strain curves.

$$D(\Xi) = \begin{cases} 0 & \Xi \leq \mu_{min} \\ x^3(6x^2 - 15x + 10) & \mu_{min} < \Xi < \mu_{max}, \\ D_{Max} & \mu_{max} < \Xi \end{cases} \qquad x = \frac{\Xi - \mu_{min}}{\mu_{max} - \mu_{min}} \tag{5}$$

Damage D can range from values of 0 to 1, and is a function of the first principle Lagrange strain (Ξ). The limits of damage evolution (μ_{min}, μ_{max}) determine the strain values where damage initiates and reaches a maximum (D_{max}). Finally, Cauchy stress $\boldsymbol{\sigma}$ was calculated by scaling the effective undamaged stress $\boldsymbol{\sigma_0}$ with damage D.

$$\boldsymbol{\sigma} = (1 - D)\boldsymbol{\sigma_0} \tag{6}$$

<u>4.2.5 Parameter Optimization</u>

The material parameters were curve fit to experimental data (axial force vs. time) using the Levenberg-Marquardt parameter optimization module in FEBio [95,97]. Parameter optimization was conducted in two steps. In the first step, only the hyperelastic model was run (Eq. 2-5), and the elastic material parameters (C_1, C_2, C_3, C_4, C_5, λ_m) were fit to the toe and linear region of the stress-strain curve (Figure 12). Initial guesses for C_1, C_5, and λ_m were based on previously measured mechanical properties [91] with optimization limits of more than ± two standard deviations to help ensure convergence to a global minima. Initial guesses for the remaining elastic parameters were determined by trial and error, with maximum and minimum limits of approximately double and one-half the initial guess, respectively. In the second step, the full hyperelastic-damage model was run (Eq. 6), and the damage parameters were fit to the strain-softening region of the stress-strain curve (Figure 12) with initial guesses set as the values of Lagrange strain at yield and rupture (70% of UTS) from our previous experiments [91]. When optimization returned a parameter extremum, the extrema was expanded by 30% and optimization was re-performed.

The axial component of stress from the model and experiment were plotted together as a function of engineering tensile strains ($\varepsilon = \lambda - 1$). The hyperelastic-damage model resulted in excellent fits for all experimental data (Figure 14), with an average R^2 value of 0.998 ± 0.002, and an NRMSE of 2.9 ± 1.2% (normalized to mean stress). The average model coefficients used to fit these twenty experiments are given in Table 5. The transition stretch λ_m from the optimized model fit was converted to the known or "actual" transition strain ($\varepsilon_{actual} = \lambda_m - 1$). This known transition strain was then used to estimate the accuracy of Dots-on-Plots by calculating the error ($\varepsilon_{trans\_dots} - \varepsilon_{trans\_actual}$) and absolute error (|$\varepsilon_{trans\_dots}$ - $\varepsilon_{trans\_actual}$ |) of the measured transition strain. A similar approach to estimate accuracy has been used in previous studies [98,99].

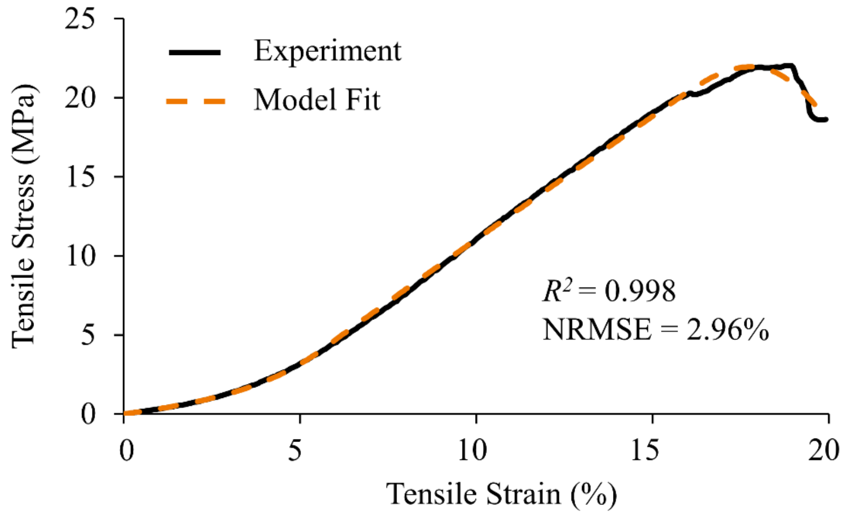

Figure 14: The hyperelastic-damage model gave excellent fits to the experimental data.

Table 5: Average model coefficients that were curve fit to experimental stress-strain curves (average ± standard deviation). The quality of fit was measured by the percent error (NRMSE) of the simulated stress curve relative to experimental data.

	C_1	C_2	C_3	C_4	C_5	λ_m	μ_{min}	μ_{max}	D_{max}	*NRMSE*
Young	0.75 ± 0.53	1.39 ± 0.53	0.42 ± 0.10	37.9 ± 6.8	115.0 ± 38.7	1.052 ± 0.006	0.14 ± 0.08	0.29 ± 0.10	1	2.42 ± 0.99
Older	0.71 ± 0.78	1.24 ± 1.18	0.47 ± 0.17	37.0 ± 8.1	100.2 ± 36.0	1.048 ± 0.007	0.11 ± 0.05	0.26 ± 0.13	1	3.29 ± 1.23
Total	0.73 ± 0.65	1.32 ± 1.07	0.45 ± 0.14	37.5 ± 7.3	107.6 ± 37.2	1.050 ± 0.006	0.12 ± 0.07	0.28 ± 0.11	1	2.86 ± 1.18

4.2.6 Sensitivity of Transition Strain to Shape of Stress-Strain Curves

A sensitivity analysis was conducted to determine if factors that affect the shape of the stress-strain curve will significantly influence the calculation of transition strain. We used the aforementioned hyperelastic-damage model (Eq. 2-6) to artificially generate a set of 27 unique stress-strain curves by adjusting the toe region, linear modulus, and damage onset (Figure 15). The toe region was adjusted by inputting λ_m values into the

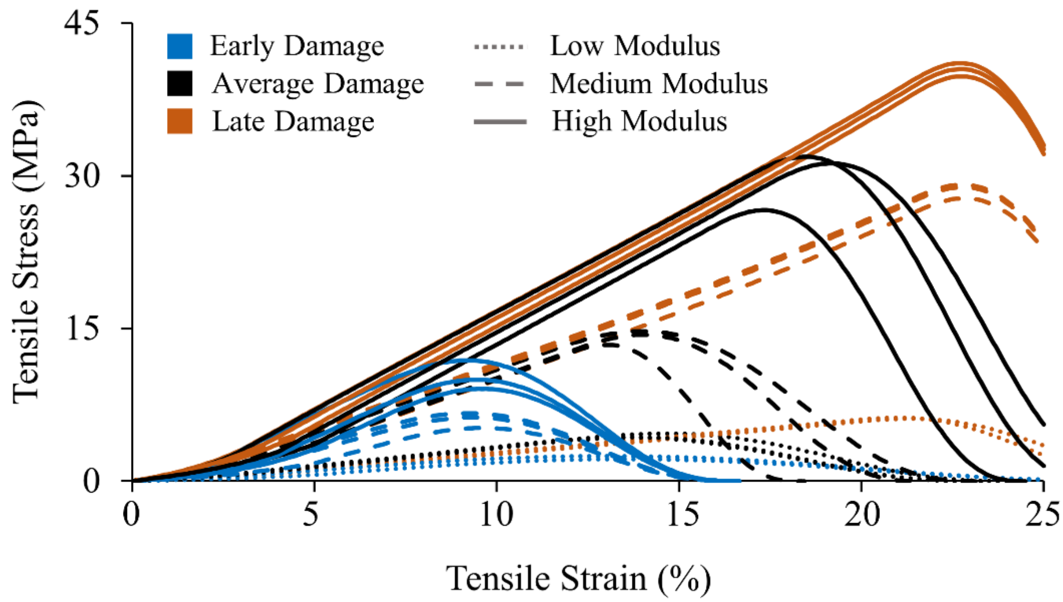

Figure 15: Model generated stress-strain curves using three different settings for transition strain, linear modulus, and damage onset, resulting in 27 unique curves with known transition strains.

model that corresponded to transition strains of 3, 4, and 5% (small, moderate, and large, respectively); linear modulus was adjusted by inputting modulus values into the model (C_5) of 30, 110, and 190 MPa (low, medium, and high, respectively); and damage onset was adjusted by inputting different μ_{min} values to have yield strain occur at 5 ± 1%, 12 ± 2%, and 19 ± 1% (early, average, and late, respectively). The three values for each tested group were based on the average ± two standard deviations from our previous mechanical study on human meniscus[91]. Since the transition stretch λ_m was a model input (Eq. 4), the actual transition strain was known ($\varepsilon_{trans\_actual}$) for all generated stress-strain data.

4.2.7 Statistics

All statistical analysis was performed using SPSS software (IBM; Armonk, NY, USA, v25). For analyzed data that was not normally distributed (determined using a

Kolmogorov-Smirnov normality test), non-parametric tests were used. For experimental stress-strain curves, the effect of stress deviation threshold (within-subject) and age group (between-subject) on the absolute error of the transition strain calculated by Dots-on-Plots was measured using a repeated measures ANOVA, with Tukey HSD post hoc testing. For synthetically generated stress-strain curves, the effect of input parameters (toe region, linear modulus, damage onset) on the absolute error of the transition strain calculated by Dots-on-Plots was measured using a non-parametric Kruskal-Wallis test. For all statistical tests, significance was set at $p < 0.05$. All means are reported with one standard deviation.

4.3 Results

4.3.1 Web Application

A free web application called Dots-on-Plots was developed (**Error! Reference s ource not found.**A), tested, and is now available online (*https://ntm.boisestate.edu/dots-on-plots/*). This application automatically calculates and exports mechanical properties for soft tissue tensile tests, and allows for multiple files to be input and run simultaneously. Users can upload .xlsx, .csv, or .txt files containing two columns of equal length data, with strain in the first column and stress in the second column. The program generates a stress-strain curve and a table of calculated mechanical properties for each uploaded file (**Error! Reference source not found.**A). The threshold settings can be a djusted by the user, including the stress deviation threshold used to calculate the

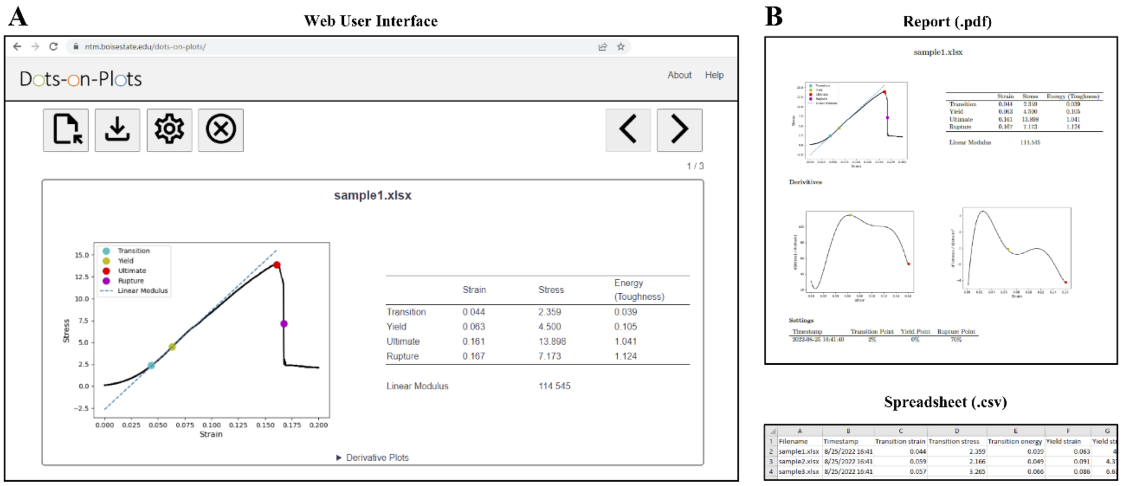

Figure 16 Dots-on-Plots web application. A) From a web browser, the user can upload multiple .txt, .csv, or .xlsx files, each with two equal columns of strain and stress data. The program automatically computes the mechanical properties and gives a graphical display of the results. B) The user can download a report and spreadsheet that detail and summarize all results.

transition point. Results from all analyzed files can be downloaded as one .pdf report and one .csv summary spreadsheet (**Error! Reference source not found.**B). The report has g raphical displays of the results, including derivative plots used to determine the maximum slope of the stress-strain curve. The summary spreadsheet allows for convenient plotting or statistical analysis of mechanical properties (Figure 16 B). The described features of this web application satisfy the design criteria (Table 4).

<u>4.3.2 Optimal Threshold to Calculate Transition Strain</u>

The error of the transition strain calculated by Dots-on-Plots was influenced by the threshold setting (Figure 17; $p < 0.001$), where a stress deviation threshold of 2% was most accurate. For all twenty experiments, the mean transition strain calculated using a 2% threshold in Dots-on-Plots (0.049 ± 0.007) was within 0.0007 (Figure 17) of the known mean transition strain (0.050 ± 0.006), corresponding to a mean percent error of 1.4%. For each individual experiment, the mean absolute error when using a 2%

threshold in Dots-on-Plots was 0.004 ± 0.004, corresponding to a mean absolute percent error of 8.2 ± 8.0%. This absolute error was significantly less than the 10% deviation setting ($p < 0.001$), but not significantly different than the 1%, 3%, or 5% threshold settings ($p = 0.23$; $p = 0.98$; $p = 0.18$, respectively) (Figure 17). There were no significant differences in the absolute error of the calculated transition strain due to age group ($p = 0.88$).

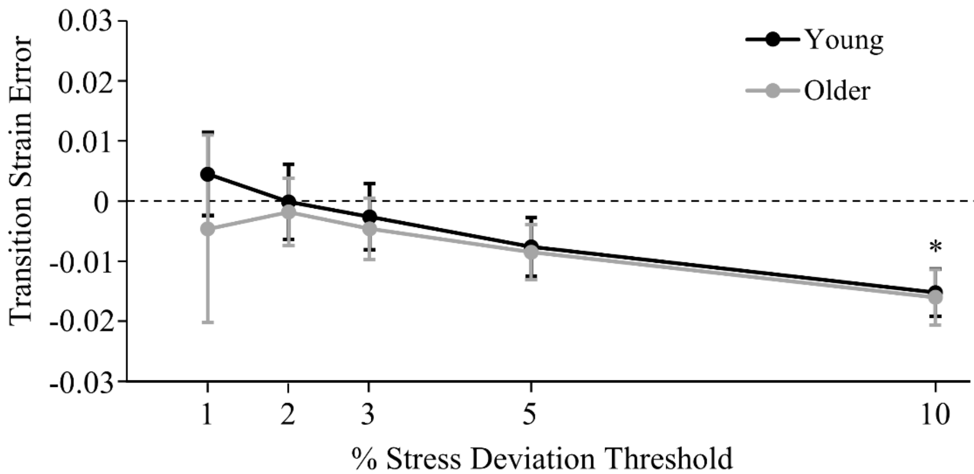

Figure 17: The lowest error for calculating transition strain with Dots-on-Plots occurred when using a % stress deviation threshold of 2%. *Significantly greater absolute error than other threshold values.

4.3.3 Sensitivity of Transition Strain to Shape of Stress-Strain Curves

The calculation of transition strain was most sensitive to damage onset (Figure 18; $p < 0.001$). Stress-strain curves with a late damage onset (Figure 15, orange curves) had significantly greater mean transition strains that were 2.5 times greater than the known mean (Figure 18, dashed line). The calculation of transition strain was insensitive to changes in linear modulus (p = 0.95), and to changes in the size of the toe region (p = 0.99) (Figure 18).

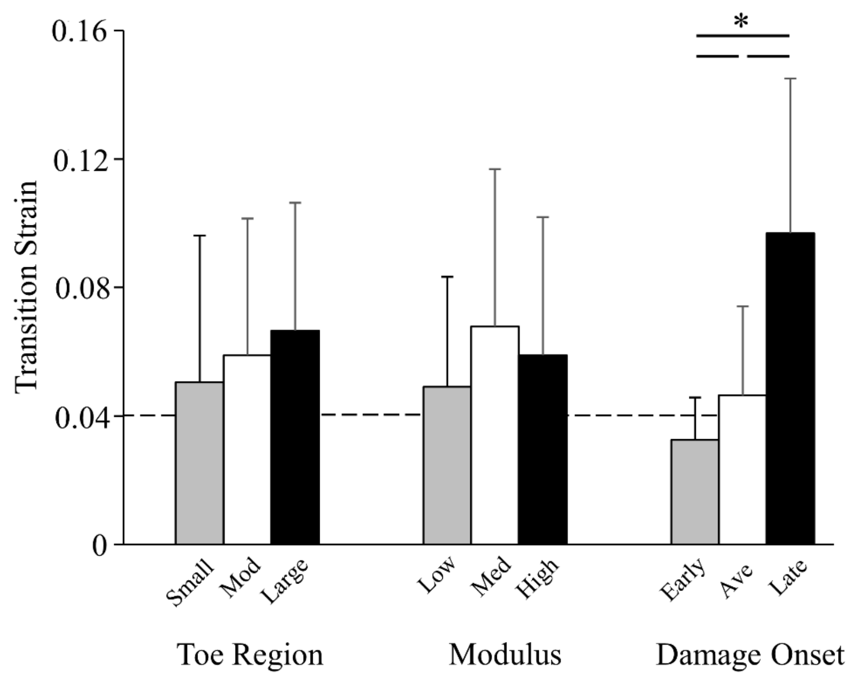

Figure 18: Sensitivity of the transition strain calculated by Dots-on-Plots to factors that alter the shape of the stress-strain curve. The program was most sensitive to curves with a late damage onset. The dashed line is the mean of the known transition strain (ε_{actual}). *Significant difference in absolute error of calculated transition strain (p < 0.05).

4.3.4 Automated Calculation of Mechanical Properties

The tensile mechanical properties of the twenty meniscus specimens (Table 6) were computed in Dots-on-Plots using the optimized threshold setting for the transition point (2% stress deviation from the linear fit), and a rupture point setting at 15% of the ultimate stress (based on our previous experimental work) [91]. The linear fit used to calculate linear modulus (Figure 13) had an average NRMSE of 0.30 ± 0.12% (R^2 = 0.998 ± 0.001). The mean and standard deviation values in Table 4 were calculated from the .csv output file generated by Dots-on-Plots (**Error! Reference source not found.**B). T he total runtime for Dots-on-Plots to analyze all twenty stress-strain curves was approximately 15 seconds.

Table 6: Tensile mechanical properties of twenty human meniscus specimens that were automatically calculated using Dots-on-Plots (mean ± standard deviation).

	Transition	Yield	Ultimate	Rupture
Strain (%)	4.94 ± 0.68	7.08 ± 1.18	15.49 ± 5.23	24.37 ± 8.46
Stress (MPa)	2.45 ± 1.08	4.66 ± 2.21	11.57 ± 6.63	4.02 ± 5.40
Energy (J/ml)	0.04 ± 0.02	0.13 ± 0.08	0.97 ± 0.75	1.32 ± 0.87
Modulus (MPa)	103.9 ± 37.2			

4.4 Discussion

The objectives of this work were to provide a free, web based computational tool to calculate the tensile mechanical properties of soft-tissue, and to identify the optimal settings to minimize error when calculating the transition strain, a mechanical property with important implications for soft collagenous tissues. We met our first objective by developing a web application called Dots-on-Plots that is now freely available on the internet at *https://ntm.boisestate.edu/dots-on-plots/* (**Error! Reference source not found.**). We met our second objective by determining that a 2% stress deviation was an optimal threshold for calculating transition strain from a set of uniaxial tensile experiments of human meniscus (Figure 17). We further identified characteristics of stress-strain curves that affect the calculation of the transition strain (Figure 18).

The development of Dots-on-Plots represents an important advance for the standardization of material characterization in biomedical engineering and beyond. To our knowledge, Dots-on-Plots will be the first web-based application that allows users to upload tensile test data to calculate mechanical properties. Existing software for analyzing stress-strain curves includes downloadable software packages that are tailored towards more common engineering materials, like metals or semiconductors [100,101]. While these programs are capable of calculating a wide variety of mechanical and thermodynamic properties, they would not be appropriate for handling the analysis of tissues that exhibit non-linear behavior. A recently released downloadable software, MechAnalyze [102], has sought to help fill this gap by automating the analysis of compressive force-displacement curves. MechAnalyze calculates the ultimate stresses and strains, as well as compressive moduli for hydrogels or tissues, but is not currently capable of calculating transition, yield, strain energy, or analyzing tensile data. Dots-on-Plots is unique in automating the analysis of tensile data for soft tissue, and importantly, is unique in being a web application. A striking advantage of web applications is they provide on-demand access to a scalable software platform. By eliminating barriers related to downloading and installing a software package on a particular operating system, web-based software becomes easily accessible to a worldwide research community. In the future, Dots-on-Plots can be expanded to analyze other types of stress-strain curves and other types of materials.

The automated calculation of mechanical properties with Dots-on-Plots can help researchers conduct an objective and comprehensive analysis of mechanical behavior. For example, our automated calculation of linear modulus can eliminate the subjectivity inherent in previous methods that defined modulus as the slope between two user-defined points [26,103]. Our program also automatically calculates strain energy density, which is a single scalar measure of material resilience and toughness [104] that can be calculated at yield [105], ultimate[106], and rupture points [107]. While strain energy density is often reported in biomechanical studies using computational models [108,109], it is not a commonly reported property in experimental studies of soft tissue. Automating this calculation could encourage research groups to consistently report this property, thus improving our understanding of tissue material behavior. Our study determined yield strength by finding the point on the stress-strain curve with a maximum positive slope, as this point indicates the beginning of strain-softening (Figure 12). For collagenous tissues, strain softening correlates with the onset of tissue damage in the form of unfolding collagens [82], though the precise location of this point along the stress-strain curve is debatable. To account for this uncertainty and support program flexibility (Table 4), Dots-on-Plots allows users to adjust the positioning of the yield point from the point of maximum slope. The downloadable files from Dots-on-Plots (PDF and CSV) provide an archivable record of all results and settings that can be readily included as supplementary data for journal articles.

An innovation of this project was the use of a constitutive model to determine the known (actual) transition strain from sets of stress-strain data. This allowed us to quantify the accuracy of Dots-on-Plots relative to a known answer. We selected a hyperelastic-damage model that 1) gave excellent fits to experimental stress-strain curves (Figure 14), and 2) included a material coefficient (λ_m) equivalent to the transition stretch, defined as the intersection of the toe and linear region (Figure 12). This model curve fitting served as a “gold standard” to quantify the error of our algorithm for calculating transition strains. We found that a 2% stress deviation threshold gave the best results, with a mean absolute error of 0.004 engineering strain for each individual experiment, corresponding to a mean absolute percent error of 8%. This level of accuracy was independent of stress-strain curves from young and older groups that exhibited different mechanical properties [91]. Moreover, if we examine the average transition strain for all twenty experiments using a 2% threshold in Dots-on-Plots (0.049) and compare to the average known transition strain using finite element parameter optimization (0.050), we see little overall difference between the methods (1.4% mean percent error). This gives us confidence that our algorithm for calculating transition strain can provide a fast and reliable alternative to time-intensive parameter optimization.

To determine whether the calculation of transition strain by Dots-on-Plots was sensitive to the shape of the input stress-strain curve, we analyzed a manufactured set of curves with unique shapes (Figure 15). We found that our algorithm was generally robust when analyzing data with different lengths of toe region and magnitudes of linear modulus, but was quite sensitive to damage onset (Figure 18). The late damage onset group gave the largest magnitude of transition strain error due the linear region of the stress-strain curve having a steady curvature that prematurely triggered the stress deviation threshold and resulted in large overpredictions of the transition strain. For this reason, we recommend increasing the threshold to calculate the transition strain when analyzing stress-strain curves with high yield strains.

The mechanical properties calculated in this study using Dots-on-Plots can be compared to previous biomechanical meniscus studies. Our calculated transition strain of 4.9% (Table 6; using the optimized 2% stress deviation setting) is close to the overall mean transition strain of approximately 5.4% that was computed in six previous meniscus studies using various methods to compute transition strain (Table 3). Our linear modulus value of 104 MPa is similar to the modulus values of 108 MPa and 96 MPa reported for human meniscus by Lechner et al., and Tissakht & Ahmed, respectively [7,26]. Importantly, our method for calculating the linear modulus, where we applied a linear fit to stress-strain data near the maximum slope of the stress-strain curve (Figure 13), gave excellent fits to our experimental data in this region, with an average NRMSE of 0.30 ± 0.12%. The goodness of fit persisted across the entirety of the linear region between the transition and yield point, maintaining an average NRMSE of 0.99 ± 0.53%. The close comparison of our calculated linear modulus to prior studies, and the quality and consistency of our linear fits, gives us confidence that our algorithm is accurately determining the linear modulus. It's also worth noting that the tensile properties computed by Dots-on-Plots are nearly identical to our prior analysis of this same set of tensile stress-strain curves [91]. This was expected, since the custom Matlab script used in our prior analysis was eventually converted into the Dots-on-Plots web application. The one exception is that the mean transition strain in the current study (4.9%) is larger than we previously reported (3.6%). The reason for this difference is that we used a 10% stress deviation threshold in our prior study, which we now know is too large a threshold to accurately estimate the transition strain (Figure 17).

This study has several notable limitations. First, Dots-on-Plots was designed to evaluate tensile pull-to-failure data of soft tissue, and may not be appropriate for analyzing other materials and test configurations (e.g. compression, shear). However, in practice, any stress-strain curve with a toe and linear region could be analyzed with Dots-on-Plots. For example, compression tests of intervertebral disc exhibit stress-strain profiles with a toe and linear region[110], and therefore could be analyzed using our software. Second, the optimal threshold value to calculate transition strain was determined from a single material (human lateral meniscus), which may not represent all variations in stress-strain behavior the program may encounter. To account for this, we 1) conducted sensitivity tests to better understand stress-strain shapes that could pose problems to our algorithm, and 2) designed the software to allow users to adjust threshold settings. Third, this study focused on a single set of algorithms to automate the calculation of transition and yield points, and the accuracy of other techniques to detect these points of interest were not quantified [7,12,14,93,111]. Nevertheless, the algorithms used in this study were shown to be accurate (Figure 17), and they have proven to be robust in previous work [6,13,91]. Finally, the program performs unitless calculations. While this provides program simplicity and user flexibility, it does mean that the accurate calculation of strain energy density is dependent on the user inputting stress and strain measures that are energy conjugates (e.g. engineering stress vs engineering strain, Cauchy stress vs true strain)[94].

In conclusion, this study has developed and evaluated a free, web-based program for the calculation of tensile mechanical properties. This program can provide researchers a fast, convenient, and reliable tool to analyze mechanical data, and along with other recent work from our group [13,70], can support the broad adoption of standard test methods for tensile testing of biological tissue.

4.5 Acknowledgements

Financial support kindly provided by the National Science Foundation under grant number 1554353 and the National Institute of Arthritis and Musculoskeletal and Skin Diseases under grant 1R15AR075314-01.

CHAPTER 5: FINITE ELEMENT MODELING OF MENISCAL TEARS USING CONTINUUM DAMAGE MECHANICS AND DIGITAL IMAGE CORRELATION[3]

5.1 Introduction

Meniscal tears are one of the most common musculoskeletal injuries, with more than a half-million occurring in the U.S. each year[1]. Once torn, the load attenuating capability of the semi-circular meniscus can become permanently compromised, leading to chronic knee joint pain and instability[112]. The meniscus also has a diminishing capacity to heal with age[16] and surgical interventions that remove damaged meniscal tissue increase the likelihood of osteoarthritis[113,114]. With the lack of effective treatment options to fully restore meniscus function, the prevention of meniscal tear injuries is of utmost importance. Meniscal tears are classified by their shape relative to the anisotropic collagen type I fiber matrix[18], which is primarily aligned circumferentially to resist the large tensile or hoop stresses that develop during joint compression[64]. Tears can occur alongside the fibers through the ground substance (e.g. horizontal and vertical tears), or can disrupt or break the circumferential fibers (e.g. radial and flap tears). Despite the prevalence and impact of this injury, the physical mechanism of meniscal tears is poorly understood.

Computational tools like finite element (FE) analysis can be utilized to help understand injury mechanisms in soft tissue, as well as inform the development of injury prevention strategies[9,115]. While many three-dimensional FE models of soft tissue structures in the knee and other joints have been created to analyze stresses and strains

---

[3] Reprinted from *Scientific Reports* Nesbitt DQ, Burruel, DE, Henderson, BS, Lujan TJ. “*Finite Element Modeling of Meniscal Tears Using Continuum Damage Mechanics and Digital Image Correlation.”* 2023 March 10; 13(1).[196]

during normal and pathological activities[37,116,117], FE models have not been developed to investigate meniscal injury mechanisms. One way that FE can be effectively used to simulate meniscal tears is by using Continuum Damage Mechanics (CDM) to model material weakening and eventual loss of load bearing capacity due to the onset and propagation of damage. Material damage is theorized to occur due to the breaking of chemical bonds[109] leading to the formation of microscopic voids[118]. This damage will irreversibly reduce the material's ability to resist deformation until material separation occurs (tissue tearing). Several studies have used CDM to successfully simulate the stress-softening behavior observed in stress-strain curves of soft tissue under tension[43–45,119,120], but no previous soft tissue study has used FE models to analyze the localized failure behavior in the tear region predicted by CDM.

A critical step in computational research is to perform a validation study to determine whether the model is able to simulate independent experimental data not used to calibrate (fit) the model parameters[121]. A validation technique useful for modeling mechanical failure is to compare FE predicted surface strains in the tear region to full field strain maps experimentally measured using digital image correlation (DIC)[47,122–127]. This approach is advantageous as it allows for the calibration and validation of a computational model using the same experimental data set; first by tuning model parameters to the grip-to-grip stress-strain behavior, then validating the model by comparing the localized surface strains predicted by the model and measured experimentally. This validation method has been used in FE models of bone fracture [122–124], but has not previously been applied to soft tissue. However, a study by Von Forell and Bowden did make a qualitative comparison between FE and DIC shear strains in tendon, demonstrating that CDM has potential to predict observed deformations in the tear region when using appropriate formulations to trigger and evolve damage[128]. Similarly, findings from our previous experimental work that used DIC with high-speed video to characterize tensile failures in human meniscus[91] can inform a constitutive framework for a physiological damage model. We found that when loaded along the fiber network (longitudinal), failures followed the plane of maximum shear strain. This suggests that macroscale fiber failures are driven by distortion energy, and therefore von Mises stress may be an appropriate damage criteria[46,91]. When loaded normal to the fibers (transverse), failures occurred along the plane of maximum normal strain. This suggests that macroscale ground substance failures are driven by first principal strain[91], and maximum normal strain may be an appropriate damage criterion. Further, our previous DIC measurements of localized strains in the tear region at precise points on the stress-strain curve can be used to validate whether CDM is capable of recreating the physiological strains occurring during meniscal tears.

The objective of this work was to determine if CDM can predict the anisotropic, macroscale failure behavior of human meniscal tissue under tensile loading. We hypothesize that a transversely isotropic hyperelastic damage model using von Mises stress damage criteria for fiber failures, and maximum normal strain damage criteria for ground substance failures, will be able to reproduce the stress-strain profile of quasi-static tensile tests and planar strain in the tear region.

5.2 Methods

5.2.1 Overview

Finite element analysis was used with CDM to simulate uniaxial tensile experiments of human meniscus. We analyzed two loading configurations (longitudinal, transverse) and two CDM damage criterion (von Mises stress, maximum normal strain). Model parameters were tuned to experimental stress-strain curves and quality-of-fit was measured. The tissue strains within the tear region of interest (ROI) were then compared to those measured experimentally by DIC in our previous work[91] to determine the accuracy of the model in predicting meniscal tears.

5.2.2 Tensile Tests using DIC

An in-depth description of the experimental methods for the uniaxial tensile tests can be found in our previous experimental paper[91]. In this prior study, human menisci were harvested from cadaveric knees that were obtained through an accredited tissue bank (Science Care Inc., Pheonix, AZ), and all experimental protocols were approved by the Institutional Biosafety Committee at Boise State University. In brief, 40 monotonic uniaxial tensile tests (loading rate = 1% strain/s) were conducting using specimens from five young human cadaveric menisci (age = 33 ± 5 years; BMI = 21 ± 1) and five older human cadaveric menisci (age = 72 ± 7 years; BMI = 26 ± 5). All knees had no medical history of injury or visible signs of damage or degeneration. Thin layers of meniscus were cut from both the anterior and posterior region[13], and punched into dumbbell shaped coupons[70] either along the preferred fiber direction (longitudinal) or normal to the preferred fiber direction (transverse). Specimens were speckled for DIC analysis, preloaded, mechanically preconditioned, and then preloaded again prior to being pulled to failure in tension. A high-speed camera and DIC software were used to measure planar strains from the start of testing to tissue separation (failure). Planar tissue strains were calculated in an ROI that was centered along the tear line of action and spanned the width and thickness of the coupon with a vertical height of 2 mm. These ROI strains were calculated at ultimate tensile stress, where the tissue begins losing load bearing capacity. Axial force and grip displacements were used to calculate the overall stress-strain curve for each specimen.

5.2.3 Damage Model

The selected constitutive model was a transversely isotropic hyperelastic[129] damage model available in FEBio[95], where the material's strain energy density Ψ is uncoupled into hydrostatic and deviatoric components of the ground substance F_1 and fiber matrix F_2:

$$\Psi = F_1(\tilde{I}_1, \tilde{I}_2) + F_2(\tilde{\lambda}) + \frac{K}{2}(ln(J))^2 \tag{7}$$

Here $\tilde{I}_1$ and $\tilde{I}_2$ are the first and second invariants of the deviatoric portion of the right Cauchy Green deformation tensor, $\tilde{\lambda}$ is the deviatoric part of stretch along the fiber direction, J is the volume change ratio, and K is bulk modulus, which was set to 1000 to enforce near-incompressibility[96]. Following previous research in ligament modeling[130,131], we used a Veronda-Westmann formulation for the ground substance (Eq. 8),[39,40] where strain energy is dependent on two material coefficients (C_1, C_2). A piecewise exponential function was used for the fiber network (Eq. 9), where the transition fiber stretch λ_m defines the transition between the toe and linear region.

$$F_1 = C_1\left(e^{(C_2(\tilde{I}_1-3))} - 1\right) - \frac{C_1 C_2}{2}(\tilde{I}_2 - 3) \tag{8}$$

$$\tilde{\lambda}\frac{\partial F_2}{\partial \tilde{\lambda}} = \begin{cases} 0 & \tilde{\lambda} \le 1 \\ C_3\left(e^{C_4(\tilde{\lambda}-1)} - 1\right) & 1 < \tilde{\lambda} < \lambda_m \\ C_5\tilde{\lambda} + C_6 & \tilde{\lambda} \ge \lambda_m \end{cases} \tag{9}$$

When the fiber stretch is below λ_m, the function is dependent on two material coefficients that effectively control fiber straightening (C_3, C_4). At a fiber stretch above λ_m, the fibers take on an approximately linear character, and are dependent on fiber modulus C_5, where C_6 ensures that stress is continuous at the transition stretch. The calculated strain energy density from the hyperelastic model is converted to an effective undamaged Cauchy stress $\boldsymbol{\sigma}_o$[95].

In order to model stress softening behavior, a quintic polynomial cumulative distribution function was implemented to apply damage evolution.

$$D(\Xi) = \begin{cases} 0 & \Xi \le \mu_{min} \\ x^3(6x^2 - 15x + 10) & \mu_{min} < \Xi < \mu_{max} \\ D_{Max} & \Xi \ge \mu_{max} \end{cases}, x = \frac{\Xi - \mu_{min}}{\mu_{max} - \mu_{min}} \tag{10}$$

Here D ranges from zero to a maximum damage (D_{max}), controlled by the limits μ_{min} and μ_{max}. Damage D is a function of the selected damage criteria (Ξ): von Mises stress (Eq. 11) or maximum normal Lagrange strain (Eq. 12).

$$\Xi = \sqrt{\tfrac{3}{2}\tilde{\boldsymbol{\sigma}}_o : \tilde{\boldsymbol{\sigma}}_o} \tag{11}$$

$$\Xi = Max\,(E_1, E_2, E_3) \tag{12}$$

where $\tilde{\boldsymbol{\sigma}}_o$ is the deviatoric part of undamaged stress $\boldsymbol{\sigma}_o$, and E_1, E_2, and E_3 are the principal values of Lagrange strain $\boldsymbol{E}$. This damage was applied to both the fiber and ground substance terms (Eq. 8-9). Finally, Cauchy stress $\boldsymbol{\sigma}$ was calculated by scaling the effective undamaged stress tensor $\boldsymbol{\sigma_0}$ with scalar damage D.

$$\boldsymbol{\sigma} = (1 - D)\boldsymbol{\sigma_0} \tag{13}$$

5.2.4 Finite Element Mesh and Coupon Geometry

Computational effort was reduced by modeling 1/8th of dumbbell shaped coupons along three planes of symmetry (Figure 19). Model dimensions reflected the average coupon dimensions measured experimentally for longitudinal (Figure 19a) and transverse (Figure 19b) specimens[91]. For boundary conditions, the grip was modeled as a rigid body with an irrotational sliding elastic tension contact at the top of the coupon, while the axis normal to each plane of symmetry was fixed.

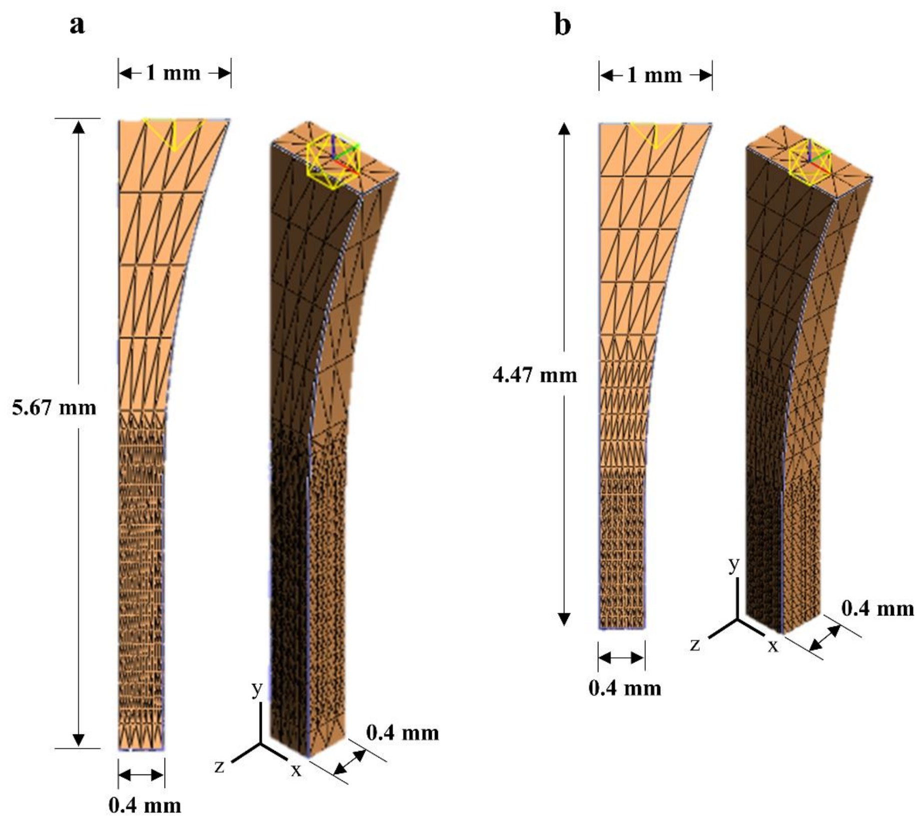

Figure 19: Coupon dimensions and mesh for all a) longitudinal and b) transverse models.

The three-dimensional models were meshed with 10 x 8 x 2 linear tetrahedral elements, then refined by four-fold in an approximately 2.5 mm tall region spanning the width and thickness of the coupon where the highest strain concentrations occurred prior to failure. This localized refinement was done to help reduce the premature model termination we observed in coarse meshes due to damage localization. A mesh convergence study was conducted to determine the effect of mesh refinement on tensile strain along the loading axis ($\underline{E}_{yy}$) when a grip-to-grip stretch of 1.20 was applied. Tensile strain was selected as the criteria for mesh convergence since strain is the outcome measure we're comparing to our prior experimental results[91]. The mesh convergence study found that refinement increased the tensile strain (E_{yy}; averaged in the ROI), although this increase exhibited a plateauing trend (Figure 20a). For this study, we selected a mesh size (16,144 elements; Figure 20b) that was computationally efficient (~1 min runtime) and gave strain results near the projected curve plateau (Figure 20a). Linear tetrahedral elements were selected for ease of mesh generation compared to more complex elements[132].

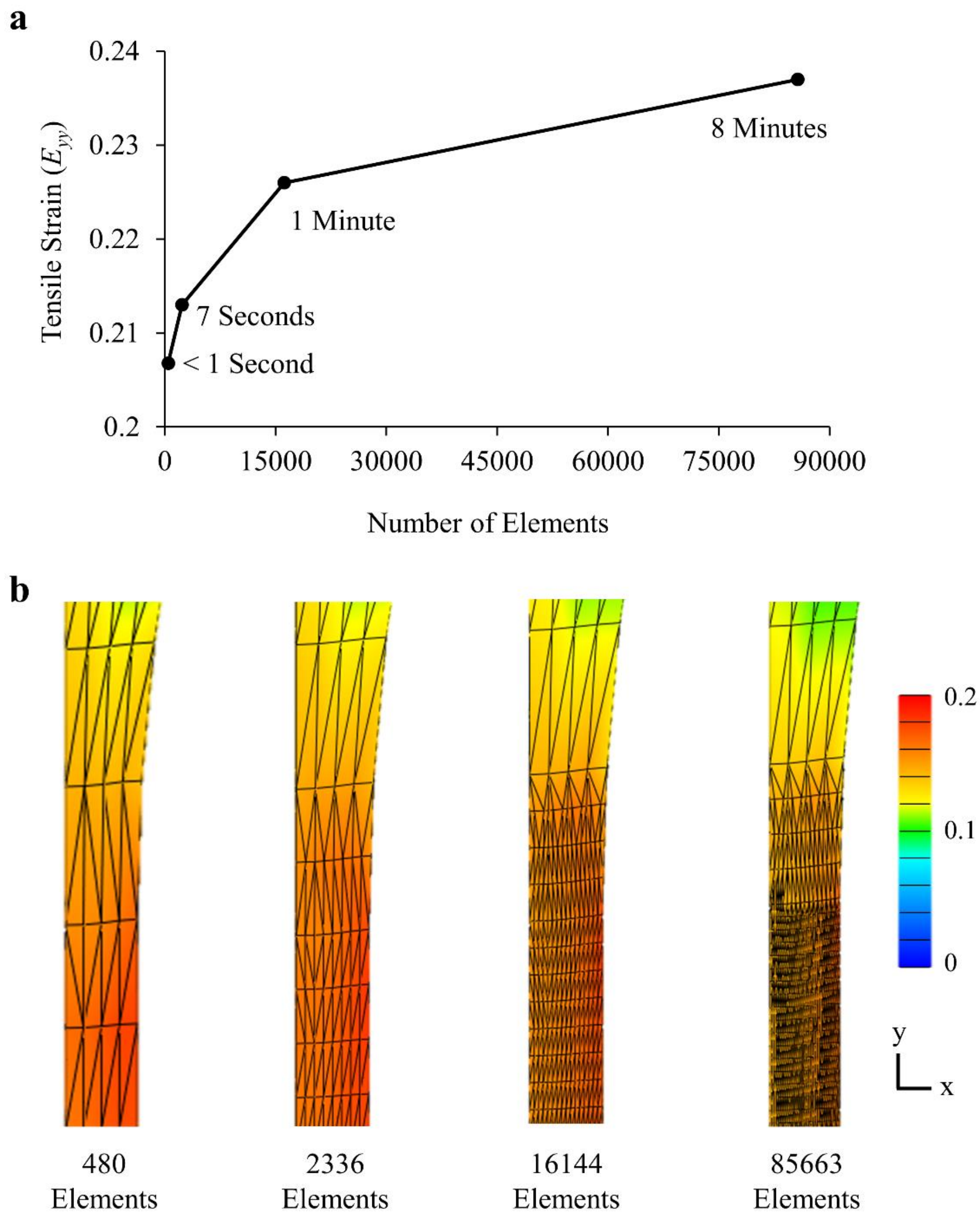

Figure 20: Mesh convergence study. a) Increasing mesh size resulted in longer run times and greater tensile strain (E_{yy}) inside the tear region that gradually plateaued. b) Strain maps (E_{yy}) of different mesh sizes. This study used 16,144 elements.

5.2.5 Parameter Optimization

Tensile tests were simulated by displacing the rigid body plate by the specimen specific grip-to-grip stretch, and comparing the axial force measured at the rigid body to the experimental axial force measured at the grip. In total, there were nine parameters to fit in the hyperelastic damage model: two ground substance parameters, four fiber parameters, and three damage parameters. The two parameters of the elastic ground substance (Eq. 9) were first fit to stress-strain curves of transverse specimens up to the yield point (point of maximum slope determined with Dots-on-Plots[133]) using the Levenberg-Marquardt parameter optimization module in FEBio[95,96]. The four parameters of the elastic fiber network were then fit to the stress-strain curves of longitudinal specimens up to the yield point, also using FEBio's parameter optimization module. For these optimizations, initial guesses for C_1, C_5, and λ_m were based on our previously measured mechanical properties[91], with optimization limits of more than ± two standard deviations. The initial guess for C_2 was set to one to enforce near incompressibility[130], and the initial guesses for the remaining elastic parameters were similar to a prior study[130] with limits of approximately double and one-half the initial guess, respectively. When optimization returned a parameter extremum, that extremum was expanded by 30% and optimization was reperformed. This process was repeated until the optimization returned parameters that were not extrema. The average values for the fitted elastic parameters were $C_1 = 0.78 \pm 0.66$ MPa, $C_2 = 1.20 \pm 1.8$, $C_3 = 0.43 \pm 0.23$ MPa, $C_4 = 40.83 \pm 9.95$, $C_5 = 119.63 \pm 50.07$ MPa, and $\lambda_m = 1.048 \pm 0.007$.

Once the elastic parameters were optimized, the three damage parameters were selected to best fit the stress-strain curve between the yield point and ultimate tensile strength (UTS). Automated optimization of damage parameters was not feasible, as the optimization module would often select a combination of parameters that resulted in early model termination and thereby caused the optimization routine to halt. Instead, model damage parameters were manually fit with specific success criteria, starting with initial guesses for μ_{min} and μ_{max} at yield strain and ultimate strain, respectfully. Models were considered successfully fit once model predicted ultimate stress and strain were within 0.2 MPa and 3% strain of the experimental ultimate stress and strain for longitudinal models, respectively; and 0.03 MPa and 3% strain for transverse models, respectively. A successful fit also required a post-UTS reduction in stress of at least 1% and 0.5% from the ultimate stress for the longitudinal and transverse models, respectively. The value of D_{max} was kept below 1 (no load carrying capacity when D = 1) to avoid model convergence issues that have been previously described[128,134]. Different damage parameters were used for the longitudinal and transverse specimens (Table 7), as damage onset of the ground substance occurs at much greater strains then fiber damage (Figure 21).

Table 7: Damage parameters for models loaded longitudinal or transverse to the fiber direction.

	Von Mises Stress Criteria			Max Normal Strain Criteria		
	μ_{min}	μ_{max}	D_{max}	μ_{min}	μ_{max}	D_{max}
Longitudinal	8.83 ± 9.26	43.66 ± 30.17	0.58 ±0.08	0.18 ± 0.21	0.48 ± 0.26	0.61 ± 0.09
Transverse	0.19 ± 0.26	2.20 ± 1.98	0.65 ± 0.13	0.12 ± 0.16	1.18 ± 0.68	0.73 ± 0.13

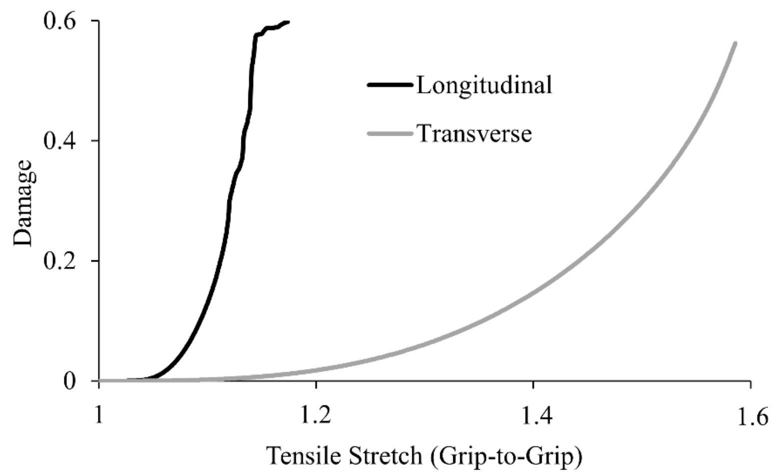

Figure 21: Maximum damage in the tear region of two representative specimens.

5.2.6 Model Evaluation and Validation

The failure ROI for the model spanned the vertical coupon edges and was determined as one element above and below the line-of-action of greatest damage concentration. This resulted in ROI height spans of 0.2 mm for all transverse models, 0.24 mm for longitudinal models with the von Mises criteria, and 0.3 mm for longitudinal models with the maximum normal strain criteria. These ROI heights are comparable to the 0.2 mm ROI heights from the DIC experiment[91] (Figure 22). The location and shape of this ROI was the same for all models within each group. Average normal and shear Lagrange strains (E_{yy}, E_{xx}, E_{xy}), principal strains (E_1, E_2), and maximum shear strain (γ_{max}), of the element surfaces in the ROI were output to a logfile, averaged, and compared to the planar Lagrange strains measured by DIC during the uniaxial tensile experiment (Figure 22a)[91].

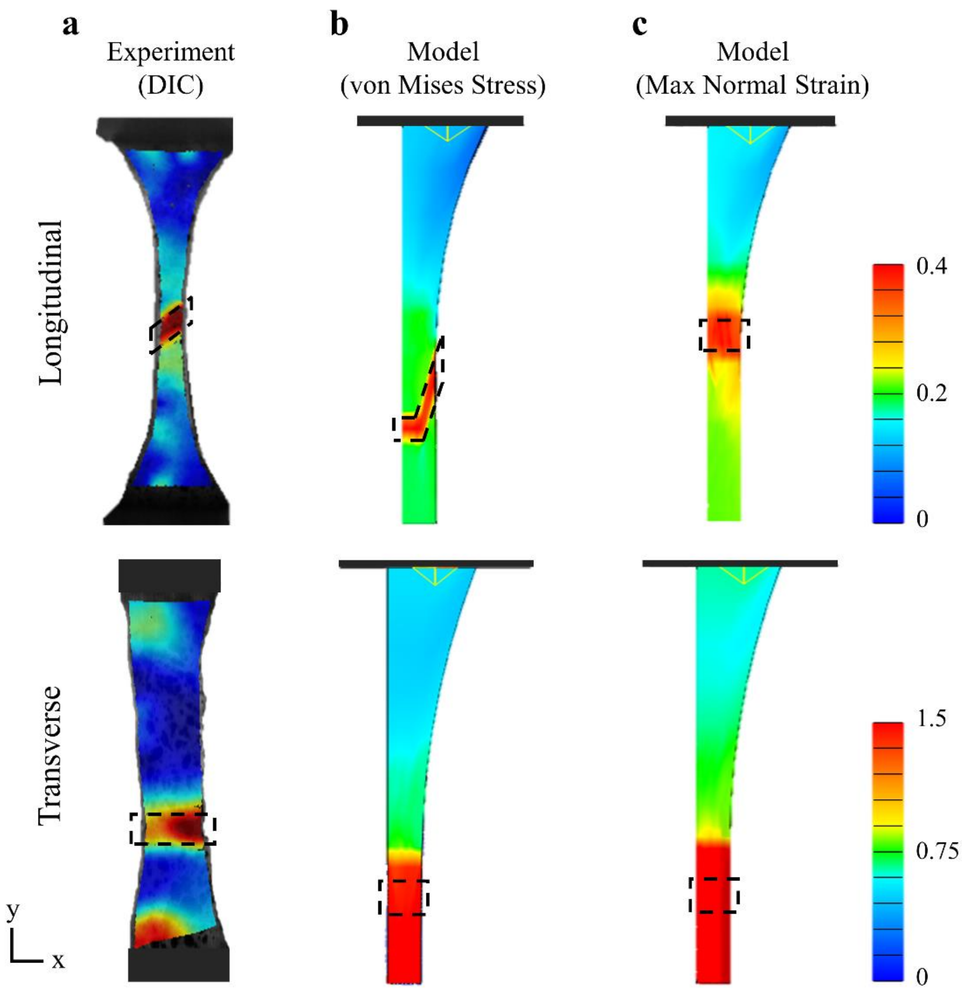

Figure 22: Normal strains (E_{yy}) from experiments and FE models for longitudinal and transverse specimens. A) The experimental tear pattern and strains in the tear region (ROI) measured with DIC were compared to model predictions using b) von Mises stress damage criteria, and c) maximum normal strain damage criteria. ROI are shown above by the dashed black box.

5.2.7 Statistics

Quality of fit between the experimental and model stress-strain curves was determined by calculating the NRMSE (normalized to mean stress) and coefficient of determination (R^2). The effect of damage criteria on quality of fit was determined using a one-way ANOVA. Differences in ultimate stress, ultimate strain, and average Lagrange strains within the tear region at UTS between the models and experiment were determined with a repeated measures ANOVA. All significance in this study was set at $p < 0.05$.

5.3 Results

5.3.1 Model Fit to Stress-Strain Curves

Finite element models were successfully fit to experimental stress-strain curves (Figure 23). Longitudinal models utilizing the von Mises stress damage criteria had significantly better quality of fits to experimental stress-strain curves relative to the maximum normal strain damage criteria ($p = 0.04$), with average NRMSEs of 2.10 ± 1.25% ($R^2 = 0.999 \pm 0.002$) and 2.92 ± 1.23% ($R^2 = 0.998 \pm 0.002$), respectively (Figure 23a, b). Transverse models using the maximum normal strain damage criteria gave better fits overall (Figure 23d), but were not significantly different than the von Mises stress damage criteria (Figure 23c) ($p = 0.07$), with average NRMSEs of 9.89 ± 5.83% ($R^2 = 0.96 \pm 0.05$) and 13.40 ± 6.09% ($R^2 = 0.93 \pm 0.06$), respectively. No significant differences existed in ultimate stress or ultimate strain between the models and experiments, for either loading orientation ($p > 0.99$) (Table 8).

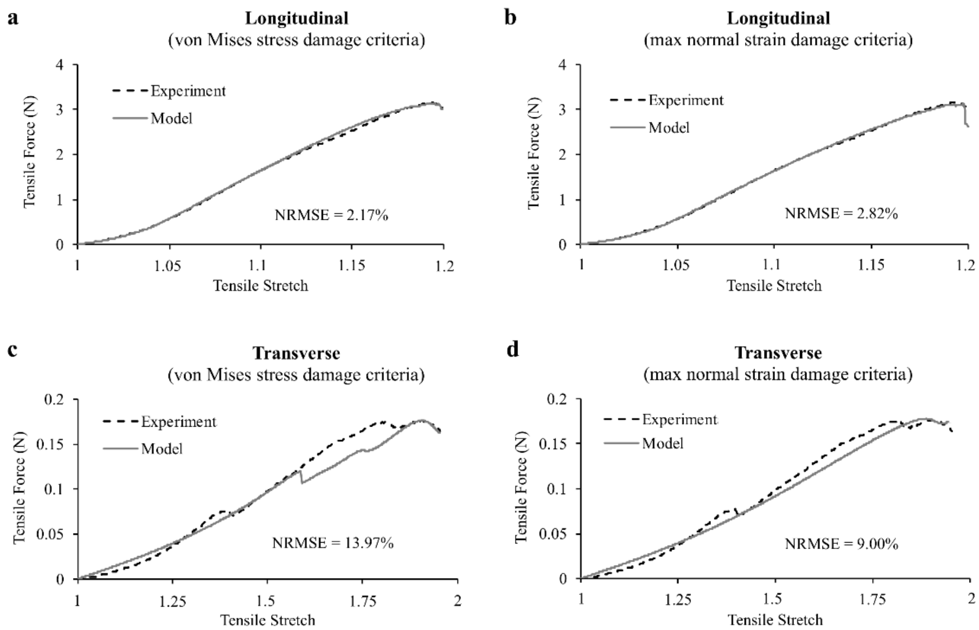

Figure 23: Representative model fits to experimental grip-to-grip force–displacement curves (we converted grip displacement to tensile stretch). (a) When modeling the fiber response (longitudinal), von Mises stress damage criterion had better fits compared to the (b) maximum normal strain damage criterion. (c) However, von Mises stress damage criterion had slightly poorer quality of fits compared to (d) maximum normal strain damage criterion when modeling the ground substance (transverse).

Table 8 : Comparison of mechanical behavior between damage models and experiments (sample size for each cell = 20). All strain values are reported as Lagrange strain.

	Longitudinal			Transverse		
	Experiment	Model (von Mises stress)	Model (max normal strain)	Experiment	Model (von Mises stress)	Model (max normal strain)
Ultimate Tensile Strength (MPa)	2.25 ± 1.42	2.25 ± 1.41	2.23 ± 1.39	0.100 ± 0.066	0.103 ± 0.068	0.100 ± 0.066
Ultimate Tensile Stretch (grip-to-grip)	1.155 ± 0.052	1.153 ± 0.053	1.155 ± 0.052	1.493 ± 0.214	1.491 ± 0.212	1.491 ± 0.216
Normal Strain E_{yy} (tear region at UTS)	0.29 ± 0.14	0.26 ± 0.11	0.27 ± 0.10	3.64 ± 3.30	**1.00 ± 0.46***	**1.02 ± 0.54***
Normal Strain E_{xx} (tear region at UTS)	0.01 ± 0.16	**-0.09 ± 0.07***	**-0.07 ± 0.03***	-0.21 ± 0.31	-0.15 ± 0.06	-0.15 ± 0.06
Shear Strain E_{xy} (tear region at UTS)	0.20 ± 0.10	0.14 ± 0.12	0.09 ± 0.06	0.529 ± 0.620	**0.017 ± 0.011***	**0.015 ± 0.008***
1st Principle Strain (tear region at UTS)	0.42 ± 0.14	**0.31 ± 0.16***	**0.29 ± 0.12***	3.78 ± 3.35	**1.00 ± 0.46***	**1.02 ± 0.54***
2nd Principle Strain (tear region at UTS)	-0.13 ± 0.10	-0.14 ± 0.12	-0.10 ± 0.05	-0.34 ± 0.08	**-0.15 ± 0.06***	**-0.15 ± 0.06***
Max Shear Strain (tear region at UTS)	0.28 ± 0.10	0.23 ± 0.13	**0.19 ± 0.08***	2.06 ± 1.70	**0.57 ± 0.25***	**0.59 ± 0.29***

* Significantly lower than experimental data within either Longitudinal or Transverse group (p <0.001).

5.3.2 Tear Region Strain

For the longitudinal group, normal axial strains (E_{yy}) in the tear region were not significantly different than experimentally measured strains for either the von Mises stress or maximum normal strain damage criteria ($p = 0.72$, $p = 0.87$, respectively) (Figure 24a, Table 8). The shear strains (E_{xy}) predicted by the longitudinal models using the von Mises stress damage criteria were approximately 30% lower than experiments ($p = 0.16$), and were approximately 50% lower than experiments when using the maximum normal strain damage criteria ($p = 0.003$) (Figure 24b, Table 8). For the transverse group, models using both damage criteria significantly underpredicted the experimental normal axial strains and shear strains ($p < 0.001$) (Figure 24c, d; Table 8). The contraction of the specimens within the tear region (E_{xx}) for all models was significantly less than experiments for the longitudinal group ($p < 0.05$), but not for the transverse group (p >

0.50).

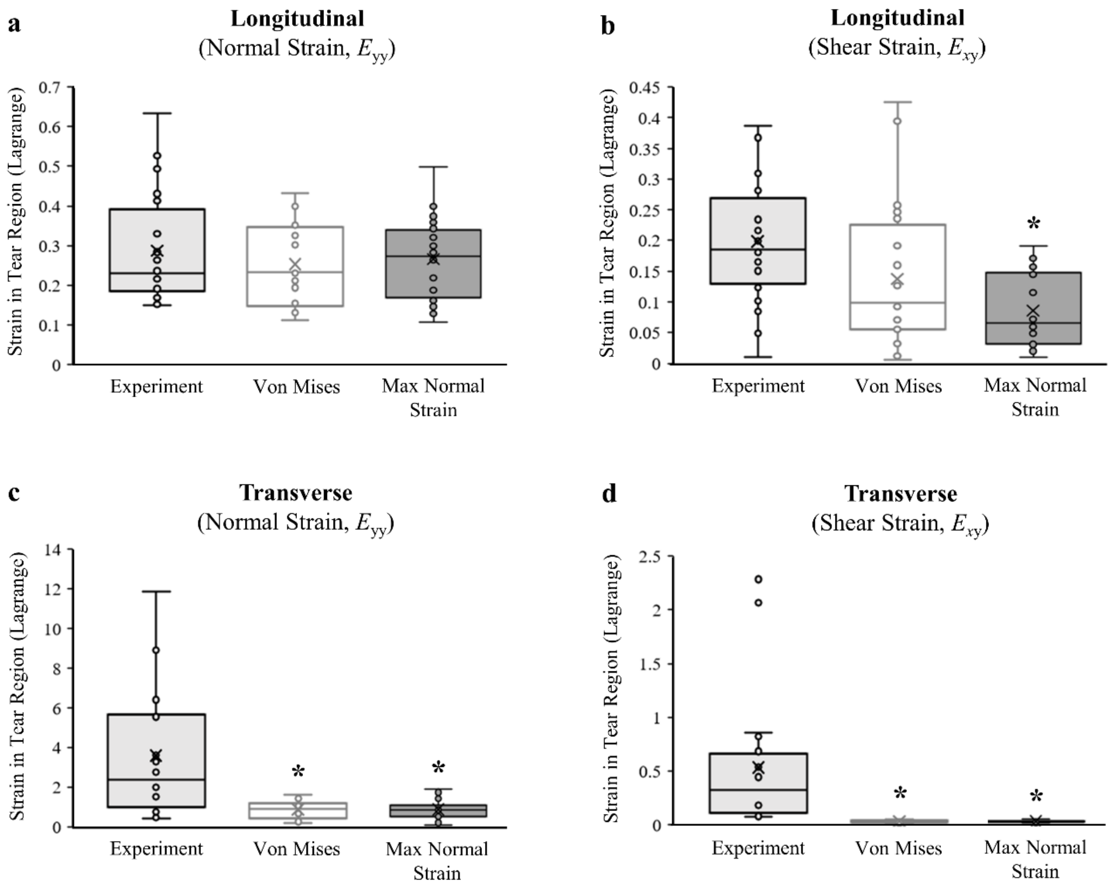

Figure 24: Comparison of strains in the tear region (ROI) between experiments measured using DIC and FE models generated with von Mises stress or maximum normal strain damage criterion. (a) Both damage criteria gave close predictions to the normal axial strains for the longitudinal loading condition, but (b) the maximum normal strain damage criterion significantly underpredicted the shear strains. (c) When loading transverse to the fiber direction, both models significantly underpredicted normal axial strains and (d) shear strains. *Significantly less than experimentally measured strains (p < 0.001). The 'x' in the box plot = average strain.

For longitudinal tests, first principal strains predicted by both the von Mises stress damage criteria and the maximum normal strain damage criteria were significantly lower than the experimental strains (p = 0.042, p = 0.013, respectively) (Figure 25a). The maximum shear strains predicted by both damage criteria were also less than experimental strains, but only maximum normal strain damage criteria were significantly less ($p = 0.046$) (Figure 25b). The second principal strains predicted by both damage criteria were similar to experimental strains ($p > 0.5$; Table 8). For transverse tests, first and second principal strains, as well as max shear strains predicted by both failure criterion were significantly lower than experimental strains ($p < 0.001$) (Figure 25c, d; Table 8).

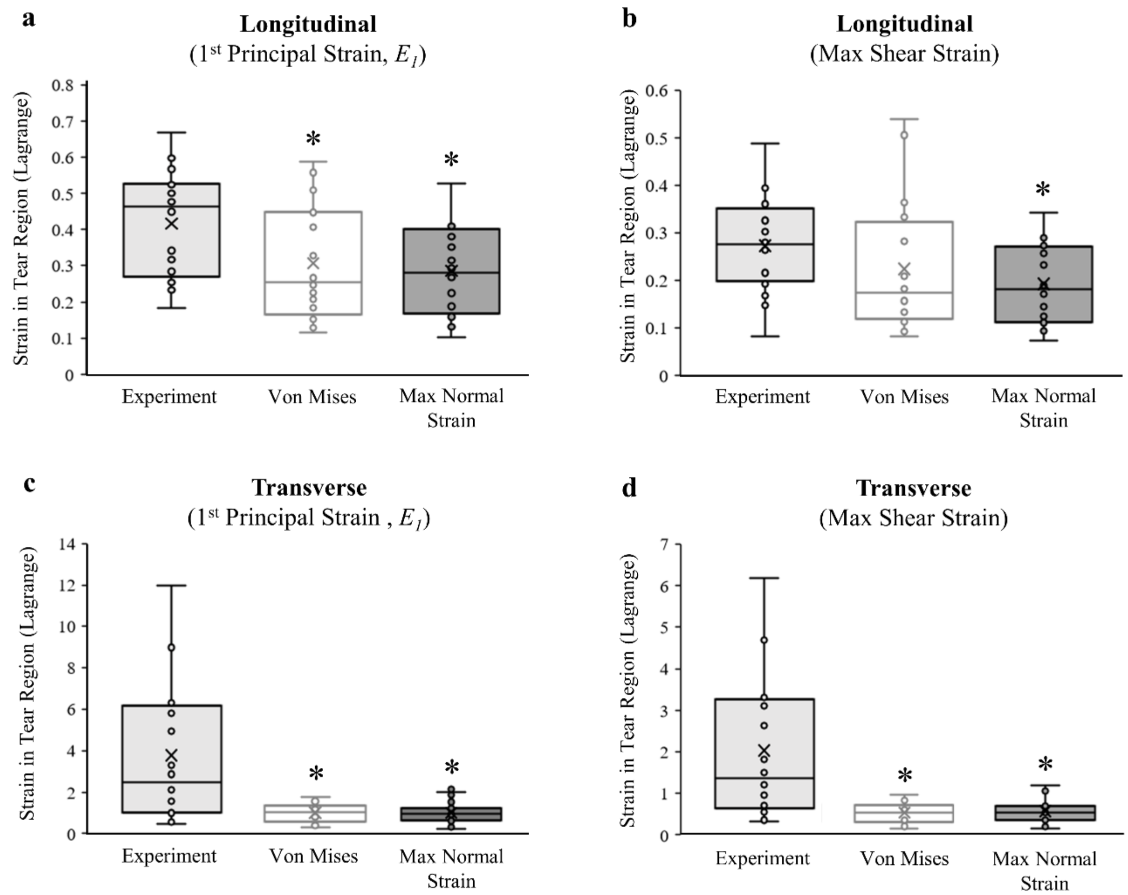

Figure 25: Comparison of principal strains in the tear region (ROI) between experiments measured using DIC and FE models generated with von Mises stress or maximum normal strain damage criterion. (a) Both damage criteria significantly under predicted the first principal strains for the longitudinal loading condition, but (b) only the maximum normal strain damage criterion significantly underpredicted the max shear strains. (c) When loading transverse to the fiber direction, both models significantly underpredicted first principal strains and (d) max shear strains. *Significantly less than experimentally measured strains ($p < 0.05$). The 'x' in the box plot = average strain.

For transverse models, both damage criterion predicted tears to propagate straight across the coupon at a 0 degree angle (i.e. perpendicular to the loading axis). For longitudinal models, the maximum normal strain damage criteria similarly predicted a 0 degree tear angle, however, longitudinal models using the von Mises stress damage criteria had tears initiate near the fillet an propagate at approximately 70 degrees, measured perpendicular to the loading axis (an angle of 90 degrees would be parallel to the loading axis), before changing angle at the midline of the coupon, where it continued propagating to the opposite boundary at 0 degrees. The average damage in these regions at UTS for longitudinal models was 0.26 ± 0.10 and 0.28 ± 0.16 for the von Mises and maximum normal strain damage criteria, respectively. For transverse models, the average damage was 0.59 ± 0.17 for both damage criteria.

5.4 Discussion

The objective of this study was to determine if finite element models using hyperelastic damage constitutive equations could simulate tears in the fibers and ground substance of human meniscus. We found that von Mises stress and maximum normal strain damage criteria were able to simulate the experimental anisotropic stress-strain curves (Figure 23), but in general, both damage criteria underpredicted the strains in the tear region. The one exception was that both damage criteria were able to reasonably predict normal strains along the loading axis for longitudinal tests. Also, the von Mises stress damage criteria was uniquely able to approximate the distinct tear angles for both fiber and ground substance failures. Overall, our findings partially supported our hypothesis and demonstrate limitations in using continuum level damage mechanics to simulate failure in soft fibrous tissue.

The excellent fits of our models to experimental stress-strain curves verified that the selected constitutive formulations were appropriate for modeling the grip-to-grip mechanical failure behavior of human meniscus. When loading the fibers (longitudinal tests), the piecewise strain energy function (Eq. 9) was able to fit the non-linear toe region[85] and linear region of the experimental data, and the damage formulation was able to fit the experimental stress-softening region where collagen damage accumulates[82]. As a result, our longitudinal models had an average R^2 value (> 0.99) better than other CDM modeling papers we surveyed for soft tissue[45,109,119,135–138]. When loading the ground substance (transverse tests), our model fits to experiments had average R^2 values (> 0.93) that were consistent with prior soft tissue studies[135,138]. Interestingly, many of the transverse experiments displayed localized stress peaks prior to UTS (Figure 23c, d), possibly indicating the sporadic failure of tie fiber groups, which run normal to the circumferential direction[64], and are stiffer and less extensible then the ground substance. We were able to recreate these localized peaks in our FE model by setting an upper limit to ground substance damage via D_{max} (Eq. 10). By limiting the maximum amount of damage, elements subjected to high strain concentrations that experience rapid damage would stabilize once maximum damage was reached, and would eventually support greater loads as the tissue continued to stretch. The ability of our model to match this experimental behavior supports the use of CDM for modeling ground substance failure, rather than fracture mechanics. This conclusion supports work by Peloquin et al., who conducted experiments with cracked meniscus tissue and concluded that fracture mechanics was not an appropriate failure analysis method for meniscal tissue[65].

The experimental validation of local strains in the longitudinal models exposed strengths and weaknesses of using CDM to model fiber failures. We were initially encouraged that both damage criteria could fairly accurately predict normal strains along the loading axis for longitudinal tests (Figure 24a), but when we examined the principal strains (Figure 25a), both damage criteria underpredicted the 1st principal strain in the tear region by approximately 30%. For comparison, previous studies that used DIC to validate an FE model of relatively hard materials (e.g. bone, steel) reported errors ranging from 7-24%[122–125,127,139], therefore our error is larger than desired. Our error is partially explained by the FE model underpredicting the E_{xy} shear strains that occur on the surface normal to the y-axis (Figure 24b). The larger E_{xy} shear strains in the experiments likely develop from collagen fiber sliding[76] that could potentially be simulated with a micromechanics model[140]. Since our model underpredicted 1st principal strain, we would have expected the 2nd principal strain to similarly be underpredicted, but on the contrary, the model predicted 2nd principal strains were a good match to experiments (Table 8). This disparity between principal strains indicates that our longitudinal models overpredicted the amount of lateral contraction during axial elongation, and that incompressibility is a poor physiological assumption when modeling the necking behavior that occurs in the tear region of fiber failures.

The experimental validation of strains in the transverse models demonstrated that a hyperelastic damage formulation is unable to capture the considerable extensibility of the ground substance in the tear region. In experiments, the ground substance elongated by more than 2.5 times its original length at UTS, while in the models, the ground substance extended to only approximately 1.75 times its original length at UTS (Table 8). This difference can be explained by discrepancies in the strain concentrations between the transverse experiments and models. The region of high strain concentration in the transverse experiments was a tight band of approximately 0.2 mm that propagated across the specimen surface, while the region of high concentration in the transverse models was a broad band of approximately 1.4 mm (Figure 22b, c). Our mesh convergence study shows that further mesh refinement in the tear region would result in only a nominal improvement in predicted strains and would not resolve this limitation (Figure 20a). Importantly, regularization methods commonly used to help FE damage models converge would likely only exacerbate this strain discrepancy, as these methods spread out localized deformation to prevent premature model termination[141,142]. A potential solution to simulate a tighter band of stress concentrations with CDM is to use region-dependent material parameters that effectively model localized defects within the tissue[143,144].

We evaluated two damage criteria in this study and found that von Mises stress offers two distinct advantages for modeling failure in soft tissue. First, longitudinal models that used von Mises stress damage criteria had slightly better overall predictions of 1st principal strain and maximum shear strain compared to models using maximum normal strain (Figure 25a, b, Table 8), although these differences were not significant. Second, models using von Mises stress damage criteria were better able to recreate the experimental tear angles. Longitudinal models with von Mises damage criteria had tears that initiated at the narrow section of the coupon fillet and propagated at a steep oblique angle until changing directions to propagate perpendicular to the loading axis (Figure 22b). This tear pattern is indicative of a classic cup-and-cone failure pattern seen in ductile materials[46], and was consistent with a subset of specimens in our previous experimental work that exhibited bimodal tear angles, characterized by steep initial tear angles that similarly “flattened” or changed direction near the coupon center axis[91]. The von Mises stress damage criteria was also able to model the “flat” tear angle of the transverse specimens near the coupon midsubstance where necking minimizes the cross-sectional area, thus maximizing 1st principal stress. Mathematically, since the 2nd and 3rd principal stresses are negligible near the midsubstance (simple tension), the von Mises equation simplifies to a maximum normal stress damage criteria and the tear would propagate perpendicular to the loading axis. It is therefore possible to use von Mises stress damage criteria to model the anisotropic tear patterns of meniscus, and other transversely isotropic soft fibrous tissues (e.g. ligament, tendon), however, different damage parameters would need to be used for the fibers and ground substance (Table 7). Not surprisingly, the maximum normal strain damage criteria simulated tears perpendicular to the loading axis near the midsubstance in both longitudinal and transverse groups (Figure 22c), as this region experiences the most necking and axial strain. Maximum normal strain damage criteria would thereby be an appropriate model to predict tear patterns in the ground substance, but not the fibers.

This project was innovative by being the first to quantify whether a damage model can accurately predict the deformation in the tear region of soft tissue. Other soft tissue damage models have simulated the physiological deformation of the overall structure[109,145], but not the localized deformation within the tear region. By comparing the model predicted surface strains and tear angles to the experimentally measured ones, we were able to determine whether the mathematical mechanisms driving model predicted failure are physiologically relevant. To our knowledge, this is also the first FE study of human meniscus to successfully simulate stress-strain curves to UTS (Figure 23), as previous FE models of the meniscus disregarded any failure or softening behavior[37–39]. These novel contributions help advance scientific efforts to develop and validate computational tools that can reliably simulate mechanical failure in connective tissue, and thereby allow clinicians and researchers to visualize model outcomes with direct clinical significance (i.e. tissue tears) with a goal of designing new treatment and prevention strategies for meniscal injuries and other musculoskeletal disorders.

This work had notable limitations. First, we were unable to utilize FEBio's parameter optimization plug-in to calibrate the damage parameters to the experimental stress-strain curves, as any combination of parameters that resulted in early model termination would halt the optimization routine. We instead manually fit these damage parameters to achieve a set of objective success criteria, and this resulted in stress-strain curves with excellent fits (Figure 23, Table 8). Second, this study used a large number of linear tetrahedral elements and the use of other element types (e.g. quadratic tetrahedral, linear or quadratic hexahedral) may result in different strain calculations[146]. Next, our finite element models only investigated tears that develop under tensile loading, and did not consider the effects of compression on meniscus failure. The models also did not consider variable loading rates, which would require the implementation of a viscoelastic constitutive framework. Lastly, our model validation study used two-dimensional surface strains and may have missed important phenomena in out-of-plane strains and tear patterns. However, we did account for this limitation by only comparing the two-dimensional surface strains and tear patterns of our finite element model to the experimental results.

In conclusion, this study has quantified the ability of continuum damage FE models to predict tearing in meniscal tissue subjected to tensile loads. This work provides a benchmark for the ongoing development and validation of computational models that accurately simulate tears in soft fibrous tissues.

5.5 Acknowledgements

Financial support kindly provided by the National Science Foundation under award number 1554353 and the National Institute of General Medical Sciences under award number P20GM109095.

CHAPTER 6: Age-Dependent Changes in Collagen Crosslinks Weaken the Mechanical Toughness of Human Meniscus

6.1 Introduction

Injuries to the human meniscus are common, and have been shown to lead to the early onset of knee osteoarthritis (OA)[1]. Over a half-million meniscal surgeries are performed annually in the U.S. to address joint pain and instability[1], and as we age, the menisci become more susceptible to injury[19,63] and less amenable to repair techniques[147]. This increase in injury incidence is likely due to changes in the mechanical integrity of the meniscus as we age, such as reduced elasticity[148], or a loss of capacity to absorb energy (toughness) during joint compression[91]. The age-related changes to tissue composition and organization that cause these functional deficits need to be determined to better understand knee pathophysiology and ultimately help design interventions to prevent or delay these prevalent injuries.

The mechanical integrity of the meniscus is provided by groups of structural proteins that may increase or decrease as we age. In meniscus, the proteins chiefly responsible for providing strength are collagens, with collagen I (Col1) being the most abundant. Col1 forms a durable fiber network that is primarily aligned circumferentially along the semi-circular shape of the meniscus (Figure 26) to resist the large tensile or hoop stresses that develop during joint compression[64]. The second most abundant protein is collagen II (Col2), which forms smaller, more randomly aligned fibrils that interact with proteoglycans[149] to resist compressive loading via osmotic pressure[23]. Other collagens that perform minor roles in the structure of the extracellular matrix (ECM) are also present in lesser quantities[150–152]. Non-collagenous proteins also play important roles in the structural integrity of the meniscus, including decorin and bigylcan which help to form and bind other ECM proteins to the collagen network[150–152]. In addition, prolargin assists in binding proteoglycans to the ECM[153], and elastin, which is around 1000 times more flexible than collagens, assists in resilience and elasticity of the tissue[154].

The effect of aging on the structural proteins in meniscus is poorly understood. Two prior studies noted an increase of decorin with aging[155,156], and others measured age-related changes to the organization of the fiber matrix[157,158], as well as surface fraying and the development of calcified regions[68]. Another group of studies primarily focused on degeneration and OA, and found that meniscal strength was significanctly reduced in joints with advanced degeneration and OA[25,157,159]. However, no study to our knowledge has comprehensively analyzed age-related changes in the molecular composition of healthy meniscus. Moreover, the structural origins for the age-related loss in mechanical toughness observed in healthy meniscal tissue[91] is unknown.

A likely molecular contributor to age-related changes in mechanical behavior are collagen crosslinks. Crosslinks can form normally as the collagen matures[160], providing strength or assisting with normal mechanical function. Abnormal crosslinks can also accumulate over time as advanced glycation end-products (AGE's), in which glucose spontaneously condenses with the lyslyl and hydroxylysyl side chains of collagen, forming crosslinks between the collagen triple helices (Figure 26)[161]. Senescent

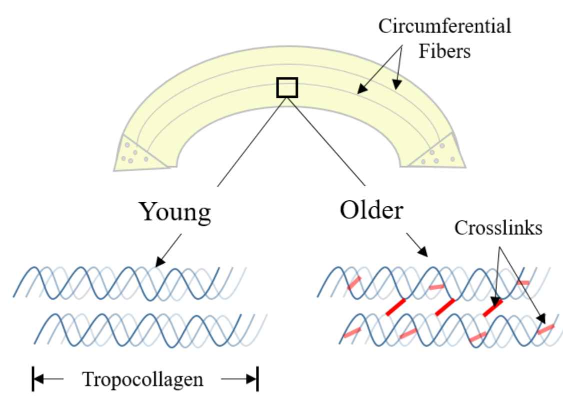

Figure 26: Graphic representation of the human meniscus gaining spurious collagen crosslinks with age.

collagen crosslinking by AGE's have been observed in human meniscus[55], and have shown a particularly pronounced effect in other tissues, as the induction of AGE's increase tissue stiffness[56,57,162–165]. The increase of AGE's has also altered mechanical properties in other fibrous soft tissues, such as reduced viscoelasticity in tendon[76], accelerated osteoarthritic degeneration in cartilage[58], and reduced elasticity in intervertebral disks[165]. This suggests that these AGE molecules can have a negative functional consequence to the tissues in which they accumulate. The objective of this work was to quantify changes in the structural proteins and collagen crosslinks of meniscus due to aging, as well as to determine the relationship between these molecules and tissue toughness. We hypothesize that a strong negative correlation would exist between the quantity of AGE collagen crosslinks and tissue toughness.

6.2 Methods

6.2.1 Overview

We determined proteomic profiles and collagen crosslinks within young and older populations of human lateral menisci via two mass spectrometry methods, and total elastin was measured by a colorimetric assay. Age-related changes in protein quantity were measured, and changes in collagen crosslinking were correlated to changes in tensile mechanical properties measured within the same set of tissue.

6.2.2 Specimen Preparation

A total of 40 meniscus specimens were prepared from the lateral menisci of 10 unpaired fresh frozen human cadaveric knee joints (femur to tibia), with five knees from donors under the age of 40 (age = 33 ± 5 years; 3 male and 2 female), and five knees from donors over the age of 65 (age = 72 ± 7 years; 4 male and 1 female). No medical history of injury and no visual signs of meniscus damage or degeneration was associated with donor knees. All experimental protocols were approved by the Institutional Biosafety Committee at Boise State University. Meniscus specimens were layered from the anterior and posterior regions of the meniscus[91] and then punched into dumbbell-shaped coupons for mechanical testing either parallel (longitudinal) or perpendicular (transverse) to the circumferential fiber direction[13,91]. The tissue adjacent to the dumbbell-shaped coupons was collected for proteomic and crosslink analysis (Figure 27). Dry tissue was carefully weighed using a high-precision benchtop scale (accuracy ± 0.01 mg; AT201, Mettler Toledo, Columbus, OH, USA) before being macerated, separated, and labeled for biochemical analysis.

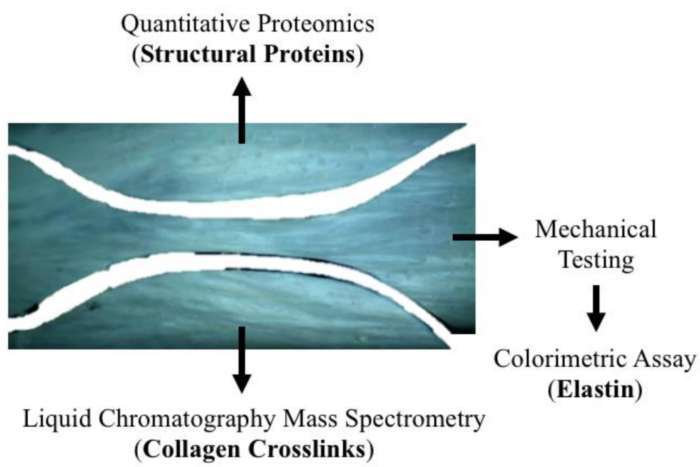

Figure 27. Specimen Preparation. Meniscus layers (n=40) were punched into three parts. The dumbbell-shaped part was used for mechanical testing and elastin analysis, while the adjacent parts were used to analyze proteomics and collagen crosslinks.

6.2.3 Mechanical Testing

An in-depth description of the mechanical testing method can be found in our previous study[91]. In brief, monotonic uniaxial tensile tests to failure were performed on all 40 dumbbell-shaped coupons (Figure 27). The longitudinal and transverse groups allowed us to capture the anisotropic nature of the human meniscus by measuring the circumferential fiber response and the ground substance response, respectively. Specimens were preloaded, mechanically preconditioned, and then preloaded again prior to being pulled to failure in tension at 1% strain/second. Specimens were kept hydrated using a 0.9% saline solution spray, and filmed during the pull to failure using a high-speed camera to enable digital image correlation (DIC). The DIC was used to measure the localized engineering strains in a 0.2 mm ROI along the tear line. Axial force and grip displacements were also used to calculate the stress-strain curve for each specimen. This curve was analyzed to calculate the tensile toughness (area under stress-strain curve up to the ultimate tensile stress) using a custom program called "Dots-on-Plots"[133].

6.2.4 Quantitative Proteomics (ECM Structural Proteins)

Quantitative proteomics were performed in collaboration with the University of Arkansas for Medical Sciences under the IDeA National Resource for Quantitative Proteomics program[166]. Meniscal tissue (10.3 ± 0.5 mg, n=40) was minced and homogenized with a bead mill in 300 μL of RIPA buffer along with HALT protease and phosphatase inhibitor. Samples were placed on ice in between bead mill pulses to prevent excessive heat production. Samples were then agitated on a shaker at 4 °C for 30 minutes before a 24-hour incubation at 4 °C. This process was repeated two more times, skipping the incubation on the third cycle to be centrifuged at 12,000 x G for 10 minutes at 4 °C. The supernatant was removed and the sample was centrifuged again to separate more of the supernatant. This supernatant was vortexed to ensure protein solution homogeneity before quantifying the protein concentration and quality with a BCA assay kit and SDS-PAGE electrophoresis. Fifty μg of protein for each sample was then shipped on dry ice from Boise, Idaho to Little Rock, Arkansas, where a 20-sample data independent acquisition quantitative proteomic platform (Orbitrap Fusion Lumos, Thermo Fisher Scientific, Waltham, MA, USA) was used to characterize ECM protein makeup of each sample[166]. From this proteomics analysis, $\log_2$ fold changes of protein quantity were compared between age groups, and we narrowed down to nine extracellular proteins that have been associated with mechanical function (Col1, Col2, Col4, Col6, Col8, decorin, prolargin, biglycan, fibromodulin)[23,150,153,167–172] (Figure 28). The mass spectrometry proteomics dataset used in this study has been deposited to the MassIVE repository[173].

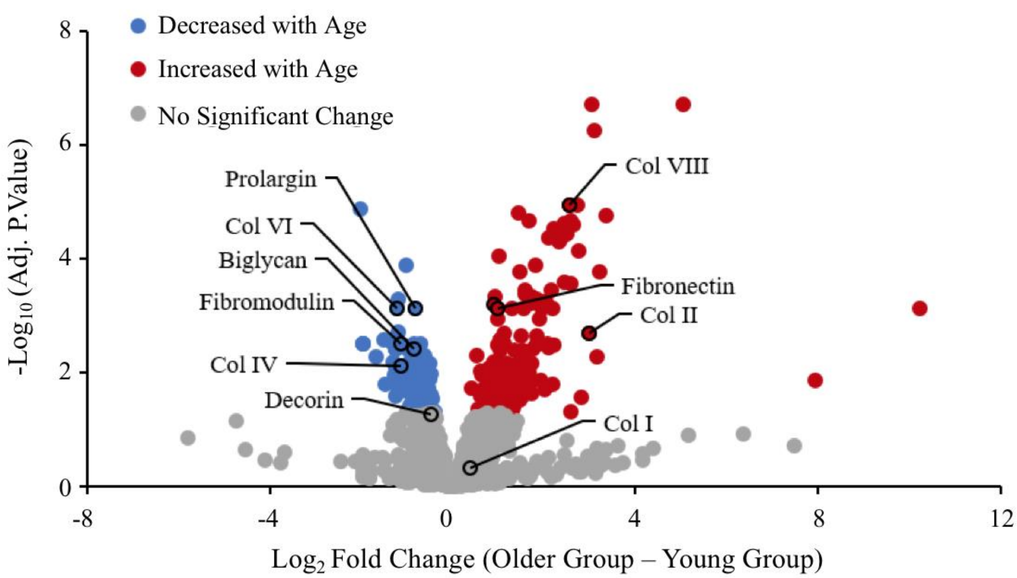

Figure 28: Volcano plot comparing proteins in young and older human meniscus. Aging resulted in either significant increases or decreases in most of the structural proteins analyzed in this study.

6.2.5 Liquid Chromatography Mass Spectrometry (Collagen Crosslinking)

Collagen crosslinking was quantified using liquid chromatography mass spectrometry. To prepare the tissue for this analysis, the tissue (15.3 ± 4.1 mg, n=40) was finely diced and reduced with sodium borohydride. Sodium borohydride was dissolved in 1 mM NaOH, and added to give a 1:30 ratio of sodium borohydride to tissue, and reduction was allowed to proceed for 2 h at 37 ºC. The reaction was quenched by adjustment to pH 3 with glacial acetic acid, centrifuged, and the supernatant discarded. Reduced samples were hydrolyzed in 0.5 mL of 6 M HCl at 105 ºC for 24 h. The acid was evaporated and the hydrolyzed sample resuspended in 250 µL of a 5% cellulose slurry in 4:1:1 butanol: glacial acetic acid: water. This was added to a syringe column containing 0.2 g of cellulose, spun, and was washed 3 times with 0.5 mL of the butanol: glacial acetic acid: water mixture. Crosslinks were eluted with 5 washes of 250 µL water, dried and resuspended in 100 µL of 50% methanol.

Liquid chromatography separation was then achieved using a Cogent Diamond Hydride column (MicroSolv Technology Corporation, Leland, NC, USA), a silica hydride column, using an aqueous normal phase chromatographic approach based on a previously described methods[174,175]. The gradient started at 90% acetonitrile: 10% water for 3 min, followed by a 15 min gradient to 25% acetonitrile: 75% water, held for 2 min, and returned to 90% acetonitrile and equilibrated for 5 min. Total run time was 25 min and flow rate was 0.2 mL/min. Mass spectrometry detection was achieved using an ultra-high-resolution Quadrupole Time of Flight (QTOF) instrument (Bruker maXis, Billerica, MA, USA). The electrospray ionization source was operated under the following conditions: positive ion mode, 1.2 bar nebulizer pressure, 8 L/min flow of N_2 drying gas heated to a temperature of 200 ºC, 3000 V to −500 V voltage between HV capillary and HV end-plate offset, mass range set from 80 to 800 *m/z*, and the quadrupole ion energy at 4.0 eV. Sodium formate was used to calibrate the system in the mass range of 80 to 800 *m/z*. The injection volume for all samples was 10 µL. The Compass Data Analysis software package (Bruker Corporation) was used to identify two crosslinks specific to collagen 1: deoxypyridinoline (DPD) and dihydroxylysinonorleucine (DHLNL); as well as two AGE's: carboxymethyl-lysine (CML) and pentosidine (PEN).

6.2.6 Colorimetric Assay (Elastin)

The quantitative proteomic analysis was unable to detect elastin, and therefore elastin was quantified from meniscus samples using the Fastin Elastin colorimetric assay kit (Biocolor Life Science Assays, Newtonabbey, UK). Briefly, dry samples were weighed and minced (11.8 ± 1.6 mg, n=40) before incubating in 0.25M oxalic acid at 100^{o}C for 1 hour. Solubilized elastin was precipitated before binding to dye according to the kit directions. Dissociated dye was read at 513 nm and total elastin mass in each sample was determined using a standard curve generated from known concentrations of elastin. Elastin content was normalized to dry weight.

6.2.7 Statistical analysis

Proteomics comparisons (young vs. older) were made by fitting a repeated-measures one way ANOVA to the $\log_2$-fold protein amounts of each sample. We used the limma library (Richie, 2015) with version 4.3.0 (R Core Team, 2023) in the Rstudio environment (Rstudio Team, 2020) to apply a moderated t-test following an established workflow[176]. Raw *p*-values were adjusted using a false discovery rate[177]. The effect of age (young vs. older) on elastin amount was determined using an ANOVA, and the effect of age on collagen crosslink amount was determined using a MANOVA, with a Tukey HSD post-hoc when significance was detected. A Fisher's exact test was used to determine the effect of age on the detection of pentosidine. Multiple regression analyses were performed to correlate amounts of structural proteins and collagen crosslinks with mechanical toughness. These two groups of molecules were analyzed relative to the loading orientation (four unique multiple regression tests). A backwards stepwise methods was used to identify predictive variables. These regression analyses were completed with SPSS software (IBM; Armonk, NY, USA; v24) and an R based web application[178].

6.3. Results

6.3.1 Age-Dependent Changes in ECM Structural Proteins

The quantity of ECM structural proteins was significantly different between age groups (Figure 29,Table 9). Col2 and Col8 had the greatest age-associated increases of more than 2 $\log_2$-fold ($p < 0.01$). Conversely, the quantity of Col4, Col6, and fibromodulin decreased by over 1 $\log_2$-fold ($p <0. 01$), and biglycan and prolargin also significantly decreased with aging ($p < 0.01$). There were no significant changes in the qauntity of decorin or Col1 associated with age ($p = 0.053$ and $p = 0.47$, respectively). Elastin increased from 18.5 ± 6.5 µg/mg in the young donor group to 20.6 ± 8.9 µg/mg in the older donor group, but this $\log_2$-fold change of 0.16 was not a significant increase (*p* = 0.39).

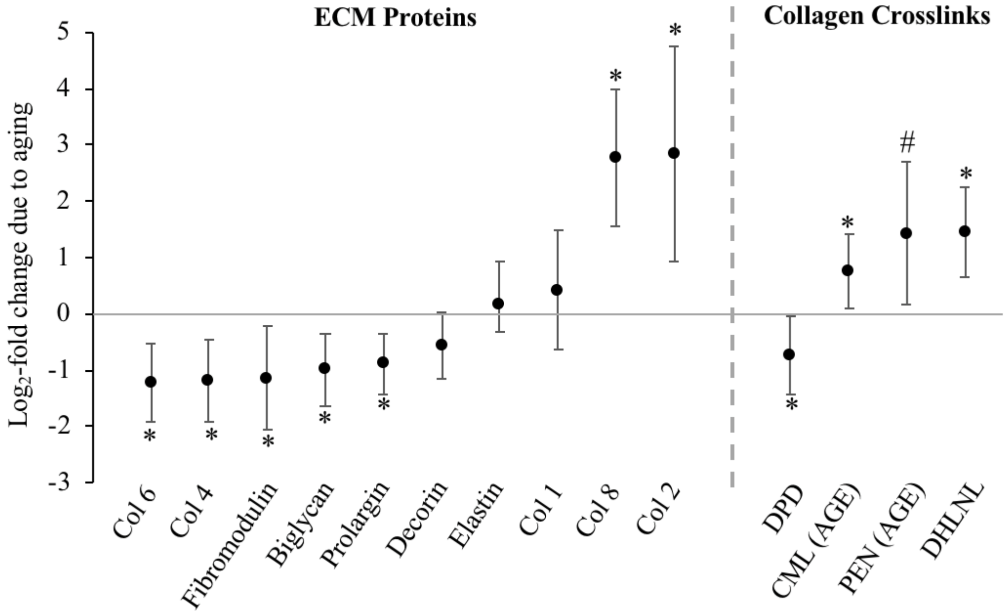

Figure 29: Log2 fold change of structural ECM molecules due to age ($p < 0.05$). Error bars show the 95% confidence interval of the $\log_2$ fold change.

Table 9:Effect of Aging on ECM Proteins and Collagen Crosslinks in Meniscus

	Molecule	Structural Role	Log_2-Fold Change with Age	CI (95%)
ECM Structural Proteins	Collagen IV	Main structureal component of the basement membrane[167].	-1.24*	-2.04, -0.44
	Collagen VI	Transmits mechanical load between the extracellular and pericellular matrix[168,179].	-1.19*	-1.71, -0.66
	Fibromodulin	Binds to collagen regulating fibrillogenesis and influences crosslinking[169].	-1.14*	-1.67, -0.61
	Biglycan	Assists in mineralization of connective tissues[170]. Regulates ECM turnover[180].	-0.85*	-1.25, -0.44
	Prolargin	Binds Col1 and Col2 to basement memberanes[181].	-0.82*	-1.16, -0.49
	Decorin	Assists in ECM assembly and promotes adhesion between aggrecan and collagen II[150].	-0.47*	-0.82, -0.12
	Elastin	Provides elasticity, and improves resilience and extensibility[154,182].	0.16	-0.33, 0.92
	Collagen I	Key structural component resisting tensile loads in connective tissue[149,171].	0.39	-0.32, 1.11
	Collagen VIII	Assists in forming a porous structure to withstand compressive forces[52].	2.56*	1.82, 3.29
	Collagen II	Interacts with proteoglycans[8] to improve compressive strength via osmotic pressure[9].	3.00*	1.67, 4.34
Collagen Crosslinks	DPD	Mature collagen crosslink that supports tensile stiffness and strength[55,160].	-0.74*	-1.43, -0.05
	CML	An AGE associated with loss of toughness in bone that increases skeletal fragility[184,185].	0.74*	0.08, 1.40
	PEN	An AGE associated with loss of toughness in hard and soft tissues[55,184].	1.43*	0.17, 2.70
	DHLNL	Immature collagen crosslink present during tissue remodeling[160].	1.43*	0.66, 2.24

6.3.2 Age-Dependent Changes in Collagen Crosslinks

The quantity of collagen crosslinks was significantly associated with aging (Table 9,Figure 29). The AGE crosslinks CML and PEN both increased with aging, with CML increasing by 0.74 log_2-fold (p=0.001) and PEN being detected in four times more older specimens than young specimens (p=0.004). In the enzymatic crosslinks, the qauntity of DHLNL increased with aging by 1.45 log_2-fold (p<0.001), whereas DPD decreased on average by 0.74 log_2-fold (p=0.032).

6.3.3 Relationship between ECM Proteins, Toughness, and Aging

Weak to moderate significant correlations existed between ECM protein qauntity and toughness when using simple regression analysis (Table 10). These included Col4, Col8, and prolargin, with Col8 having a moderate negative correlation of -0.51 under longitudinal loading. Multiple linear regression indicated a moderate collective significant effect between ECM proteins and toughness for longitudinal loading (p = 0.023, R^2_{adj} = 0.22), and a weak collective non-significant effect for transverse loading (p = 0.091, R^2_{adj} = 0.10). Multiple regression did not detect any individual significant correlations (Table 10), but a backward stepwise method did determine that Col8 was a significant predictor for tissue toughness under longitudinal loading. Aging had significant interactions with the slope between ECM protein quantity and toughness, where older specimens had a more positive slope than young specimens for Col1, Col4, and Col6.

Table 10: Relationship between ECM protein Quantity and toughness during uniaxial pull-to-failure tests either parallel (longitudinal, sample size = 20) or perpendicular (transverse, sample size= 20) the circumferential fiber orientation.

Loading Orientation	Protein	Simple Regression		Multiple Regression					
		r	p	β	t	p	Partial r	Tol	VIF
Longitudinal	Col1	0.08	0.36	0.17	0.41	0.69	0.12	0.30	3.39
	Col2	-0.31	0.094	0.15	0.41	0.83	0.06	0.12	8.11
	Col4	0.41	**0.036***	0.00	0.22	1.00	0.00	0.22	4.50
	Col6	0.37	0.055	0.21	0.00	0.70	0.11	0.19	5.35
	Col8	-0.51	**0.011***	-0.48	0.40	**0.13†**	-0.42	0.60	1.66
	Elastin	-0.15	0.270	-0.13	-1.61	0.64	-0.14	0.79	1.27
	Prolargin‡	0.39	**0.044***	0.12	0.27	0.79	0.08	0.28	3.64
Transverse	Col1	-0.32	0.083	-0.26	-0.70	0.50	-0.20	0.47	2.14
	Col2	-0.23	0.17	-0.15	-0.28	0.79	-0.08	0.21	4.75
	Col4	-0.02	0.46	0.15	0.22	0.83	0.06	0.14	7.05
	Col6	0.02	0.47	-0.10	-0.19	0.85	-0.06	0.23	4.35
	Col8	-0.39	**0.045***	-0.32	-0.75	0.47	-0.21	0.34	2.93
	Elastin	-0.02	0.47	-0.15	-0.47	0.65	-0.14	0.66	1.53
	Prolargin‡	0.01	0.49	0.26	-0.76	0.46	-0.21	0.56	1.79

*p <0.05 (bold)
†Identified as a significant predictor of toughness from a backward stepwise method (bold)
‡Prolargin quantity has a strong positive linear correlation with decorin and biglycan

6.3.4 Relationship between Collagen Crosslinks, Toughness, and Aging

Collagen crosslinks had significant correlations with toughness when using simple regression analysis, except for CML during longitudinal loading (Table 11,Figure 30). Multiple linear regression found strong collective significant effects between DPD, DHLNL, CML, and toughness for longitudinal loading ($p = 0.007$, $R^2_{adj} = 0.35$), and a very strong collective significant effect for transverse loading ($p < 0.001$, $R^2_{adj} = 0.62$). Notably, during transverse loading, DPD had a strong positive correlation with toughness (partial $r = 0.79$), and CML had a moderate negative correlation (partial $r = -0.68$). The backward stepwise method identified DPD and CML to be predictors of transverse toughness, and DPD to also be a predictor of longitudinal toughness (Figure 30). Aging had a significant interaction with the slope between DHLNL quantity and toughness, where older specimens had a more positive slope than young specimens.

Table 11:Relationship between collagen crosslink quantity and toughness during uniaxial pull-to-failure tests either parallel (longitudinal, samples size =17) or perpendicular (transverse, sample size = 17) to the circumferential fiber orientation.

Loading Orientation	Crosslink	Simiple Regression		Multiple Regression					
		r	*p*	*β*	*t*	*p*	Partial *r*	*Tol*	*VIF*
Longitudinal	DPD	0.63	**0.003***	0.36	1.52	**0.15†**	0.39	0.63	1.58
	DHLNL	-0.60	**0.005***	-0.49	-1.90	0.08	-0.47	0.54	1.86
	CML	0.02	0.46	0.18	0.79	0.44	0.22	0.71	1.42
Transverse	DPD	0.55	**0.006***	0.82	5.13	**<0.001*†**	0.79	0.75	1.34
	DHLNL	-0.39	**0.045***	0.31	1.38	0.19	0.33	0.38	2.62
	CML	-0.41	**0.036***	-0.87	-3.73	**0.002*†**	-0.68	0.36	2.82

*p <0.05 (bold)

†Identified as a significant predictor of tissue toughness from a backward stepwise method (bold)

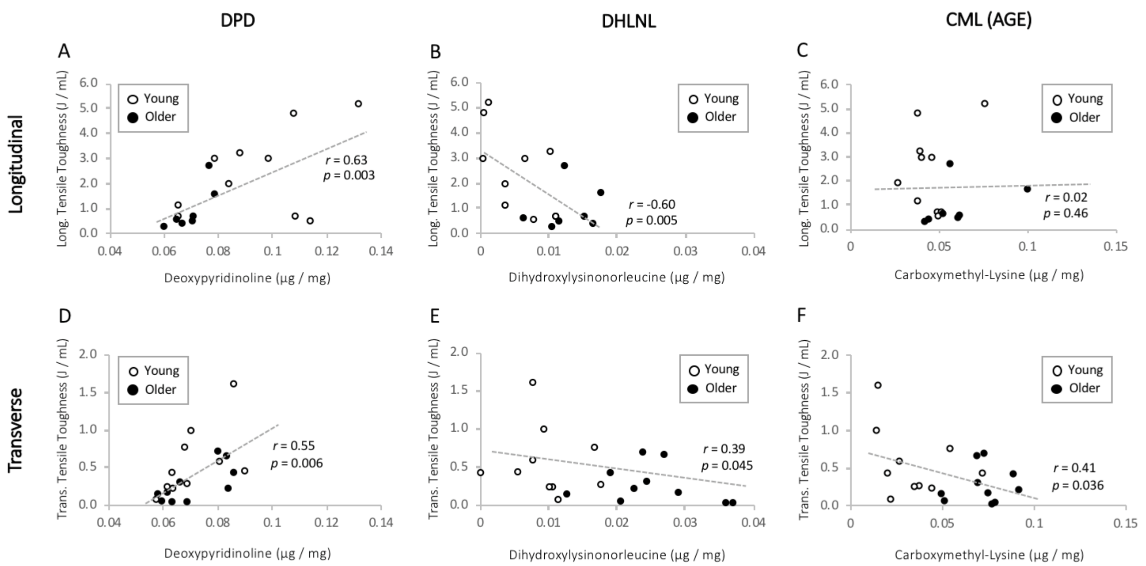

Figure 30: Correlations of collagen crosslink quantity and toughness using simple regression. (A-C) Under longitudinal loading, significant correlations existed between the quantity of enzymatic crosslinks DPD and DHLNL, but not the AGE crosslink CML. (D-F) Under transverse loading, all crosslinks had significant correlations with toughness. Multiple regression analysis found that DPD and CML had a synergistic effect, as transverse toughness was greatest with high quantities of DPD and low quantities of CML.

6.4. Discussion

In this study we investigated how aging alters the structural ECM molecules in healthy human meniscus, and whether these compositional changes are associated with reductions in tear resistance (toughness). We hypothesized that increases in AGE crosslinks (CML) would be strongly associated with a loss of toughness, and our findings supported this hypothesis when examining the toughness of the ground substance (transverse group), but our findings did not support this hypothesis when examining the toughness along the circumferential fibers (longitudinal group). The strongest predictors of overall tissue toughness, were the enzymatic collagen crosslinks (i.e., DPD), not the non-enzymatic AGE crosslinks.

We identified several interesting age-dependent changes in the quantity of structural ECM proteins (Table 9). The relative quantity of Col1 did not significantly change across age groups, which is consistent with prior findings that the amount of Col1 in meniscus is unaltered during healthy aging[80]. In contrast, degenerative meniscus exhibits a decrease in the quantity of Col1[186]. Degenerative meniscus also exhibits a decrease in Col2[186], but Col2 in our healthy older meniscus had a nearly 6-fold increase compared to the young group, and this structural shift of the meniscus towards the biochemical makeup of cartilage[149] could help increase or maintain swelling pressure of the tissue to withstand compressional forces[187,188]. Prolargin, biglycan, and decorin all decreased with aging, although decorin’s decrease was not significant (Figure 29). These decreases were weakly associated with loss of toughness in the ground substance (r = 0.39), but they had no effect on the fiber strength, which supported previous work investigating the mechanical role of decorin and the glycosaminoglycan crosslinks[83]. The loss of Col4 and Col6 indicate reduced interactions between matrix proteins[149] and chondrocytes[168], as well as a reduced capacity for cell signaling[167]. Similar to Col1, the quantity of elastin did not significantly change with aging, which is different than prior ligament and tendon studies that found elastin quantity to decrease with aging[189].

A surprising finding was that the observed changes in structural protein abundance only had weak to moderate correlations with tissue toughness under both longitudinal and transverse loading. In fact, the only protein that was predictive of tissue toughness using a multiple linear regression model was Col8 (Table 10). Col8 is a non-fibrillar short-chain collagen that may provide a porous, open matrix structure that can better withstand compressive forces[183]. Aging resulted in a significant 5-fold increase in Col8 (Figure 29), and this increase was associated with a loss of longitudinal tensile toughness (Table 10). It’s logical that Col8’s ability to enhance resistance to compressive loads by increasing pore size would have an adverse effect on the tissue’s capacity to withstand tensile forces. Overall, the lack of strong correlations between protein amount and toughness suggests that age-dependent weakening of the meniscus is not governed by changes in the quantity of structural ECM proteins, but rather changes in the quality of the structural proteins, such as structural damage or fibrillar disorganization[190,191].

The most significant predictor of tissue toughness that we identified was the quantity of collagen crosslinks in the tissue. We expected AGE crosslinks to negatively correlate with toughness, but this was only observed under transverse loading that tested the meniscal ground substance. AGE crosslinks may have a more pronounced effect on the ground substance by interfering with the interaction between collagen and other ECM proteins, as previously speculated[54], which may help explain the 70% reduction in transverse toughness that occurs with aging[91]. The endogenous AGE crosslinks may not have been abundant enough to cause the same increases in mechanical resilience under longitudinal loading observed in studies that artificially induced AGE crosslinks in rat tail tendon[54]. The correlations between AGE crosslinks and toughness are based on CML, and not PEN, since PEN had a low concentration in the meniscal tissue that was inconsistently detected in the proteomic profile. The higher concentration of CML relative to PEN follows a similar trend to previous research[184], and supports measuring CML in preference to PEN to study aging and oxidative stress in meniscus tissue[55,185].

The enzymatic crosslink DPD had the strongest positive correlation with toughness (Table 10). DPD helps provide tensile strength and stability in the collagen matrix[160,192], and assists with collagen folding in to a triple-helix along with hydroxylysine[193]. A reduction of DPD crosslinks, which we observed in older specimens (Table 9), corresponded to a loss of toughness in both the ground substance (transverse) and circumferential fibers (longitudinal, Figure 30). The increase of the immature crosslink DHLNL with age, which is a precursor to the mature DPD crosslink during tissue remodeling[160], could indicate a disruption of the hydroxyallysine pathway through which DPD crosslinks mature[194] and an impaired ability to repair molecular damage[82].

This study had several limitations. First, this study did not examine all possible collagen crosslinks, but rather examined four crosslinks that are abundant in soft tissue and have been speculated to have an effect on mechanical properties[15,55]. We weren’t able to detect the AGE crosslink PEN in most samples, and therefore PEN was not included in the multiple regression analysis. Second, we evaluated tissue adjacent to the mechanically tested tissue to most accurately compare biochemical and biomechanical changes (Figure 27), but we did not examine structural differences between different meniscal regions. Third, we only examined one mechanical property and a small group of collagenous and non-collagenous proteins. We were selective with the number of analyzed variables to avoid statistical problems with multiple comparisons, and therefore we selected well-recognized structural proteins and a mechanical property (toughness) that best captured resilience to meniscal tears. After testing the collinearity of the selected molecules we removed decorin and biglycan from the regression analysis because they showed a high positive correlation with prolargin for longitutinal and transverse tests. This helped reduce our variance inflation factors (VIF; Table 10), and the high positive correlation implied that regression results for prolargin were predictive of decorin and biglycan.

This is the first study to our knowledge to directly compare changes in human meniscal composition with changes in mechanical integrity. We found meniscal tissue loses toughness in tissue with less enzymatic collagen crosslink DPD and more non-fibrillar short-chain collagen Col8. We also found that the age-dependent increase in AGE crosslinks is associated with reductions in ground substance toughness. This knowledge helps advance our understanding of how age-dependent changes in tissue composition lead to a higher incidence of knee disorders in older populations.

6.5 Acknowledgements

Financial support kindly provided by the National Science Foundation under grant no. 1554353 (funded materials used in the experiment and personnel costs), the National Institute of General Medical Sciences under award numbers P20GM109095 and P20GM103408 (funded some of the equipment used in the experiment). We also acknowledge the University of Arkansas for Medical Sciences for providing the proteomic analysis under the IDeA National Resource for Quantitative Proteomics, and support from the Biomolecular Research Center at Boise State (RRID:SCR_019174) for the collagen crosslink analysis, with funding from the National Science Foundation under grant no. 0619793 and 0923535; the M. J. Murdock Charitable Trust, Lori and Duane Stueckle, and the Idaho State Board of Education.

CHAPTER 7: DISCUSSION

7.1 Summary

The overall objective of this research was to quantify the effect of age on the human meniscus. By mechanically testing tissue from young and older donors, we identified the differences in mechanical performance of the tissue due to age. By measuring the extracellular matrix proteins and crosslink molecules of this tissue, we help to identify some of the structural reasons for these mechanical changes due to age. By building a continuum damage mechanics model of the tissue, we provide the first step of using computational modelling to identify differences in failure loading of the tissue between young and aged populations. By creating and providing a tool to automate data analysis of soft tissue tensile tests, we reduce the burden of future research on the meniscus and similar tissues, while providing a standard for the calculation of previously poorly defined properties.

Key results of this work include:

- Tissue mechanical toughness was reduced with age, both along the primary circumferential fiber network, and perpendicular to it. This indicates a reduced energy absorption and dissipation capacity of the tissue with age.
- Rupture strain along the primary circumferential fiber network was reduced with age, reducing the total amount the tissue can elongate before being ripped apart.

- Failures of the tissue when loaded along the primary circumferential fiber network occurred at approximately 45°, following the plane of maximum shear stress.
- Failures of the tissue when loaded perpendicular to this fiber network occurred at a flat angle across the fibers, following the plane of maximum normal stress.
- Characterization of soft tissue failure strains with high speed digital image correlation matched to loading curves.
- Developed a free web application to automate the data analysis of soft tissue tensile tests.
- Implemented a robust method to identify the transition point on the stress-strain curve, and validated this method against a more computationally expensive finite element curve fit optimization schema.
- Found that continuum damage mechanics is capable of reproducing the failure behavior of meniscus tissue under tension.
- A piecewise strain energy function comprised of a transversely anisotropic fiber matrix embedded in a Veronda-Westmann hyperelastic ground substance matches the nonlinear tensile loading of meniscus tissue with high accuracy.
- Continuum damage mechanics using von Mises stress or maximum normal strain for damage criteria underpredicts strain in the failure region of meniscus tissue.

- Von Mises damage criteria is capable of reproducing the failure behavior in meniscus models loaded both along, and perpendicular to, the primary circumferential fiber axis.
- Model predicted strains in the tissue were more spread out then the highly concentrated strains measured experimentally. This resulted in models loading the tissue perpendicular to the primary circumferential fibers to be unable to run to completion in most instances.
- This strain concentration discrepancy also contraindicates the use of regularization methods when using continuum damage mechanics, as these methods further spread strain out.
- Advanced glycation end-products significantly increase in meniscus tissue with age.
- There were several significant changes to Collagen due to age. Notable changes include an increase of Collagen II and Collagen VIII, as well as a decrease in Collagen VI.
- The amounts of elastin Collagen I did not significantly change due to age. These are proteins most commonly associated with extensibility in the tissue.
- An increase of proteins associated with osteoarthritis were seen with age.
- Carboxymethyl-lysine, an advanced glycation end-product, was measured in much greater concentration than the other advanced glycation end-product measured in this study, Pentosidine. This work recommends

measuring Carboxymethyl-lysine in preference to Pentosidine as a method to quantify oxidative stress.

- An increase of the collagen crosslink molecule Dihydroxylysinonorleucine correlated significantly with a loss of tissue strength and modulus.
- An increase of the advanced glycation end-product Carboxymethyl-lysine correlated significantly with a loss of tissue strength and toughness.

We believe that these findings represent a significant contribution to the understanding of how the meniscus changes with age, and becomes more susceptible to injury.

7.2 Clinical Relevance

The findings of this work have both a direct and indirect effect on the treatment of meniscus tears. The mechanical characterization work indirectly benefits clinicians, in that it informs modeling of the tissue, as well as differences in the strength and toughness of the tissue with age. This information is critical to understanding the tear mechanics that will be used to inform more directly relevant analyses of the tissue. The automated analysis of soft tissue tensile properties also indirectly benefits clinicians in that it will assist further research of both meniscus and other soft tissues. Encouraging further characterization of a wide variety of tissues increases our understanding of soft tissues as a whole, as well as providing a larger data set to tissues previously analyzed.

The computational modeling outlined in this work can be directly used to assess the differences in the amount of load that can be sustained prior to the onset of irreversible damage between young and older patients. This can inform the limits of what may be considered healthy activities for aging populations. This model may also be implemented in to whole knee models to analyze different loadings of the whole knee joint, which can have a wide variety of potential benefits to clinicians assessing knee stresses, designing knee braces, or evaluating the effect of surgical interventions. As this was the first model of human meniscus, more refined modeling techniques may come in the future. This model would inform these potential future models and give them something to compare to, potentially indirectly benefitting the further understanding of meniscus tears.

The structure-function work has the greatest amount of directly applicable information to clinicians. Understanding how the structural makeup of the meniscus is changing with age gives direct insight to the changing structure with age. The large changes to the collagen makeup being the most directly profound of these, telling us that the meniscus may be beginning to behave more like articular cartilage with age. Understanding this changing behavior may help clinicians understand the changes to tear incidence, and inform patient care both pre and post injury. The structure work also indirectly benefits the treatment of the meniscus by identifying proteins of interest for targeted analysis. These analyses will prove or disprove the mechanical effect of the loss or gain of certain proteins, and open the door for potential therapeutic treatments, much like hyaluronic acid injections have been used to combat cartilage degeneration.[195] Understanding the consequences of the accumulation of advanced glycation end-products also represents a directly relevant finding, as this work suggests that preventing the accumulation of these molecules could help sustain the meniscus' energy dissipation capacity, increasing the longevity of the tissue in older populations. Understanding the accumulation of these molecules, and how they interact with the maturation of normal collagen crosslink molecules, gives clinicians insight to the potential causes of disfunction in the tissue remodeling with age.

7.3 Publications

7.3.1 Peer Reviewed Journal Articles

1. Nesbitt, D. Q., Siegel, D. N., Nelson, S. J., and Lujan, T. J. "*Effect of Age on the Failure Properties of Human Meniscus: High-Speed Strain Mapping of Tissue Tears*," Journal of Biomechanics Vol 115 pp 110-126, 2021.[91] **Half of the data of this work was done during my MS degree.**
2. Nesbitt DQ, Nelson ML, Shannon KS, Lujan TJ. "*Dots-on-Plots: A Web Application to Analyze Stress-Strain Curves from Tensile Tests of Soft Tissue.*" Journal of Biomechanical Engineering 2023 Feb 1;145(2):024504.[133]
3. Nesbitt DQ, Burruel, DE, Henderson, BS, Lujan TJ. "*Finite Element Modeling of Meniscal Tears Using Continuum Damage Mechanics and Digital Image Correlation*." Scientific Reports 2023 March 10; 13(1).[196]
4. Nesbitt DQ, Pu X, Turner M, Zavala A, Bond L, Oxford J, Lujan TJ. *"Age-Dependent Changes in Collagen Crosslinks Weaken the Mechanical Toughness of Human Mensicus."* Submitted to the Journal of Orthopaedic Research on July 22nd 2023.

7.3.2 Abstracts

1. Nesbitt DQ, Krentz ME, Lujan TJ, "*The Effect of Fiber Orientation on Failure Patterns in the Bovine Meniscus During Tensile Loading."* Summer Biomechanics, Bioengineering and Biotransport Conference, June 21 – 24 2017, Tucson, AZ, USA. **Poster Presentation**

2. Nesbitt DQ, Krentz ME, Lujan TJ, "*High-speed Strain Mapping of Human Meniscus During Tensile Loading."* 8th World Congress of Biomechanics, Dublin, Ireland, July 2018. **Poster Presentation**
3. Nesbitt DQ, Siegel DN, Nelson SJ, Lujan TJ, "*How Age Affects the Failure Properties of Human Meniscus: High-Speed Strain Mapping of Tears."* Summer Biomechanics, Bioengineering and Biotransport Conference, June 17 – 20 2020, Virtual. **Podium Presentation**
4. Nesbitt DQ, Lujan TJ, "*Damage Modeling of Human Meniscus with Digital Image Correlation."* Boise State Graduate Student Showcase. 2021. **Poster Presentation.**
5. Nesbitt DQ, Turner M, Pu X, Bond L, Woods K, Oxford J, Lujan TJ, "*Age-Dependent Changes to Collagen Crosslinks Reduce the Toughness of Human Meniscus."* Orthopaedic Research Society, February 4-8, 2022. Tampa, Florida. **Poster Presentation.**
6. Nesbitt DQ, Burruel DE, Lujan TJ. "*Using Digital Image Correlation to Validate a Finite Element Damage Model of Human Meniscus."* 15th World Congress on Computational Mechanics. July 31- August 5 2022. Virtual. **Podium Presentation.**

7.4 Limitations

These studies had limitations. Most notably, was that all mechanical and biochemical characterization was done on a total of 10 donors. While this sample size was sufficient for many of the comparisons done, the potential for type 2 error could have been reduced for data points with lower effect size using a greater sample set. All of these studies exclusively evaluated human meniscus tissue, so any and all conclusions would be relevant to only human meniscus tissue. The evaluation of the changes to meniscus structure with age also focused solely on structural proteins of the extracellular matrix. It is possible that other highly impactful comparisons of other measured proteins could be performed with this data. While we do not intend to investigate these possibilities ourselves, it is our intent to make the proteomics data widely available to the scientific community. Another limitation, is that the computational model used to validate both the Dots-on-Plots application and to build the continuum damage mechanics model, only compared a single constitutive model. While the evaluation of other models could be beneficial, we feel that the high accuracy ($R > 0.97$) of this selected formulation was sufficient for the studies performed here. Lastly, the effect of age was not considered in the modeling work we performed. Our intent was to validate a model that could accurately recreate tissue at any age, but the difference in average model parameters for young and older specimens were not compared.

7.5 Future work

Future work should expand upon the modeling work of Chapter 5 by implementing the continuum damage mechanics framework in to models of the whole meniscus. Applying physiological loading at this scale of model would then asses the ability of the model framework to simulate tears as they would happen within the knee, and would open the door to increasingly complex models that could determine the injury risk posed by different motions. Models simulating tears of the whole meniscus would need validation against experimental observations, which could be obtained by performing loading to failure on whole tissue using machines that simulate joint movement, such as the Vivo six degree of freedom joint simulator[197]. While this model formulation is sufficient for quasi-static loading, impact loading introduces the time rate dependent nature of hydrated soft tissues[198], and viscoelastic effects would need to be considered. Previous mathematical models of meniscus fatigue loading were also improved by the inclusion of viscoelasticity[199], so model formulations designed to account for repeated loading over time would likewise benefit from including viscoelasticity.

Our structural work detailed in Chapter 6 identified several proteins and molecules that may be responsible for the changing of meniscus mechanical characteristics with aging, but the correlations done in this work are not causative. Studies will need to be designed to target these specific proteins and molecules in order to prove their effect on mechanical characteristics. This could be achieved via animal knockout or over expression models, as well as chemical applications that induce the formation of advanced glycation end-products. Once these structure-function relationships have been proven, it will increase our understanding of how the meniscus changes with age, and open the door to potential tissue diagnostics using biopsied tissue.

This work should also expand to include tears of the meniscus root, where the main body of the meniscus tissue transitions in to the ligaments that attach to the surrounding bones.[200] Many tears of the meniscus are in the root region, so understanding the tear mechanisms of this complex region represents an important goal in reducing meniscus tear incidence. Other research groups have done some mechanical characterization of this region,[201–203] but to our knowledge no study has yet computationally modeled or biochemically analyzed this region. The work outlined in this dissertation could serve as a guide to characterizing the changing of tear incidence of the meniscus roots with age.

In conclusion, the continued refinement of meniscus models will aid in the understanding of the mechanisms that lead to injury, as well as lead to innovations in clinical treatment and prevention of these injuries. Additionally, targeted investigations in to the changing structure-function relationships of meniscus with aging will help with the understanding of the cause of increasing of risk with age, and open the door to potential therapies to combat these causes.

REFERENCES

1. Kim S, Bosque J, Meehan JP, et al. 2011. Increase in Outpatient Knee Arthroscopy in the United States: A Comparison of National Surveys of Ambulatory Surgery, 1996 and 2006. J Bone Joint Surg Am 93(11):994–1000.
2. Demange MK, Gobbi RG, Camanho GL. 2016. “Fatigue meniscal tears”: a description of the lesion and the results of arthroscopic partial meniscectomy. Int Orthop 40(2):399–405.
3. CDC. 2020. Osteoarthritis (OA). Centers for Disease Control and Prevention Available from: https://www.cdc.gov/arthritis/basics/osteoarthritis.htm.
4. Losina E, Weinstein AM, Reichmann WM, et al. 2013. Lifetime risk and age of diagnosis of symptomatic knee osteoarthritis in the US. Arthritis Care Research 65(5) Available from: https://www.ncbi.nlm.nih.gov/pmc/articles/PMC3624763/pdf/nihms412728.pdf.
5. Petersen W, Tillmann B. 1995. Age-related blood and lymph supply of the knee menisci:a cadaver study. Acta Orthop 66(4):308–312.
6. Peloquin JM, Santare MH, Elliott DM. 2016. Advances in Quantification of Meniscus Tensile Mechanics Including Nonlinearity, Yield, and Failure. J Biomech Eng 138(2):021002 Available from: http://biomechanical.asmedigitalcollection.asme.org/article.aspx?doi=10.1115/1.4032354.

7. Tissakht M, Ahmed AM. 1995. Tensile stress-strain characteristics of the human meniscal material. J Biomech 28(4):411–422.

8. Haut Donahue TL, Hull ML, Rashid MM, Jacobs CR. 2003. How the stiffness of meniscal attachments and meniscal material properties affect tibio-femoral contact pressure computed using a validated finite element model of the human knee joint. J Biomech 36(1):19–34.

9. Martin C, Sun W, Elefteriades J. 2015. Patient-specific finite element analysis of ascending aorta aneurysms. Am J Physiol Heart Circ Physiol 308(10):H1306–H1316.

10. Cheruvu B. 2015. Anterior Cruciate Ligament Biomechanics, Computational Modeling of Mechanical Behavior and Injury Risk. Available from: https://corescholar.libraries.wright.edu/etd_allhttps://corescholar.libraries.wright.edu/etd_all/1308.

11. McGregor C, Zobeiry N, Vaziri R, et al. 2017. Calibration and validation of a continuum damage mechanics model in aid of axial crush simulation of braided composite tubes. Compos Part A Appl Sci Manuf 95:208–219 Available from: http://dx.doi.org/10.1016/j.compositesa.2017.01.012.

12. Danso EK, Honkanen JTJ, Saarakkala S, Korhonen RK. 2014. Comparison of nonlinear mechanical properties of bovine articular cartilage and meniscus. J Biomech 47(1):200–206 [cited 2017 Sep 24] Available from: http://linkinghub.elsevier.com/retrieve/pii/S0021929013004387.

13. Wale ME, Nesbitt DQ, Henderson BS, et al. 2020. Applying ASTM Standards to Tensile Tests of Musculoskeletal Soft Tissue: Methods to Reduce Grip Failures and Promote Reproducibility. J Biomech Eng .

14. Abdelgaied A, Stanley M, Galfe M, et al. 2015. Comparison of the biomechanical tensile and compressive properties of decellularised and natural porcine meniscus. J Biomech 48(8):1389–1396 Available from: http://dx.doi.org/10.1016/j.jbiomech.2015.02.044.

15. Tsujii A, Nakamura N, Horibe S. 2017. Age-related changes in the knee meniscus. Knee 24(6):1262–1270 Available from: https://doi.org/10.1016/j.knee.2017.08.001.

16. Petersen W, Tillmann B. 1995. Age-related blood and lymph supply of the knee menisci:a cadaver study. Acta Orthop 66(4):308–312.

17. Mow VC, Huiskes R, Stokes IA IJC. 2004. Basic Orthopaedic Biomechanics and Mechano-Biology, 3rd ed. Lippincott Williams and Wilkins. 543–561 p.

18. Metcalf MH, Barrett GR. 2004. Prospective Evaluation of 1485 Meniscal Tear Patterns in Patients with Stable Knees. American Journal of Sports Medicine 32(3):675–680.

19. Jones JC, Burks R, Owens BD, et al. 2012. Incidence and risk factors associated with meniscal injuries among active-duty US Military service members. J Athl Train 47(1):67–73.

20. Snoeker BAM, Bakker EWP, Kegel CAT, Lucas C. 2013. Risk factors for meniscal tears: A systematic review including meta-analysis. Journal of Orthopaedic and Sports Physical Therapy 43(6):352–367.

21. Henry S, Mascarenhas R, Kowalchuk D, et al. 2012. Medial meniscus tear morphology and chondral degeneration of the knee: Is there a relationship? Arthroscopy - Journal of Arthroscopic and Related Surgery 28(8):1124–1134.

22. Goertzen DJ, Budney DR, Cinats JG. 1997. Methodology and apparatus to determine material properties of the knee joint meniscus. Med Eng Phys 19(5):412–419.

23. Fithian DC, Kelly M a, Mow VC. 1990. Material properties and structure-function relationships in the menisci. Clin Orthop Relat Res :19–31.

24. Bullough PG, Munuera L, Murphy J, Weinstein AM. 1970. the Strength of the Menisci of the Knee As It Relates To Their Fine Structure. J Bone Joint Surg Br 52-B(3):564–570.

25. Fischenich KM, Lewis J, Kindsfater KA, et al. 2015. Effects of degeneration on the compressive and tensile properties of human meniscus. J Biomech 48(8):1407–1411 Available from: http://dx.doi.org/10.1016/j.jbiomech.2015.02.042.

26. Lechner K, Hull ML, Howell SM. 2000. Is the circumferential tensile modulus within a human medial meniscus affected by the test sample location and cross-sectional area? Journal of Orthopaedic Research 18(6):945–951.

27. Tanaka ML, Vest N, Ferguson CM, Gatenholm P. 2014. Comparison of biomechanical properties of native menisci and bacterial cellulose implant. International Journal of Polymeric Materials and Polymeric Biomaterials 63(17):891–897.

28. Bursac P, York A, Kuznia P, et al. 2009. Influence of Donor Age on the Biomechanical and Biochemical Properties of Human Meniscal Allografts. Am J Sports Med 37(5):884–889.

29. Temple MM, Bae WC, Chen MQ, et al. 2007. Age- and site-associated biomechanical weakening of human articular cartilage of the femoral condyle. Osteoarthritis Cartilage 15(9):1042–1052.

30. Ferguson SJ, Steffen T. 2003. Biomechanics of the aging spine. European Spine Journal 12(SUPPL. 2):97–103.

31. Vogel HG. 1978. Influence of Maturation and Age on Mechanical and Biochemical Parameters of Connective Tissue of Various Organs in the Rat. Connect Tissue Res 6:161–166.

32. Pardes A, Beach Z, Raja H, et al. 2017. Aging leads to inferior achilles tendon mechanics and altered ankle function in rodents. J Biomech (60):30–38.

33. Swank KR, Behn AW, Dragoo JL. 2015. The Effect of Donor Age on Structural and Mechanical Properties of Allograft Tendons. Am J Sports Med 43(2):453–459.

34. Noyes FR, Grood ES. 1976. The strength of the anterior cruciate ligament in humans and rhesus monkeys: Age related and species related changes. Journal of Bone and Joint Surgery - Series A 58(8):1074–1082.

35. Volokh KY. 2008. Prediction of arterial failure based on a microstructural bi-layer fiber-matrix model with softening. J Biomech 41(2):447–453.

36. Song Y, Debski RE, Musahl V, et al. 2004. A three-dimensional finite element model of the human anterior cruciate ligament: A computational analysis with experimental validation. J Biomech 37(3):383–390.

37. Kedgley AE, Saw TH, Segal NA, et al. 2019. Predicting meniscal tear stability across knee-joint flexion using finite-element analysis. Knee Surgery, Sports Traumatology, Arthroscopy 27(1):206–214 Available from: http://dx.doi.org/10.1007/s00167-018-5090-4.

38. Meakin JR, Shrive NG, Frank CB, Hart DA. 2003. Finite element analysis of the meniscus: The influence of geometry and material properties on its behaviour. Knee 10(1):33–41.

39. Aspden RM. 1985. A model for the function and failure of the meniscus. Eng Med 14(3):119–122.

40. Peña E, Peña JA, Doblaré M. 2009. On the Mullins effect and hysteresis of fibered biological materials: A comparison between continuous and discontinuous damage models. Int J Solids Struct 46(7–8):1727–1735.

41. Ehret AE, Itskov M. 2009. Modeling of anisotropic softening phenomena: Application to soft biological tissues. Int J Plast 25(5):901–919.

42. Alastrué V, Rodríguez JF, Calvo B, Doblaré M. 2007. Structural damage models for fibrous biological soft tissues. Int J Solids Struct 44(18–19):5894–5911.

43. Liao H, Belkoff S. 1999. A failure model for ligaments. J Biomech 32:183–188.

44. Natali AN, Pavan PG, Carniel EL, et al. 2005. Anisotropic elasto-damage constitutive model for the biomechanical analysis of tendons. Med Eng Phys 27(3):209–214.

45. Martins P, Peña E, Jorge NRM, et al. 2012. Mechanical characterization and constitutive modelling of the damage process in rectus sheath. J Mech Behav

Biomed Mater 8:111–122 Available from: http://dx.doi.org/10.1016/j.jmbbm.2011.12.005.

46. Budynas RG, Nisbett JK. 2015. Shigley's Mechanical Engineering Design. 1105 p.

47. Tiossi R, Vasco MAA, Lin L, et al. 2013. Validation of finite element models for strain analysis of implant-supported prostheses using digital image correlation. Dental Materials 29(7):788–796 Available from: http://dx.doi.org/10.1016/j.dental.2013.04.010.

48. Sebastian CM. 2011. a Method for the Validation of Computational Models Using Digital Image Correlation and Image Decomposition.

49. Martin JA, Buckwalter JA. 2001. Roles of articular cartilage aging and chondrocyte senescence in the pathogenesis of osteoarthritis. Iowa Orthop J 21(319):1–7.

50. Kannus P, Paavola M, Jozsa L. 2005. Aging and Degeneration of Tendons. Tendon Injuries :25–31.

51. Loeser RF. 2004. Aging cartilage and osteoarthritis--what's the link? Science of aging knowledge environment 2004(29).

52. Martin C, Pham T, Sun W. 2011. Significant differences in the material properties between aged human and porcine aortic tissues. European Journal of Cardio-thoracic Surgery 40(1):28–34.

53. Avery NC, Bailey AJ. 2006. The effects of the Maillard reaction on the physical properties and cell interactions of collagen. Pathologie Biologie 54(7):387–395.

54. Snedeker JG, Gautieri A. 2014. The role of collagen crosslinks in ageing and diabetes - The good, the bad, and the ugly. Muscles Ligaments Tendons J 4(3):303–308.

55. Takahashi M, Suzuki M, Kushida K, et al. 1998. The effect of aging and osteoarthritis on the mature and senescent cross-links of collagen in human meniscus. Arthroscopy 14(4):366–72 Available from: http://www.ncbi.nlm.nih.gov/pubmed/9620647.

56. Verzijl N, DeGroot J, Zaken C Ben, et al. 2002. Crosslinking by advanced glycation end products increases the stiffness of the collagen network in human articular cartilage: A possible mechanism through which age is a risk factor for osteoarthritis. Arthritis Rheum 46(1):114–123.

57. Chen AC, Temple MM, Ng DM, et al. 2002. Induction of advanced glycation end products and alterations of the tensile properties of articular cartilage. Arthritis Rheum 46(12):3212–3217.

58. DeGroot J, Verzijl N, Wenting-Van Wijk MJG, et al. 2004. Accumulation of Advanced Glycation End Products as a Molecular Mechanism for Aging as a Risk Factor in Osteoarthritis. Arthritis Rheum 50(4):1207–1215.

59. Lake SP, Miller KS, Elliott DM, Soslowsky LJ. 2009. Effect of fiber distribution and realignment on the nonlinear and inhomogeneous mechanical properties of human supraspinatus tendon under longitudinal tensile loading. Journal of Orthopaedic Research 27(12):1596–1602.

60. Ristaniemi A, Stenroth L, Mikkonen S, Korhonen RK. 2018. Comparison of elastic, viscoelastic and failure tensile material properties of knee ligaments and

patellar tendon. J Biomech 79:31–38 Available from: https://doi.org/10.1016/j.jbiomech.2018.07.031.

61. Hutchinson ID, Moran CJ, Potter HG, et al. 2014. Restoration of the meniscus: Form and function. American Journal of Sports Medicine 42(4):987–998.

62. Makris EA, Hadidi P, Athanasiou KA. 2011. The knee meniscus: Structure-function, pathophysiology, current repair techniques, and prospects for regeneration. Biomaterials 32(30):7411–7431.

63. Nielsen AB, Yde J. 1991. Epidemiology of Acute Knee Injuries: A Prospective Hospital Investigation. J Trauma 31(12):1644–1648.

64. Fox AJS, Bedi A, Rodeo SA. 2012. The Basic Science of Human Knee Menisci. Sports Health: A Multidisciplinary Approach 4(4):340–351 Available from: http://journals.sagepub.com/doi/10.1177/1941738111429419.

65. Peloquin JM, Santare MH, Elliott DM. 2018. Short cracks in knee meniscus tissue cause strain concentrations, but do not reduce ultimate stress, in single-cycle uniaxial tension. R Soc Open Sci 5(11).

66. Qu RT, Zhang ZJ, Zhang P, et al. 2016. Generalized energy failure criterion. Sci Rep 6(3):1–8.

67. Barsanescu PD, Comanici AM. 2017. von Mises hypothesis revised. Acta Mech 228(2):433–446.

68. Kulkarni V V., Chand K. 1975. Pathological anatomy of the aging meniscus. Acta Orthop 46(1):135–140.

69. Creechley JJ, Krentz ME, Lujan TJ. 2017. Fatigue life of bovine meniscus under longitudinal and transverse tensile loading. J Mech Behav Biomed Mater

69(December 2016):185–192 Available from: http://dx.doi.org/10.1016/j.jmbbm.2016.12.020.

70. Nelson SJ, Creechley JJ, Wale ME, Lujan TJ. 2020. Print-A-Punch: A 3D printed device to cut dumbbell-shaped specimens from soft tissue for tensile testing. J Biomech 112.

71. Morrill EE, Tulepbergenov AN, Stender CJ, et al. 2016. A validated software application to measure fiber organization in soft tissue. Biomech Model Mechanobiol 15(6):1467–1478.

72. Liu XY, Li RL, Zhao HW, et al. 2015. Quality assessment of speckle patterns for digital image correlation by Shannon entropy. Optik (Stuttg) 126(23):4206–4211 Available from: http://dx.doi.org/10.1016/j.ijleo.2015.08.034.

73. Stender CJ, Rust E, Martin PT, et al. 2018. Modeling the effect of collagen fibril alignment on ligament mechanical behavior. Biomech Model Mechanobiol 17(2):543–557 Available from: https://doi.org/10.1007/s10237-017-0977-4.

74. Blaber J, Adair B, Antoniou A. 2015. Ncorr: Open-Source 2D Digital Image Correlation Matlab Software. Exp Mech 55(6):1105–1122.

75. Nakagawa S, Cuthill IC. 2007. Effect size, confidence interval and statistical significance: A practical guide for biologists. Biological Reviews 82(4):591–605.

76. Li Y, Fessel G, Georgiadis M, Snedeker JG. 2013. Advanced glycation end-products diminish tendon collagen fiber sliding. Matrix Biology 32(3–4):169–177 Available from: http://dx.doi.org/10.1016/j.matbio.2013.01.003.

77. Hashin Z. 1980. Failure Criteria for Unidirectional Fiber Composites. J Appl Mech 47(June):329–334.

78. Mullin J, Berry JM, Gatti A. 1968. Some Fundemental Fracure Mechanisms Applicable to Advanced Filament Reinforced Composites. J Compos Mater 2(1):82–103.

79. Rosen WB. 1964. Tensile Failure of Fibrous Composites. American Institute of Aeronautics and Astronautics 2(11):1985–1991.

80. Peters TJ, Smillie IS, Peters TJ, Smillie IS. 1971. Studies on Chemical Composition of Menisci from the Human Knee-Joint [Abridged]. J R Soc Med 64(3):261–262.

81. Kempson GE. 1982. Relationship between the tensile properties of articular cartilage from the human knee and age. Ann Rheum Dis 41(5):508–511.

82. Zitnay JL, Li Y, Qin Z, et al. 2017. Molecular level detection and localization of mechanical damage in collagen enabled by collagen hybridizing peptides. Nat Commun 8:1–12 Available from: http://dx.doi.org/10.1038/ncomms14913.

83. Lujan TJ, Underwood CJ, Henninger HB, et al. 2007. Effect of Dermatan Sulfate Glycosaminoglycans on the Quasi-Static Material Properties of the Human Medial Collateral Ligament.11:1–10.

84. Krentz ME. 2018. High-Cycle Fatigue Life of Human Meniscus. Masters Thesis .

85. Hansen KA, Weiss JA, Barton JK. 2002. Recruitment of tendon crimp with applied tensile strain. J Biomech Eng 124(1):72–77.

86. ASTM. 1997. American Society for Testing and Materials. Standard Test Method for Tensile Properties of Polymer Matrix Composite Materials (D3039/D 3039M). ASTM :105–116.

87. ASTM. 2003. American Society for Testing and Materials. Standard test method for tensile properties of plastics (D 638 - 02a). ASTM 08:46–58 Available from: http://scholar.google.com/scholar?hl=en&btnG=Search&q=intitle:Standard+Test+Method+for+Tensile+Properties+of+Plastics#0.

88. Illinois Tool Works Inc. 2021. Materials Testing Software. Instron.com [cited 2022 Aug 19] Available from: https://www.instron.com/en-us/products/materials-testing-software/bluehill-fracture.

89. AMETEK. 2021. ForceTest Force Measuring Software. Available from: https://www.ametektest.com/products/software/nexygenplus-materials-testing-software.

90. Vidik A, Danielson C, Oxlund H. 1982. On fundemental and phenomenological models, structure and mechanical properties of collagen, elastin and glycosaminoglycan complexes. Biorheology 19(3):437–451.

91. Nesbitt DQ, Siegel DN, Nelson SJ, Lujan TJ. 2021. Effect of age on the failure properties of human meniscus: High-speed strain mapping of tissue tears. J Biomech 115:110126 Available from: https://doi.org/10.1016/j.jbiomech.2020.110126.

92. Tanaka ML, Weisenbach CA, Carl Miller M, Kuxhaus L. 2011. A continuous method to compute model parameters for soft biological materials. J Biomech Eng 133(7).

93. He Y, Chen Y, Wan X, et al. 2020. Preparation and Characterization of an Optimized Meniscal Extracellular Matrix Scaffold for Meniscus Transplantation. Front Bioeng Biotechnol 8(July):1–12.

94. Nasser M. Abbasi. 2006. On stress measures in deformed solids.:1–45 [cited 2022 Apr 11] Available from: https://www.12000.org/my_notes/stress_measures/index.htm#x1-60001.4.

95. Maas SA, Ellis BJ, Ateshian GA, Weiss JA. 2012. FEBio: Finite elements for biomechanics. J Biomech Eng 134(1):1–10.

96. Weiss JA, Gardiner JC, Bonifasi-Lista C. 2002. Ligament material behavior is nonlinear, viscoelastic and rate-independent under shear loading. J Biomech 35:943–950.

97. Marquardt DW. 1963. An Algorithm for Least-Squares Estimation of Nonlinear Parameters. Journal of the Society for Industrial and Applied Mathematics 11(2):431–441.

98. Satopää V, Albrecht J, Irwin D, Raghavan B. 2011. Finding a “kneedle” in a haystack: Detecting knee points in system behavior. In: Proceedings - International Conference on Distributed Computing Systems. p 166–171.

99. Everingham JB, Martin PT, Lujan TJ. 2019. A hand-held device to apply instrument-assisted soft tissue mobilization at targeted compression forces and stroke frequencies. Journal of Medical Devices, Transactions of the ASME 13(1).

100. Thermo-Calc. 2021. Thermo-Calc Software. [cited 2022 Aug 19] Available from: https://thermocalc.com/products/databases/.

101. SenteSoftware. 2021. JMatPro. Available from: https://www.sentesoftware.co.uk/jmatpro.

102. Kahl M, Schneidereit D, Bock N, et al. 2021. MechAnalyze: An Algorithm for Standardization and Automation of Compression Test Analysis. Tissue Eng Part C Methods 27(10):529–542.

103. Lim A, Protsenko DE, Wong BJF. 2011. Changes in the tangent modulus of rabbit septal and auricular cartilage following electromechanical reshaping. J Biomech Eng 133(9).

104. Callister WD, Rethwisch DG. 2012. Materials Science and Engineering- An Introduction, 9th ed. John Wiley and Sons, Incorporated. 169–216 p.

105. Unal M, Akkus O. 2015. Raman spectral classification of mineral- and collagen-bound water's associations to elastic and post-yield mechanical properties of cortical bone. Bone 81:315–326.

106. Axpe E, Orive G, Franze K, Appel EA. 2020. Towards brain-tissue-like biomaterials. Nat Commun 11(1).

107. Launey ME, Ritchie RO. 2009. On the fracture toughness of advanced materials. Advanced Materials 21(20):2103–2110.

108. Rothermel TM, Win Z, Alford PW. 2020. Large-deformation strain energy density function for vascular smooth muscle cells. J Biomech 111.

109. Nims R, Durney KM, Cigan AD, et al. 2016. Continuum theory of fibrous tissue damage mechanics using bond kinetics: Application to cartilage tissue engineering. Interface Focus 6(1).

110. Li K, Zhang S jie, Du C fei, et al. 2020. Effect of Strain Rates on Failure of Mechanical Properties of Lumbar Intervertebral Disc Under Flexion. Orthop Surg 12(6):1980–1989.

111. Zhang G, Luo J, Zheng G, et al. 2021. Is the 0.2%-Strain-Offset Approach Appropriate for Calculating the Yield Stress of Cortical Bone? Ann Biomed Eng 49(7):1747–1760.

112. Lohmander LS, Englund PM, Dahl LL, Roos EM. 2007. The long-term consequence of anterior cruciate ligament and meniscus injuries: Osteoarthritis. American Journal of Sports Medicine 35(10):1756–1769.

113. Feeley BT, Liu S, Garner AM, et al. 2016. The cost-effectiveness of meniscal repair versus partial meniscectomy: A model-based projection for the United States. Knee 23(4):674–680.

114. Han SB, Shetty GM, Lee DH, et al. 2010. Unfavorable results of partial meniscectomy for complete posterior medial meniscus root tear with early osteoarthritis: A 5- to 8-year follow-up study. Arthroscopy - Journal of Arthroscopic and Related Surgery 26(10):1326–1332.

115. Park HS, Ahn C, Fung DT, et al. 2010. A knee-specific finite element analysis of the human anterior cruciate ligament impingement against the femoral intercondylar notch. J Biomech 43(10):2039–2042.

116. Lujan TJ, Dalton MS, Thompson BM, et al. 2007. Effect of ACL deficiency on MCL strains and joint kinematics. J Biomech Eng 129(3):386–392.

117. Ellis BJ, Lujan TJ, Dalton MS, Weiss JA. 2006. Medial collateral ligament insertion site and contact forces in the ACL-deficient knee. Journal of Orthopaedic Research 24(4):800–810.

118. Tvergaard V. 1989. Material Failure by Void Growth to Coalescence. In: Advances in Applied Mechanics. p 83–151.

119. Calvo B, Peña E, Martins P, et al. 2009. On modelling damage process in vaginal tissue. J Biomech 42(5):642–651.

120. Volokh KY. 2011. Modeling failure of soft anisotropic materials with application to arteries. J Mech Behav Biomed Mater 4(8):1582–1594 Available from: http://dx.doi.org/10.1016/j.jmbbm.2011.01.002.

121. Anderson AE, Ellis BJ, Weiss JA. 2007. Verification, validation and sensitivity studies in computational biomechanics. Comput Methods Biomech Biomed Engin 10(3):171–184.

122. Dahan G, Safran O, Yosibash Z. 2022. Can neck fractures in proximal humeri be predicted by CT-based FEA? J Biomech 136:111039.

123. Belda R, Palomar M, Peris-Serra JL, et al. 2020. Compression failure characterization of cancellous bone combining experimental testing, digital image correlation and finite element modeling. Int J Mech Sci 165.

124. Grassi L, Väänänen SP, Amin Yavari S, et al. 2013. Experimental validation of finite element model for proximal composite femur using optical measurements. J Mech Behav Biomed Mater 21:86–94.

125. Gothivarekar S, Coppieters S, van de Velde A, Debruyne D. 2020. Advanced FE model validation of cold-forming process using DIC: Air bending of high strength steel. International Journal of Material Forming 13(3):409–421.

126. Chuang SF, Chang CH, Chen TYF. 2011. Contraction behaviors of dental composite restorations - Finite element investigation with DIC validation. J Mech Behav Biomed Mater 4(8):2138–2149.

127. Sutradhar A, Park J, Carrau D, Miller MJ. 2014. Experimental validation of 3D printed patient-specific implants using digital image correlation and finite element analysis. Comput Biol Med 52:8–17.

128. von Forell GA, Bowden AE. 2014. A damage model for the percutaneous triple hemisection technique for tendo-achilles lengthening. J Biomech 47(13):3354–3360.

129. Weiss JA, Maker BN, Govindjee S. 1996. Finite element implementation of incompressible, transversely isotropic hyperelasticity. Comput Methods Appl Mech Eng 135(1–2):107–128 Available from: http://linkinghub.elsevier.com/retrieve/pii/0045782596010353.

130. Henninger HB, Ellis BJ, Scott SA, Weiss JA. 2019. Contributions of elastic fibers, collagen, and extracellular matrix to the multiaxial mechanics of ligament. J Mech Behav Biomed Mater 99:118–126.

131. Xie F, Yang L, Guo L, et al. 2009. A study on construction three-dimensional nonlinear finite element model and stress distribution analysis of anterior cruciate ligament. J Biomech Eng 131(12).

132. Anderson P, Fels S, Harandi NM, et al. 2017. FRANK. In: Biomechanics of Living Organs. Elsevier. p 413–447.

133. Nesbitt DQ, Nelson ML, Shannon KS, Lujan TJ. 2023. Dots-on-Plots: A Web Application to Analyze Stress–Strain Curves From Tensile Tests of Soft Tissue. J Biomech Eng 145(2).

134. Peña E. 2011. A rate dependent directional damage model for fibred materials: Application to soft biological tissues. Comput Mech 48(4):407–420.

135. Fereidoonnezhad B, Naghdabadi R, Holzapfel GA. 2016. Stress softening and permanent deformation in human aortas: Continuum and computational modeling with application to arterial clamping. J Mech Behav Biomed Mater 61:600–616.

136. García A, Martínez MA, Peña E. 2013. Determination and modeling of the inelasticity over the length of the porcine carotid artery. J Biomech Eng 135(3).

137. Hernández B, Peña E, Pascual G, et al. 2011. Mechanical and histological characterization of the abdominal muscle. A previous step to modelling hernia surgery. J Mech Behav Biomed Mater 4(3):392–404.

138. Buckley MR, Dunkman AA, Reuther KE, et al. 2013. Validation of an empirical damage model for aging and in vivo injury of the murine patellar tendon. J Biomech Eng 135(4).

139. Gustafson HM, Cripton PA, Ferguson SJ, Helgason B. 2017. Comparison of specimen-specific vertebral body finite element models with experimental digital image correlation measurements. J Mech Behav Biomed Mater 65:801–807.

140. Maghami E, Pejman R, Najafi AR. 2021. Fracture micromechanics of human dentin: A microscale numerical model. J Mech Behav Biomed Mater 114.

141. Mondal S, Olsen-Kettle LM, Gross L. 2020. Regularization of continuum damage mechanics models for 3-D brittle materials using implicit gradient enhancement. Comput Geotech 122.

142. Zreid I, Kaliske M. 2014. Regularization of microplane damage models using an implicit gradient enhancement. Int J Solids Struct 51(19–20):3480–3489.

143. Gardiner JC, Weiss JA. 2003. Subject-specific finite element analysis of the human medial collateral ligament during valgus knee loading. Journal of Orthopaedic Research 21(6):1098–1106.

144. Davis JL, Dumont ER, Strait DS, Grosse IR. 2011. An efficient method of modeling material properties using a thermal diffusion analogy: An example based on craniofacial bone. PLoS One 6(2).

145. Martin C, Sun W. 2013. Modeling of long-term fatigue damage of soft tissue with stress softening and permanent set effects. Biomech Model Mechanobiol 12(4):645–655.

146. Karimi A, Grytz R, Rahmati SM, et al. 2021. Analysis of the effects of finite element type within a 3D biomechanical model of a human optic nerve head and posterior pole. Comput Methods Programs Biomed 198.

147. Vaquero J, Forriol F, Ceu P, et al. 2016. Meniscus tear surgery and meniscus replacement Corresponding author :6(1):71–89.

148. Kwok J, Grogan S, Meckes B, et al. 2014. Atomic force microscopy reveals age-dependent changes in nanomechanical properties of the extracellular matrix of native human menisci: Implications for joint degeneration and osteoarthritis. Nanomedicine 10(8):1777–1785 Available from: http://dx.doi.org/10.1016/j.nano.2014.06.010.

149. Gelse K, Pöschl E, Aigner T. 2003. Collagens - Structure, function, and biosynthesis. Adv Drug Deliv Rev 55(12):1531–1546.

150. Han B, Li Q, Wang C, et al. 2019. Decorin Regulates the Aggrecan Network Integrity and Biomechanical Functions of Cartilage Extracellular Matrix. ACS Nano 13(10):11320–11333.

151. Vynios DH, Papageorgakopoulou N, Sazakli H, Tsiganos CP. 2001. The interactions of cartilage proteoglycans with collagens are determined by their structures.

152. Lindahl U, Kjellén L. 2013. Pathophysiology of heparan sulphate: Many diseases, few drugs. J Intern Med 273(6):555–571.

153. Arvidsson M, Ahmed A, Bouzina H, Rådegran G. 2021. Plasma proteoglycan prolargin in diagnosis and differentiation of pulmonary arterial hypertension. ESC Heart Fail 8(2):1230–1243.

154. Kristensen JH, Karsdal MA. 2016. Elastin. In: Biochemistry of Collagens, Laminins and Elastin. Elsevier. p 197–201.

155. Mcalinden A, Dudhia J, Bolton MC, et al. 2001. Age-related changes in the synthesis and mRNA expression of decorin and aggrecan in human meniscus and articular cartilage.:33–41.

156. Wilson CG, Vanderploeg EJ, Zuo F, et al. 2009. Aggrecanolysis and in vitro matrix degradation in the immature bovine meniscus : mechanisms and functional implications. Arthritis Res Ther 11(6):1–12.

157. Pauli C, Grogan SP, Patil S, et al. 2011. Macroscopic and histopathologic analysis of human knee menisci in aging and osteoarthritis. Osteoarthritis Cartilage 19(9):1132–1141 Available from: http://dx.doi.org/10.1016/j.joca.2011.05.008.

158. Ingman AM, Ghosh P, Taylor TKF. 1974. Variation of collagenous and non-collagenous proteins of human knee joint menisci with age and degeneration. Gerontologia 20(4):212–223.

159. Egner E. 1982. Knee Joint Meniscal Degeneration as it Relates to Tissue Fiber Structure and Mechanical Resistance. Pathol Res Pract 173:310–324.

160. Yoshida K, Jiang H, Kim MJ, et al. 2014. Quantitative evaluation of collagen crosslinks and corresponding tensile mechanical properties in mouse cervical tissue during normal pregnancy. PLoS One 9(11).

161. Tanaka S, Avigad G, Eikenberry EF, Brodsky B. 1988. Isolation and partial characterization of collagen chains dimerized by sugar-derived cross-links. J Biol Chem 263(33):17650–17657.

162. Andreassen TT, Oxlund H, Danielsen CC. 1988. The influence of non-enzymatic glycosylation and formation of fluorescent reaction products on the mechanical properties of rat tail tendons. Connect Tissue Res 17(1):1–9.

163. Reddy GK. 2004. Cross-Linking in Collagen by Nonenzymatic Glycation Increases the Matrix Stiffness in Rabbit Achilles Tendon. Exp Diabesity Res 5(2):143–153.

164. Sims TJ, Rasmussen LM, Oxlund H, Bailey AJ. 1996. The role of glycation cross-links in diabetic vascular stiffening. Diabetologia (39):946–951.

165. Hedman TP, Chen WP, Lin LC, et al. 2017. Effects of Collagen Crosslink Augmentation on Mechanism of Compressive Load Sharing in Intervertebral Discs. J Med Biol Eng 37(1):94–101.

166. Searle BC, Swearingen KE, Barnes CA, et al. 2020. Generating high quality libraries for DIA MS with empirically corrected peptide predictions. Nat Commun 11(1).

167. Sand JMB, Genovese F, Karsdal MA. 2016. Type IV Collagen. In: Biochemistry of Collagens, Laminins and Elastin. Elsevier. p 31–41.

168. Cescon M, Gattazzo F, Chen P, Bonaldo P. 2015. Collagen VI at a glance. J Cell Sci 128(19):3525–3531.

169. Andenæs K, Lunde IG, Mohammadzadeh N, et al. 2018. The extracellular matrix proteoglycan fibromodulin is upregulated in clinical and experimental heart failure and affects cardiac remodeling. PLoS One 13(7).

170. Xu T, Bianco P, Fisher LW, et al. 1998. Targeted disruption of the biglycan gene leads to an osteoporosis-like phenotype in mice. Nat Genet 20:78–82 Available from: http://genetics.nature.com.

171. Eleswarapu S V., Responte DJ, Athanasiou KA. 2011. Tensile properties, collagen content, and crosslinks in connective tissues of the immature knee joint. PLoS One 6(10).

172. Skrbic B, Engebretsen KVT, Strand ME, et al. 2015. Lack of collagen VIII reduces fibrosis and promotes early mortality and cardiac dilatation in pressure overload in mice. Cardiovasc Res 106(1):32–42.

173. Vizcaíno JA, Côté RG, Csordas A, et al. 2013. The Proteomics Identifications (PRIDE) database and associated tools: Status in 2013. Nucleic Acids Res 41(D1).

174. Naffa R, Holmes G, Ahn M, et al. 2016. Liquid chromatography-electrospray ionization mass spectrometry for the simultaneous quantitation of collagen and

elastin crosslinks. J Chromatogr A 1478:60–67 Available from: http://dx.doi.org/10.1016/j.chroma.2016.11.060.

175. Gineyts E, Borel O, Chapurlat R, Garnero P. 2010. Quantification of immature and mature collagen crosslinks by liquid chromatography-electrospray ionization mass spectrometry in connective tissues. J Chromatogr B Analyt Technol Biomed Life Sci 878(19):1449–1454.

176. Thurman TJ, Washam CL, Alkam D, et al. 2023. proteoDA: a package for quantitative proteomics. J Open Source Softw 8(85):5184 Available from: https://joss.theoj.org/papers/10.21105/joss.05184.

177. Benjamini Y, Hochberg Y. 1995. Controlling the False Discovery Rate: A Practical and Powerful Approach to Multiple Testing. 289–300 p.

178. Statistics Kingdom. 2019. http://statskingdom.com/.

179. Alexopoulos LG, Youn I, Bonaldo P, Guilak F. 2009. Developmental and osteoarthritic changes in Col6a1-knockout mice: Biomechanics of type VI collagen in the cartilage pericellular matrix. Arthritis Rheum 60(3):771–779.

180. Embree MC, Kilts TM, Ono M, et al. 2010. Biglycan and fibromodulin have essential roles in regulating chondrogenesis and extracellular matrix turnover in temporomandibular joint osteoarthritis. American Journal of Pathology 176(2):812–826.

181. Bengtsson E, Mörgelin M, Sasaki T, et al. 2002. The leucine-rich repeat protein PRELP binds perlecan and collagens and may function as a basement membrane anchor. Journal of Biological Chemistry 277(17):15061–15068.

182. Henninger HB, Underwood CJ, Romney SJ, et al. 2013. Effect of elastin digestion on the quasi-static tensile response of medial collateral ligament. Journal of Orthopaedic Research 31(8):1226–1233.

183. Sutmuller M, Bruijn JA, De Heer E. 1997. Histology and Histopathology From Cell Biology to Tissue Engineering Collagen types VIII and X, two non-fibrillar, short-chain collagens. Structure homologies, functions and involvement in pathology. Histol Histopathol 12:557–566 Available from: http://www.hh.um.es.

184. Nakano M, Nakamura Y, Suzuki T, et al. 2020. Pentosidine and carboxymethyl-lysine associate differently with prevalent osteoporotic vertebral fracture and various bone markers. Sci Rep 10(1).

185. Delgado-Andrade C. 2016. Carboxymethyl-lysine: Thirty years of investigation in the field of AGE formation. Food Funct 7(1):46–57.

186. Mine T, Ihara K, Kawamura H, et al. 2013. Collagen expression in various degenerative meniscal changes: an immunohistological study. J Orthop Surg (Hong Kong) 21(2):216–220.

187. Sophia Fox AJ, Bedi A, Rodeo SA. 2009. The basic science of articular cartilage: Structure, composition, and function. Sports Health 1(6):461–468.

188. Yanagishita M. 1993. Function of proteoglycans in the extracellular matrix. Pathol Int 43(6):283–293.

189. Osakabe T, Hayashi M, Hasegawa K, et al. 2001. Age- and Gender-Related Changes in Ligament Components. 527–532 p.

190. Godinho MSC, Thorpe CT, Greenwald SE, Screen HRC. 2017. Elastin is Localised to the Interfascicular Matrix of Energy Storing Tendons and Becomes Increasingly Disorganised With Ageing. Sci Rep 7(1).

191. Sugiyama Y, Naito K, Goto K, et al. 2019. Effect of aging on the tendon structure and tendon-associated gene expression in mouse foot flexor tendon. Biomed Rep 10(4):238–244.

192. Takahashi M, Kushida K, Ohishi T, et al. 1994. Quantitative analysis of crosslinks pyridinoline and pentosidine in articular cartilage of patients with bone and joint disorders. Arthritis Rheum 37(5):724–728.

193. Di Medio L, Brandi ML. 2021. Advances in bone turnover markers. p 101–140.

194. Eyre DR, Koob TJ, Van Ness KP. 1984. Quantitation of hydroxypyridinium crosslinks in collagen by high-performance liquid chromatography. Anal Biochem 137(2):380–388.

195. Derwich M, Mitus-kenig M, Pawlowska E. 2021. Mechanisms of action and efficacy of hyaluronic acid, corticosteroids and platelet-rich plasma in the treatment of temporomandibular joint osteoarthritis—a systematic review. Int J Mol Sci 22(14).

196. Nesbitt DQ, Burruel DE, Henderson BS, Lujan TJ. 2023. Finite element modeling of meniscal tears using continuum damage mechanics and digital image correlation. Sci Rep 13(1).

197. Advanced Mechanical Technology Inc. 2023. VIVO Joint Simulator. https://www.amti.biz/product/vivo-simulator/ .

198. Bonifasi-Lista C, Lake SP, Small MS, Weiss JA. 2005. Viscoelastic properties of the human medial collateral ligament under longitudinal, transverse and shear loading. J Orthop Res 23(1):67–76 Available from: http://www.ncbi.nlm.nih.gov/pubmed/15607877.

199. Henderson BS, Cudworth KF, Wale ME, et al. 2022. Tensile fatigue strength and endurance limit of human meniscus. J Mech Behav Biomed Mater 127.

200. Fox AJS, Wanivenhaus F, Burge AJ, et al. 2015. The human meniscus: A review of anatomy, function, injury, and advances in treatment. Clinical Anatomy 28(2):269–287.

201. Hauch KN, Villegas DF, Haut Donahue TL. 2010. Geometry, time-dependent and failure properties of human meniscal attachments. J Biomech 43(3):463–468 Available from: http://dx.doi.org/10.1016/j.jbiomech.2009.09.043.

202. Villegas DF, Maes JA, Magee SD, Haut Donahue TL. 2007. Failure properties and strain distribution analysis of meniscal attachments. J Biomech 40(12):2655–2662.

203. Abraham AC, Moyer JT, Villegas DF, et al. 2011. Hyperelastic properties of human meniscal attachments. J Biomech 44(3):413–418 Available from: http://dx.doi.org/10.1016/j.jbiomech.2010.10.001.

204. Andrews SHJ, Rattner JB, Abusara Z, et al. 2014. Tie-fibre structure and organization in the knee menisci. J Anat 224(5):531–537.

APPENDIX A

Chapter 3 Supplemental Material

Automated Analysis of Mechanical Properties

A custom MATLAB script automated the identification of four points of interest on the stress-strain curve: transition, yield, ultimate, and rupture. The yield point was selected at the maximum slope of the stress-strain curve, the UTS point at the maximum stress, and the rupture point when stress dropped below 15% of UTS. Five specimens from the transverse group did not reach the threshold of 15% of the UTS stress before the test was halted. These five specimens were not included in any calculations using rupture strain. The transition point was determined as the point in the toe region (longitudinal specimens only) where the slope of the stress-strain curve deviated by 10% from the tangent modulus, where tangent modulus was calculated from the slope near the yield point [13].

High-Speed Video and DIC

During the tensile tests, a film speed of 500 fps was saved for 20 milliseconds before and after all points of interest, but otherwise the number of images were truncated down to 5 fps to reduce data density. Digital image correlation was performed in MATLAB using NCORR[74]. The DIC subset size was set to 0.2 mm, and the subset size to calculate strains from subset displacement was set to 0.1 mm. An incremental DIC method was used to help prevent decorrelation in the high strain cases seen in transverse specimens. For this incremental method, we analyzed 133 ± 29 frames up to UTS for longitudinal specimens, and 280 ± 92 frames up to UTS for transverse specimens. When we tried using direct DIC, where only the reference frame and frame at the current point of interest were analyzed, one third of transverse specimens failed to produce results at UTS, and those that produced results had decorrelation in 23% of the region of interest, on average. By comparing results between incremental and direct DIC for the longitudinal specimens, we calculated the cumulative error of using incremental DIC for longitudinal specimens to be 0.04% strain and estimated the cumulative error of using incremental DIC for transverse specimens to by 0.08%.

Comparison of Mechanical Properties to Previous Studies on Human Meniscus

Mechanical properties calculated in the present study compare relatively well to prior biomechanics research on human meniscus. The ultimate tensile strength and tangent modulus we calculated for longitudinal specimens (Table 2) were within 10% of values reported in two studies[26,27], and our average ultimate grip strain for transverse specimens was nearly identical to values reported by Tissakht and Ahmed[7]. Larger differences existed for our ultimate grip strain in longitudinal specimens, which was between 10-75% lower than previous studies[7,26,27]. Also, our ultimate tensile strength for transverse specimens was one-fourth of a previously reported value[7]. A likely reason for this difference is that we layered our transverse specimens on an orthogonal plane to the Tissakht and Ahmed study, where tie fibers are less dense[204].

APPENDIX B

Chapter 6 Supplemental Material

Additional detail regarding the function of structural molecules from Table 9 can be seen in Table 11, to include the tissues that the relevant study of function were performed on.

Table 11. Effect of Aging on Meniscus ECM Proteins and Collagen Crosslink Molecules.

	Molecule	Tissue	Structural Role in Tissue	Log_2-Fold Change with Age	CI (95%)
ECM Structural Proteins	Collagen IV	Skin	Main structural component of the basement membrane[36].	-1.24*	-2.04, -0.44
	Collagen VI	Cartilage	Absence results in decreased cartilage stiffness and accelerated development of OA degeneration[37,48].	-1.19*	-1.71, -0.66
	Fibromodulin	Cardiac tissue	Binds to collagen regulating fibrillogenesis and influences crosslinking[38].	-1.14*	-1.67, -0.61
	Biglycan	Bone, cartilage	Assists in mineralization of bone and connective tissues[39]. Regulates ECM turnover[49].	-0.85*	-1.25, -0.44
	Prolargin	Cartilage, arterial tissue	Binds Col1 and Col2 to basement memberanes[50].	-0.82*	-1.16, -0.49
	Decorin	Cartilage	Assists in ECM assembly and promotes adhesion between aggrecan and collagen II[10].	-0.47*	-0.82, -0.12
	Elastin	Ligament	Provides resilience and elasticity, approximately 1000 times more flexible than collagens[14,51].	0.16	-0.33, 0.92
	Collagen I	Ligaments, tendon	Key structural component of the tensile integrity of connective tissue[8,40].	0.39	-0.32, 1.11
	Collagen VIII	Cardiac tissue	Short chain network-forming collagen assisting in porous structure to withstand compressive forces[52].	2.56*	1.82, 3.29
	Collagen II	Meniscus	Interacts with proteoglycans[8] to improve compressive strength via osmotic pressure[9].	3.00*	1.67, 4.34
Collagen Crosslinks	DPD	Meniscus, cervical tissue	Mature collagen crosslink that stabilizes molecules and helps with matrix tensile strength[22,24].	-0.74*	-1.43, -0.05
	CML	Skin, bone	An AGE associated with bone fracture risk and an indicator of aging and oxidative stress[53,54].	0.74*	0.08, 1.40
	PEN	Meniscus, bone	An AGE associated with reduced bone strength and loss of toughness in various soft tissues[24,53].	1.43*	0.17, 2.70
	DHLNL	Cervical tissue	Immature collagen crosslink present during tissue remodeling[22].	1.43*	0.66, 2.24

*Significantly different between age groups ($p < 0.05$).

A table with a comprehensive list of all of the proteins with significant changes due to age can be seen in Table 12. A positive log fold change value indicates the older age group showed an increase in the protein, whereas a negative value indicates less of the protein.

Table 12: All proteins with significant differences between age groups.

Protein Name	Log_2 Fold Change	*P.* Value
TMED2_HUMAN Transmembrane emp24 domain-containing protein 2 OS=Homo sapiens OX=9606 GN=TMED2 PE=1 SV=1	5.040	0.000
APOA4_HUMAN Apolipoprotein A-IV OS=Homo sapiens OX=9606 GN=APOA4 PE=1 SV=3	3.036	0.000
TIMP3_HUMAN Metalloproteinase inhibitor 3 OS=Homo sapiens OX=9606 GN=TIMP3 PE=1 SV=2	3.097	0.000
CO8A1_HUMAN Collagen alpha-1(VIII) chain OS=Homo sapiens OX=9606 GN=COL8A1 PE=1 SV=2	2.558	0.000
ZG16_HUMAN Zymogen granule membrane protein 16 OS=Homo sapiens OX=9606 GN=ZG16 PE=1 SV=2	2.725	0.000
PLMN_HUMAN Plasminogen OS=Homo sapiens OX=9606 GN=PLG PE=1 SV=2	1.436	0.000
CQ058_HUMAN UPF0450 protein C17orf58 OS=Homo sapiens OX=9606 GN=C17orf58 PE=3 SV=2	3.355	0.000
NDNF_HUMAN Protein NDNF OS=Homo sapiens OX=9606 GN=NDNF PE=1 SV=2	2.602	0.000
SAMP_HUMAN Serum amyloid P-component OS=Homo sapiens OX=9606 GN=APCS PE=1 SV=2	1.684	0.000
CRLF1_HUMAN Cytokine receptor-like factor 1 OS=Homo sapiens OX=9606 GN=CRLF1 PE=1 SV=1	2.449	0.000
IL17D_HUMAN Interleukin-17D OS=Homo sapiens OX=9606 GN=IL17D PE=2 SV=1	2.662	0.000
PF4V_HUMAN Platelet factor 4 variant OS=Homo sapiens OX=9606 GN=PF4V1 PE=1 SV=1	2.222	0.000
ANTR2_HUMAN Anthrax toxin receptor 2 OS=Homo sapiens OX=9606 GN=ANTXR2 PE=1 SV=5	2.504	0.000
METRL_HUMAN Meteorin-like protein OS=Homo sapiens OX=9606 GN=METRNL PE=2 SV=1	2.094	0.000
PXYP1_HUMAN 2-phosphoxylose phosphatase 1 OS=Homo sapiens OX=9606 GN=PXYLP1 PE=1 SV=1	2.353	0.000
DNJC3_HUMAN DnaJ homolog subfamily C member 3 OS=Homo sapiens OX=9606 GN=DNAJC3 PE=1 SV=1	2.332	0.000
ITIH6_HUMAN Inter-alpha-trypsin inhibitor heavy chain H6 OS=Homo sapiens OX=9606 GN=ITIH6 PE=2 SV=1	2.751	0.000
CHM4B_HUMAN Charged multivesicular body protein 4b OS=Homo sapiens OX=9606 GN=CHMP4B PE=1 SV=1	1.010	0.000
MGAT1_HUMAN Alpha-1,3-mannosyl-glycoprotein 2-beta-N-acetylglucosaminyltransferase OS=Homo sapiens OX=9606 GN=MGAT1 PE=1 SV=2	1.826	0.000
DDX6_HUMAN Probable ATP-dependent RNA helicase DDX6 OS=Homo sapiens OX=9606 GN=DDX6 PE=1 SV=2	1.472	0.000
LAG3_HUMAN Lymphocyte activation gene 3 protein OS=Homo sapiens OX=9606 GN=LAG3 PE=1 SV=5	3.233	0.000
TNF13_HUMAN Tumor necrosis factor ligand superfamily member 13 OS=Homo sapiens OX=9606 GN=TNFSF13 PE=1 SV=1	2.441	0.000

SEM3E_HUMAN Semaphorin-3E OS=Homo sapiens OX=9606 GN=SEMA3E PE=1 SV=1	2.603	0.000
CHSTE_HUMAN Carbohydrate sulfotransferase 14 OS=Homo sapiens OX=9606 GN=CHST14 PE=1 SV=2	1.582	0.000
SEM3B_HUMAN Semaphorin-3B OS=Homo sapiens OX=9606 GN=SEMA3B PE=2 SV=1	2.163	0.000
CHSTC_HUMAN Carbohydrate sulfotransferase 12 OS=Homo sapiens OX=9606 GN=CHST12 PE=2 SV=2	1.600	0.000
ERF1_HUMAN Eukaryotic peptide chain release factor subunit 1 OS=Homo sapiens OX=9606 GN=ETF1 PE=1 SV=3	0.920	0.000
CADH1_HUMAN Cadherin-1 OS=Homo sapiens OX=9606 GN=CDH1 PE=1 SV=3	1.720	0.000
CHST3_HUMAN Carbohydrate sulfotransferase 3 OS=Homo sapiens OX=9606 GN=CHST3 PE=1 SV=3	1.843	0.000
CHST6_HUMAN Carbohydrate sulfotransferase 6 OS=Homo sapiens OX=9606 GN=CHST6 PE=1 SV=1	1.978	0.001
LPAR1_HUMAN Lysophosphatidic acid receptor 1 OS=Homo sapiens OX=9606 GN=LPAR1 PE=1 SV=3	2.048	0.001
C1TC_HUMAN C-1-tetrahydrofolate synthase, cytoplasmic OS=Homo sapiens OX=9606 GN=MTHFD1 PE=1 SV=3	1.738	0.001
POSTN_HUMAN Periostin OS=Homo sapiens OX=9606 GN=POSTN PE=1 SV=2	0.920	0.001
QSOX1_HUMAN Sulfhydryl oxidase 1 OS=Homo sapiens OX=9606 GN=QSOX1 PE=1 SV=3	1.317	0.001
DAF_HUMAN Complement decay-accelerating factor OS=Homo sapiens OX=9606 GN=CD55 PE=1 SV=4	1.569	0.001
FINC_HUMAN Fibronectin OS=Homo sapiens OX=9606 GN=FN1 PE=1 SV=4	0.981	0.001
MIA_HUMAN Melanoma-derived growth regulatory protein OS=Homo sapiens OX=9606 GN=MIA PE=1 SV=1	1.949	0.001
SEM3D_HUMAN Semaphorin-3D OS=Homo sapiens OX=9606 GN=SEMA3D PE=2 SV=2	2.188	0.001
CHRD_HUMAN Chordin OS=Homo sapiens OX=9606 GN=CHRD PE=1 SV=2	10.238	0.001
CRAC1_HUMAN Cartilage acidic protein 1 OS=Homo sapiens OX=9606 GN=CRTAC1 PE=1 SV=2	0.987	0.001
SEM3C_HUMAN Semaphorin-3C OS=Homo sapiens OX=9606 GN=SEMA3C PE=2 SV=2	1.913	0.001
CO2A1_HUMAN Collagen alpha-1(II) chain OS=Homo sapiens OX=9606 GN=COL2A1 PE=1 SV=3	3.003	0.002
MA1A1_HUMAN Mannosyl-oligosaccharide 1,2-alpha-mannosidase IA OS=Homo sapiens OX=9606 GN=MAN1A1 PE=1 SV=3	1.139	0.002
TRPV4_HUMAN Transient receptor potential cation channel subfamily V member 4 OS=Homo sapiens OX=9606 GN=TRPV4 PE=1 SV=2	1.506	0.002
STEA3_HUMAN Metalloreductase STEAP3 OS=Homo sapiens OX=9606 GN=STEAP3 PE=1 SV=2	1.842	0.002
CALM2_HUMAN Calmodulin-2 OS=Homo sapiens OX=9606 GN=CALM2 PE=1 SV=1	1.043	0.003
CALM3_HUMAN Calmodulin-3 OS=Homo sapiens OX=9606 GN=CALM3 PE=1 SV=1	1.043	0.003
CBPB2_HUMAN Carboxypeptidase B2 OS=Homo sapiens OX=9606 GN=CPB2 PE=1 SV=2	1.119	0.003
ECM2_HUMAN Extracellular matrix protein 2 OS=Homo sapiens OX=9606 GN=ECM2 PE=2 SV=1	1.842	0.003
OAF_HUMAN Out at first protein homolog OS=Homo sapiens OX=9606 GN=OAF PE=2 SV=1	1.903	0.003
HS3S1_HUMAN Heparan sulfate glucosamine 3-O-sulfotransferase 1 OS=Homo sapiens OX=9606 GN=HS3ST1 PE=1 SV=1	2.088	0.003
PPT1_HUMAN Palmitoyl-protein thioesterase 1 OS=Homo sapiens OX=9606 GN=PPT1 PE=1 SV=1	0.983	0.003
SULF2_HUMAN Extracellular sulfatase Sulf-2 OS=Homo sapiens OX=9606 GN=SULF2 PE=1 SV=1	2.208	0.003

FIBIN_HUMAN Fin bud initiation factor homolog OS=Homo sapiens OX=9606 GN=FIBIN PE=1 SV=1	2.113	0.004
HIPL2_HUMAN HHIP-like protein 2 OS=Homo sapiens OX=9606 GN=HHIPL2 PE=1 SV=1	1.755	0.004
CFA20_HUMAN Cilia- and flagella-associated protein 20 OS=Homo sapiens OX=9606 GN=CFAP20 PE=1 SV=1	1.032	0.004
DIK2A_HUMAN Divergent protein kinase domain 2A OS=Homo sapiens OX=9606 GN=DIPK2A PE=1 SV=1	1.347	0.004
FBLN7_HUMAN Fibulin-7 OS=Homo sapiens OX=9606 GN=FBLN7 PE=2 SV=1	1.520	0.004
MGP_HUMAN Matrix Gla protein OS=Homo sapiens OX=9606 GN=MGP PE=1 SV=2	1.566	0.004
GANAB_HUMAN Neutral alpha-glucosidase AB OS=Homo sapiens OX=9606 GN=GANAB PE=1 SV=3	0.532	0.005
PONL1_HUMAN Podocan-like protein 1 OS=Homo sapiens OX=9606 GN=PODNL1 PE=2 SV=2	3.153	0.005
CO4B_HUMAN Complement C4-B OS=Homo sapiens OX=9606 GN=C4B PE=1 SV=2	1.489	0.006
TRI47_HUMAN E3 ubiquitin-protein ligase TRIM47 OS=Homo sapiens OX=9606 GN=TRIM47 PE=1 SV=2	0.897	0.007
LFTY2_HUMAN Left-right determination factor 2 OS=Homo sapiens OX=9606 GN=LEFTY2 PE=1 SV=2	1.730	0.007
IPSP_HUMAN Plasma serine protease inhibitor OS=Homo sapiens OX=9606 GN=SERPINA5 PE=1 SV=3	1.027	0.007
CNNM3_HUMAN Metal transporter CNNM3 OS=Homo sapiens OX=9606 GN=CNNM3 PE=1 SV=1	1.184	0.007
CCD80_HUMAN Coiled-coil domain-containing protein 80 OS=Homo sapiens OX=9606 GN=CCDC80 PE=1 SV=1	1.710	0.007
PRPS2_HUMAN Ribose-phosphate pyrophosphokinase 2 OS=Homo sapiens OX=9606 GN=PRPS2 PE=1 SV=2	0.924	0.007
APOC1_HUMAN Apolipoprotein C-I OS=Homo sapiens OX=9606 GN=APOC1 PE=1 SV=1	1.293	0.007
2ABA_HUMAN Serine/threonine-protein phosphatase 2A 55 kDa regulatory subunit B alpha isoform OS=Homo sapiens OX=9606 GN=PPP2R2A PE=1 SV=1	0.927	0.008
KCC1D_HUMAN Calcium/calmodulin-dependent protein kinase type 1D OS=Homo sapiens OX=9606 GN=CAMK1D PE=1 SV=1	1.150	0.008
RL9_HUMAN 60S ribosomal protein L9 OS=Homo sapiens OX=9606 GN=RPL9 PE=1 SV=1	1.515	0.008
TGM2_HUMAN Protein-glutamine gamma-glutamyltransferase 2 OS=Homo sapiens OX=9606 GN=TGM2 PE=1 SV=2	1.181	0.008
FA49A_HUMAN Protein FAM49A OS=Homo sapiens OX=9606 GN=FAM49A PE=2 SV=1	1.020	0.008
GLCM_HUMAN Lysosomal acid glucosylceramidase OS=Homo sapiens OX=9606 GN=GBA PE=1 SV=3	0.785	0.009
RNAS4_HUMAN Ribonuclease 4 OS=Homo sapiens OX=9606 GN=RNASE4 PE=1 SV=3	1.396	0.009
AAMDC_HUMAN Mth938 domain-containing protein OS=Homo sapiens OX=9606 GN=AAMDC PE=1 SV=1	1.234	0.009
ANGL2_HUMAN Angiopoietin-related protein 2 OS=Homo sapiens OX=9606 GN=ANGPTL2 PE=1 SV=1	1.037	0.009
PUR2_HUMAN Trifunctional purine biosynthetic protein adenosine-3 OS=Homo sapiens OX=9606 GN=GART PE=1 SV=1	0.626	0.009
TR11B_HUMAN Tumor necrosis factor receptor superfamily member 11B OS=Homo sapiens OX=9606 GN=TNFRSF11B PE=1 SV=3	1.689	0.010
STON1_HUMAN Stonin-1 OS=Homo sapiens OX=9606 GN=STON1 PE=1 SV=2	0.965	0.010
CHMP3_HUMAN Charged multivesicular body protein 3 OS=Homo sapiens OX=9606 GN=CHMP3 PE=1 SV=3	0.694	0.010
GALT2_HUMAN Polypeptide N-acetylgalactosaminyltransferase 2 OS=Homo sapiens OX=9606 GN=GALNT2 PE=1 SV=1	0.831	0.010

B4GT1_HUMAN Beta-1,4-galactosyltransferase 1 OS=Homo sapiens OX=9606 GN=B4GALT1 PE=1 SV=5	1.022	0.011
LAMA5_HUMAN Laminin subunit alpha-5 OS=Homo sapiens OX=9606 GN=LAMA5 PE=1 SV=8	1.040	0.011
ALS_HUMAN Insulin-like growth factor-binding protein complex acid labile subunit OS=Homo sapiens OX=9606 GN=IGFALS PE=1 SV=1	1.092	0.011
1A11_HUMAN HLA class I histocompatibility antigen, A-11 alpha chain OS=Homo sapiens OX=9606 GN=HLA-A PE=1 SV=1	1.442	0.011
1A01_HUMAN HLA class I histocompatibility antigen, A-1 alpha chain OS=Homo sapiens OX=9606 GN=HLA-A PE=1 SV=1	1.442	0.011
1A36_HUMAN HLA class I histocompatibility antigen, A-36 alpha chain OS=Homo sapiens OX=9606 GN=HLA-A PE=1 SV=1	1.442	0.011
BIEA_HUMAN Biliverdin reductase A OS=Homo sapiens OX=9606 GN=BLVRA PE=1 SV=2	0.642	0.011
RAB13_HUMAN Ras-related protein Rab-13 OS=Homo sapiens OX=9606 GN=RAB13 PE=1 SV=1	0.697	0.011
GPC6_HUMAN Glypican-6 OS=Homo sapiens OX=9606 GN=GPC6 PE=1 SV=1	1.507	0.011
EDIL3_HUMAN EGF-like repeat and discoidin I-like domain-containing protein 3 OS=Homo sapiens OX=9606 GN=EDIL3 PE=1 SV=1	1.587	0.011
LOXL4_HUMAN Lysyl oxidase homolog 4 OS=Homo sapiens OX=9606 GN=LOXL4 PE=1 SV=1	1.432	0.011
PGRP2_HUMAN N-acetylmuramoyl-L-alanine amidase OS=Homo sapiens OX=9606 GN=PGLYRP2 PE=1 SV=1	1.215	0.012
GPM6A_HUMAN Neuronal membrane glycoprotein M6-a OS=Homo sapiens OX=9606 GN=GPM6A PE=1 SV=2	1.327	0.012
GDF5_HUMAN Growth/differentiation factor 5 OS=Homo sapiens OX=9606 GN=GDF5 PE=1 SV=3	1.452	0.013
AGM1_HUMAN Phosphoacetylglucosamine mutase OS=Homo sapiens OX=9606 GN=PGM3 PE=1 SV=1	0.832	0.013
ANKH_HUMAN Progressive ankylosis protein homolog OS=Homo sapiens OX=9606 GN=ANKH PE=1 SV=2	1.067	0.013
LRP1B_HUMAN Low-density lipoprotein receptor-related protein 1B OS=Homo sapiens OX=9606 GN=LRP1B PE=1 SV=2	1.608	0.013
PMVK_HUMAN Phosphomevalonate kinase OS=Homo sapiens OX=9606 GN=PMVK PE=1 SV=3	0.916	0.013
KCMA1_HUMAN Calcium-activated potassium channel subunit alpha-1 OS=Homo sapiens OX=9606 GN=KCNMA1 PE=1 SV=2	0.978	0.013
UGGG2_HUMAN UDP-glucose:glycoprotein glucosyltransferase 2 OS=Homo sapiens OX=9606 GN=UGGT2 PE=1 SV=4	1.283	0.013
GDF10_HUMAN Growth/differentiation factor 10 OS=Homo sapiens OX=9606 GN=GDF10 PE=2 SV=1	1.934	0.013
GNPI2_HUMAN Glucosamine-6-phosphate isomerase 2 OS=Homo sapiens OX=9606 GN=GNPDA2 PE=1 SV=1	7.931	0.013
CIRBP_HUMAN Cold-inducible RNA-binding protein OS=Homo sapiens OX=9606 GN=CIRBP PE=1 SV=1	1.480	0.014
GLT16_HUMAN Polypeptide N-acetylgalactosaminyltransferase 16 OS=Homo sapiens OX=9606 GN=GALNT16 PE=1 SV=2	1.419	0.015
PA2GA_HUMAN Phospholipase A2, membrane associated OS=Homo sapiens OX=9606 GN=PLA2G2A PE=1 SV=2	2.199	0.016
CTL1_HUMAN Choline transporter-like protein 1 OS=Homo sapiens OX=9606 GN=SLC44A1 PE=1 SV=1	1.002	0.016
PRG4_HUMAN Proteoglycan 4 OS=Homo sapiens OX=9606 GN=PRG4 PE=1 SV=3	0.982	0.017
PEPL_HUMAN Periplakin OS=Homo sapiens OX=9606 GN=PPL PE=1 SV=4	1.269	0.017
FHR2_HUMAN Complement factor H-related protein 2 OS=Homo sapiens OX=9606 GN=CFHR2 PE=1 SV=1	1.679	0.017
RIC8A_HUMAN Synembryn-A OS=Homo sapiens OX=9606 GN=RIC8A PE=1 SV=3	0.757	0.017

ARLY_HUMAN Argininosuccinate lyase OS=Homo sapiens OX=9606 GN=ASL PE=1 SV=4	1.034	0.017
FHR5_HUMAN Complement factor H-related protein 5 OS=Homo sapiens OX=9606 GN=CFHR5 PE=1 SV=1	1.349	0.018
UBXN6_HUMAN UBX domain-containing protein 6 OS=Homo sapiens OX=9606 GN=UBXN6 PE=1 SV=1	0.912	0.018
ARF4_HUMAN ADP-ribosylation factor 4 OS=Homo sapiens OX=9606 GN=ARF4 PE=1 SV=3	0.430	0.019
ITM2B_HUMAN Integral membrane protein 2B OS=Homo sapiens OX=9606 GN=ITM2B PE=1 SV=1	0.687	0.019
MINP1_HUMAN Multiple inositol polyphosphate phosphatase 1 OS=Homo sapiens OX=9606 GN=MINPP1 PE=1 SV=1	1.138	0.019
FGFP2_HUMAN Fibroblast growth factor-binding protein 2 OS=Homo sapiens OX=9606 GN=FGFBP2 PE=1 SV=1	2.010	0.019
VA0D1_HUMAN V-type proton ATPase subunit d 1 OS=Homo sapiens OX=9606 GN=ATP6V0D1 PE=1 SV=1	0.956	0.020
APOD_HUMAN Apolipoprotein D OS=Homo sapiens OX=9606 GN=APOD PE=1 SV=1	1.177	0.022
MMSA_HUMAN Methylmalonate-semialdehyde dehydrogenase [acylating], mitochondrial OS=Homo sapiens OX=9606 GN=ALDH6A1 PE=1 SV=2	0.813	0.022
AUGN_HUMAN Augurin OS=Homo sapiens OX=9606 GN=C2orf40 PE=1 SV=1	1.737	0.023
ENOG_HUMAN Gamma-enolase OS=Homo sapiens OX=9606 GN=ENO2 PE=1 SV=3	1.143	0.023
CTND1_HUMAN Catenin delta-1 OS=Homo sapiens OX=9606 GN=CTNND1 PE=1 SV=1	0.897	0.024
ARF6_HUMAN ADP-ribosylation factor 6 OS=Homo sapiens OX=9606 GN=ARF6 PE=1 SV=2	0.643	0.025
C1QT4_HUMAN Complement C1q tumor necrosis factor-related protein 4 OS=Homo sapiens OX=9606 GN=C1QTNF4 PE=1 SV=2	1.454	0.025
GDN_HUMAN Glia-derived nexin OS=Homo sapiens OX=9606 GN=SERPINE2 PE=1 SV=1	1.094	0.025
LOXL3_HUMAN Lysyl oxidase homolog 3 OS=Homo sapiens OX=9606 GN=LOXL3 PE=1 SV=1	1.262	0.025
GMPPB_HUMAN Mannose-1-phosphate guanyltransferase beta OS=Homo sapiens OX=9606 GN=GMPPB PE=1 SV=2	0.607	0.025
COBA2_HUMAN Collagen alpha-2(XI) chain OS=Homo sapiens OX=9606 GN=COL11A2 PE=1 SV=5	1.520	0.026
ARL3_HUMAN ADP-ribosylation factor-like protein 3 OS=Homo sapiens OX=9606 GN=ARL3 PE=1 SV=2	0.663	0.027
CILP1_HUMAN Cartilage intermediate layer protein 1 OS=Homo sapiens OX=9606 GN=CILP PE=1 SV=4	0.997	0.027
DESP_HUMAN Desmoplakin OS=Homo sapiens OX=9606 GN=DSP PE=1 SV=3	1.087	0.027
RAB34_HUMAN Ras-related protein Rab-34 OS=Homo sapiens OX=9606 GN=RAB34 PE=1 SV=1	0.846	0.028
HV343_HUMAN Immunoglobulin heavy variable 3-43 OS=Homo sapiens OX=9606 GN=IGHV3-43 PE=3 SV=1	2.808	0.028
XYLT1_HUMAN Xylosyltransferase 1 OS=Homo sapiens OX=9606 GN=XYLT1 PE=1 SV=1	1.282	0.028
SMOC2_HUMAN SPARC-related modular calcium-binding protein 2 OS=Homo sapiens OX=9606 GN=SMOC2 PE=2 SV=2	1.485	0.029
S29A1_HUMAN Equilibrative nucleoside transporter 1 OS=Homo sapiens OX=9606 GN=SLC29A1 PE=1 SV=3	1.179	0.030
CHID1_HUMAN Chitinase domain-containing protein 1 OS=Homo sapiens OX=9606 GN=CHID1 PE=1 SV=1	1.342	0.033
FNDC1_HUMAN Fibronectin type III domain-containing protein 1 OS=Homo sapiens OX=9606 GN=FNDC1 PE=2 SV=4	1.302	0.033
MYO1D_HUMAN Unconventional myosin-Id OS=Homo sapiens OX=9606 GN=MYO1D PE=1 SV=2	0.741	0.035

UFO_HUMAN Tyrosine-protein kinase receptor UFO OS=Homo sapiens OX=9606 GN=AXL PE=1 SV=4	0.933	0.035
CD97_HUMAN CD97 antigen OS=Homo sapiens OX=9606 GN=CD97 PE=1 SV=4	0.783	0.036
CO6_HUMAN Complement component C6 OS=Homo sapiens OX=9606 GN=C6 PE=1 SV=3	0.941	0.036
RL13_HUMAN 60S ribosomal protein L13 OS=Homo sapiens OX=9606 GN=RPL13 PE=1 SV=4	0.709	0.036
MK14_HUMAN Mitogen-activated protein kinase 14 OS=Homo sapiens OX=9606 GN=MAPK14 PE=1 SV=3	1.344	0.038
AP2B1_HUMAN AP-2 complex subunit beta OS=Homo sapiens OX=9606 GN=AP2B1 PE=1 SV=1	0.678	0.039
CLC3A_HUMAN C-type lectin domain family 3 member A OS=Homo sapiens OX=9606 GN=CLEC3A PE=1 SV=1	1.322	0.041
CCDC3_HUMAN Coiled-coil domain-containing protein 3 OS=Homo sapiens OX=9606 GN=CCDC3 PE=2 SV=1	1.300	0.041
MK03_HUMAN Mitogen-activated protein kinase 3 OS=Homo sapiens OX=9606 GN=MAPK3 PE=1 SV=4	0.787	0.041
DIP2C_HUMAN Disco-interacting protein 2 homolog C OS=Homo sapiens OX=9606 GN=DIP2C PE=1 SV=2	0.852	0.041
ARHL2_HUMAN ADP-ribose glycohydrolase ARH3 OS=Homo sapiens OX=9606 GN=ADPRHL2 PE=1 SV=1	1.180	0.044
PLCD1_HUMAN 1-phosphatidylinositol 4,5-bisphosphate phosphodiesterase delta-1 OS=Homo sapiens OX=9606 GN=PLCD1 PE=1 SV=2	0.645	0.044
GNA11_HUMAN Guanine nucleotide-binding protein subunit alpha-11 OS=Homo sapiens OX=9606 GN=GNA11 PE=1 SV=2	0.684	0.044
YES_HUMAN Tyrosine-protein kinase Yes OS=Homo sapiens OX=9606 GN=YES1 PE=1 SV=3	0.568	0.044
NIBAN_HUMAN Protein Niban OS=Homo sapiens OX=9606 GN=FAM129A PE=1 SV=1	0.720	0.046
ATL3_HUMAN ADAMTS-like protein 3 OS=Homo sapiens OX=9606 GN=ADAMTSL3 PE=1 SV=4	1.208	0.047
LV325_HUMAN Immunoglobulin lambda variable 3-25 OS=Homo sapiens OX=9606 GN=IGLV3-25 PE=1 SV=2	2.600	0.048
CN37_HUMAN 2',3'-cyclic-nucleotide 3'-phosphodiesterase OS=Homo sapiens OX=9606 GN=CNP PE=1 SV=2	0.836	0.048
SAA1_HUMAN Serum amyloid A-1 protein OS=Homo sapiens OX=9606 GN=SAA1 PE=1 SV=1	1.299	0.049
OLFL1_HUMAN Olfactomedin-like protein 1 OS=Homo sapiens OX=9606 GN=OLFML1 PE=1 SV=2	-2.027	0.000
ILF2_HUMAN Interleukin enhancer-binding factor 2 OS=Homo sapiens OX=9606 GN=ILF2 PE=1 SV=2	-1.009	0.000
CAD13_HUMAN Cadherin-13 OS=Homo sapiens OX=9606 GN=CDH13 PE=1 SV=1	-1.189	0.001
PRELP_HUMAN Prolargin OS=Homo sapiens OX=9606 GN=PRELP PE=1 SV=1	-0.822	0.001
CO6A3_HUMAN Collagen alpha-3(VI) chain OS=Homo sapiens OX=9606 GN=COL6A3 PE=1 SV=5	-1.221	0.001
CO6A1_HUMAN Collagen alpha-1(VI) chain OS=Homo sapiens OX=9606 GN=COL6A1 PE=1 SV=3	-1.188	0.002
DNPEP_HUMAN Aspartyl aminopeptidase OS=Homo sapiens OX=9606 GN=DNPEP PE=1 SV=1	-1.509	0.003
FMOD_HUMAN Fibromodulin OS=Homo sapiens OX=9606 GN=FMOD PE=1 SV=2	-1.139	0.003
H33_HUMAN Histone H3.3 OS=Homo sapiens OX=9606 GN=H3F3A PE=1 SV=2	-1.950	0.003
H32_HUMAN Histone H3.2 OS=Homo sapiens OX=9606 GN=HIST2H3A PE=1 SV=3	-1.950	0.003
H31T_HUMAN Histone H3.1t OS=Homo sapiens OX=9606 GN=HIST3H3 PE=1 SV=3	-1.950	0.003

1433B_HUMAN 14-3-3 protein beta/alpha OS=Homo sapiens OX=9606 GN=YWHAB PE=1 SV=3	-0.851	0.003
CO6A2_HUMAN Collagen alpha-2(VI) chain OS=Homo sapiens OX=9606 GN=COL6A2 PE=1 SV=4	-1.289	0.003
EHD2_HUMAN EH domain-containing protein 2 OS=Homo sapiens OX=9606 GN=EHD2 PE=1 SV=2	-0.704	0.003
H2B1O_HUMAN Histone H2B type 1-O OS=Homo sapiens OX=9606 GN=HIST1H2BO PE=1 SV=3	-1.244	0.004
H2B1B_HUMAN Histone H2B type 1-B OS=Homo sapiens OX=9606 GN=HIST1H2BB PE=1 SV=2	-1.244	0.004
H2B3B_HUMAN Histone H2B type 3-B OS=Homo sapiens OX=9606 GN=HIST3H2BB PE=1 SV=3	-1.244	0.004
H2B2E_HUMAN Histone H2B type 2-E OS=Homo sapiens OX=9606 GN=HIST2H2BE PE=1 SV=3	-1.244	0.004
EIF3A_HUMAN Eukaryotic translation initiation factor 3 subunit A OS=Homo sapiens OX=9606 GN=EIF3A PE=1 SV=1	-0.952	0.004
PGS1_HUMAN Biglycan OS=Homo sapiens OX=9606 GN=BGN PE=1 SV=2	-0.846	0.004
TM109_HUMAN Transmembrane protein 109 OS=Homo sapiens OX=9606 GN=TMEM109 PE=1 SV=1	-0.960	0.004
HS71B_HUMAN Heat shock 70 kDa protein 1B OS=Homo sapiens OX=9606 GN=HSPA1B PE=1 SV=1	-0.601	0.005
RSMN_HUMAN Small nuclear ribonucleoprotein-associated protein N OS=Homo sapiens OX=9606 GN=SNRPN PE=1 SV=1	-0.643	0.005
MPC2_HUMAN Mitochondrial pyruvate carrier 2 OS=Homo sapiens OX=9606 GN=MPC2 PE=1 SV=1	-1.663	0.005
ITB1_HUMAN Integrin beta-1 OS=Homo sapiens OX=9606 GN=ITGB1 PE=1 SV=2	-0.801	0.006
1433Z_HUMAN 14-3-3 protein zeta/delta OS=Homo sapiens OX=9606 GN=YWHAZ PE=1 SV=1	-0.596	0.006
ALDH2_HUMAN Aldehyde dehydrogenase, mitochondrial OS=Homo sapiens OX=9606 GN=ALDH2 PE=1 SV=2	-1.304	0.006
ACTN4_HUMAN Alpha-actinin-4 OS=Homo sapiens OX=9606 GN=ACTN4 PE=1 SV=2	-0.931	0.006
RSSA_HUMAN 40S ribosomal protein SA OS=Homo sapiens OX=9606 GN=RPSA PE=1 SV=4	-0.513	0.007
XRCC6_HUMAN X-ray repair cross-complementing protein 6 OS=Homo sapiens OX=9606 GN=XRCC6 PE=1 SV=2	-0.678	0.007
SHPS1_HUMAN Tyrosine-protein phosphatase non-receptor type substrate 1 OS=Homo sapiens OX=9606 GN=SIRPA PE=1 SV=2	-1.040	0.007
CO4A1_HUMAN Collagen alpha-1(IV) chain OS=Homo sapiens OX=9606 GN=COL4A1 PE=1 SV=4	-1.124	0.008
H2BFS_HUMAN Histone H2B type F-S OS=Homo sapiens OX=9606 GN=H2BFS PE=1 SV=2	-1.022	0.008
H2B1D_HUMAN Histone H2B type 1-D OS=Homo sapiens OX=9606 GN=HIST1H2BD PE=1 SV=2	-1.022	0.008
H2B1C_HUMAN Histone H2B type 1-C/E/F/G/I OS=Homo sapiens OX=9606 GN=HIST1H2BC PE=1 SV=4	-1.022	0.008
H2B2F_HUMAN Histone H2B type 2-F OS=Homo sapiens OX=9606 GN=HIST2H2BF PE=1 SV=3	-1.022	0.008
H2B1H_HUMAN Histone H2B type 1-H OS=Homo sapiens OX=9606 GN=HIST1H2BH PE=1 SV=3	-1.022	0.008
H2B1N_HUMAN Histone H2B type 1-N OS=Homo sapiens OX=9606 GN=HIST1H2BN PE=1 SV=3	-1.022	0.008
H2B1M_HUMAN Histone H2B type 1-M OS=Homo sapiens OX=9606 GN=HIST1H2BM PE=1 SV=3	-1.022	0.008
H2B1L_HUMAN Histone H2B type 1-L OS=Homo sapiens OX=9606 GN=HIST1H2BL PE=1 SV=3	-1.022	0.008
XRCC5_HUMAN X-ray repair cross-complementing protein 5 OS=Homo sapiens OX=9606 GN=XRCC5 PE=1 SV=3	-0.803	0.008
TENA_HUMAN Tenascin OS=Homo sapiens OX=9606 GN=TNC PE=1 SV=3	-1.254	0.008

ECH1_HUMAN Delta(3,5)-Delta(2,4)-dienoyl-CoA isomerase, mitochondrial OS=Homo sapiens OX=9606 GN=ECH1 PE=1 SV=2	-0.921	0.008
EIF3L_HUMAN Eukaryotic translation initiation factor 3 subunit L OS=Homo sapiens OX=9606 GN=EIF3L PE=1 SV=1	-0.818	0.009
HNRPU_HUMAN Heterogeneous nuclear ribonucleoprotein U OS=Homo sapiens OX=9606 GN=HNRNPU PE=1 SV=6	-0.714	0.009
S10A6_HUMAN Protein S100-A6 OS=Homo sapiens OX=9606 GN=S100A6 PE=1 SV=1	-0.739	0.010
DBLOH_HUMAN Diablo homolog, mitochondrial OS=Homo sapiens OX=9606 GN=DIABLO PE=1 SV=1	-0.837	0.010
TPM3_HUMAN Tropomyosin alpha-3 chain OS=Homo sapiens OX=9606 GN=TPM3 PE=1 SV=2	-0.969	0.010
BGH3_HUMAN Transforming growth factor-beta-induced protein ig-h3 OS=Homo sapiens OX=9606 GN=TGFBI PE=1 SV=1	-0.943	0.010
ATPB_HUMAN ATP synthase subunit beta, mitochondrial OS=Homo sapiens OX=9606 GN=ATP5F1B PE=1 SV=3	-0.678	0.010
IPYR2_HUMAN Inorganic pyrophosphatase 2, mitochondrial OS=Homo sapiens OX=9606 GN=PPA2 PE=1 SV=2	-0.627	0.010
NPS3A_HUMAN Protein NipSnap homolog 3A OS=Homo sapiens OX=9606 GN=NIPSNAP3A PE=1 SV=2	-0.474	0.010
CDIPT_HUMAN CDP-diacylglycerol--inositol 3-phosphatidyltransferase OS=Homo sapiens OX=9606 GN=CDIPT PE=1 SV=1	-0.831	0.011
LMNA_HUMAN Prelamin-A/C OS=Homo sapiens OX=9606 GN=LMNA PE=1 SV=1	-1.264	0.011
SEP11_HUMAN Septin-11 OS=Homo sapiens OX=9606 GN=SEPT11 PE=1 SV=3	-0.660	0.011
SGCD_HUMAN Delta-sarcoglycan OS=Homo sapiens OX=9606 GN=SGCD PE=1 SV=2	-1.025	0.011
PCYOX_HUMAN Prenylcysteine oxidase 1 OS=Homo sapiens OX=9606 GN=PCYOX1 PE=1 SV=3	-0.532	0.011
SMD3_HUMAN Small nuclear ribonucleoprotein Sm D3 OS=Homo sapiens OX=9606 GN=SNRPD3 PE=1 SV=1	-0.756	0.011
IF4A3_HUMAN Eukaryotic initiation factor 4A-III OS=Homo sapiens OX=9606 GN=EIF4A3 PE=1 SV=4	-1.153	0.012
CAVN1_HUMAN Caveolae-associated protein 1 OS=Homo sapiens OX=9606 GN=CAVIN1 PE=1 SV=1	-0.867	0.012
EF1B_HUMAN Elongation factor 1-beta OS=Homo sapiens OX=9606 GN=EEF1B2 PE=1 SV=3	-1.150	0.012
CYBR1_HUMAN Cytochrome b reductase 1 OS=Homo sapiens OX=9606 GN=CYBRD1 PE=1 SV=1	-0.993	0.012
LAMB2_HUMAN Laminin subunit beta-2 OS=Homo sapiens OX=9606 GN=LAMB2 PE=1 SV=2	-0.810	0.013
EF1G_HUMAN Elongation factor 1-gamma OS=Homo sapiens OX=9606 GN=EEF1G PE=1 SV=3	-0.554	0.013
HSP76_HUMAN Heat shock 70 kDa protein 6 OS=Homo sapiens OX=9606 GN=HSPA6 PE=1 SV=2	-0.751	0.013
OLFL3_HUMAN Olfactomedin-like protein 3 OS=Homo sapiens OX=9606 GN=OLFML3 PE=2 SV=1	-0.660	0.013
VAT1_HUMAN Synaptic vesicle membrane protein VAT-1 homolog OS=Homo sapiens OX=9606 GN=VAT1 PE=1 SV=2	-0.506	0.013
TPM2_HUMAN Tropomyosin beta chain OS=Homo sapiens OX=9606 GN=TPM2 PE=1 SV=1	-1.212	0.013
QCR9_HUMAN Cytochrome b-c1 complex subunit 9 OS=Homo sapiens OX=9606 GN=UQCR10 PE=1 SV=3	-0.920	0.013
NEUA_HUMAN N-acylneuraminate cytidylyltransferase OS=Homo sapiens OX=9606 GN=CMAS PE=1 SV=2	-0.914	0.013
HP1B3_HUMAN Heterochromatin protein 1-binding protein 3 OS=Homo sapiens OX=9606 GN=HP1BP3 PE=1 SV=1	-0.828	0.015
TPM1_HUMAN Tropomyosin alpha-1 chain OS=Homo sapiens OX=9606 GN=TPM1 PE=1 SV=2	-0.888	0.015

H4_HUMAN Histone H4 OS=Homo sapiens OX=9606 GN=HIST1H4A PE=1 SV=2	-1.100	0.016
MYH11_HUMAN Myosin-11 OS=Homo sapiens OX=9606 GN=MYH11 PE=1 SV=3	-1.476	0.016
NONO_HUMAN Non-POU domain-containing octamer-binding protein OS=Homo sapiens OX=9606 GN=NONO PE=1 SV=4	-0.852	0.017
LUM_HUMAN Lumican OS=Homo sapiens OX=9606 GN=LUM PE=1 SV=2	-0.606	0.018
PLEC_HUMAN Plectin OS=Homo sapiens OX=9606 GN=PLEC PE=1 SV=3	-0.529	0.019
METK2_HUMAN S-adenosylmethionine synthase isoform type-2 OS=Homo sapiens OX=9606 GN=MAT2A PE=1 SV=1	-1.196	0.019
TMED4_HUMAN Transmembrane emp24 domain-containing protein 4 OS=Homo sapiens OX=9606 GN=TMED4 PE=1 SV=1	-0.684	0.019
VINC_HUMAN Vinculin OS=Homo sapiens OX=9606 GN=VCL PE=1 SV=4	-0.574	0.020
LAP2B_HUMAN Lamina-associated polypeptide 2, isoforms beta/gamma OS=Homo sapiens OX=9606 GN=TMPO PE=1 SV=2	-1.027	0.020
ITA5_HUMAN Integrin alpha-5 OS=Homo sapiens OX=9606 GN=ITGA5 PE=1 SV=2	-0.516	0.021
HSPB1_HUMAN Heat shock protein beta-1 OS=Homo sapiens OX=9606 GN=HSPB1 PE=1 SV=2	-0.593	0.021
LYRIC_HUMAN Protein LYRIC OS=Homo sapiens OX=9606 GN=MTDH PE=1 SV=2	-0.641	0.022
PRDX3_HUMAN Thioredoxin-dependent peroxide reductase, mitochondrial OS=Homo sapiens OX=9606 GN=PRDX3 PE=1 SV=3	-0.755	0.022
AT5F1_HUMAN ATP synthase F(0) complex subunit B1, mitochondrial OS=Homo sapiens OX=9606 GN=ATP5PB PE=1 SV=2	-0.774	0.022
ACTBL_HUMAN Beta-actin-like protein 2 OS=Homo sapiens OX=9606 GN=ACTBL2 PE=1 SV=2	-0.630	0.022
VITRN_HUMAN Vitrin OS=Homo sapiens OX=9606 GN=VIT PE=2 SV=1	-0.770	0.023
DERM_HUMAN Dermatopontin OS=Homo sapiens OX=9606 GN=DPT PE=1 SV=2	-0.628	0.024
RBBP4_HUMAN Histone-binding protein RBBP4 OS=Homo sapiens OX=9606 GN=RBBP4 PE=1 SV=3	-0.485	0.024
LEMD2_HUMAN LEM domain-containing protein 2 OS=Homo sapiens OX=9606 GN=LEMD2 PE=1 SV=1	-0.488	0.025
CO4A2_HUMAN Collagen alpha-2(IV) chain OS=Homo sapiens OX=9606 GN=COL4A2 PE=1 SV=4	-1.239	0.025
PGRC2_HUMAN Membrane-associated progesterone receptor component 2 OS=Homo sapiens OX=9606 GN=PGRMC2 PE=1 SV=1	-0.731	0.026
DDX17_HUMAN Probable ATP-dependent RNA helicase DDX17 OS=Homo sapiens OX=9606 GN=DDX17 PE=1 SV=2	-0.471	0.027
MFS10_HUMAN Major facilitator superfamily domain-containing protein 10 OS=Homo sapiens OX=9606 GN=MFSD10 PE=1 SV=1	-0.871	0.028
SODM_HUMAN Superoxide dismutase [Mn], mitochondrial OS=Homo sapiens OX=9606 GN=SOD2 PE=1 SV=3	-0.713	0.028
CH10_HUMAN 10 kDa heat shock protein, mitochondrial OS=Homo sapiens OX=9606 GN=HSPE1 PE=1 SV=2	-0.489	0.028
CNDP2_HUMAN Cytosolic non-specific dipeptidase OS=Homo sapiens OX=9606 GN=CNDP2 PE=1 SV=2	-0.433	0.028
PGRC1_HUMAN Membrane-associated progesterone receptor component 1 OS=Homo sapiens OX=9606 GN=PGRMC1 PE=1 SV=3	-0.731	0.032
ATPO_HUMAN ATP synthase subunit O, mitochondrial OS=Homo sapiens OX=9606 GN=ATP5PO PE=1 SV=1	-0.655	0.032
SEPT7_HUMAN Septin-7 OS=Homo sapiens OX=9606 GN=SEPT7 PE=1 SV=2	-0.600	0.033
LEG1_HUMAN Galectin-1 OS=Homo sapiens OX=9606 GN=LGALS1 PE=1 SV=2	-0.576	0.033
ACON_HUMAN Aconitate hydratase, mitochondrial OS=Homo sapiens OX=9606 GN=ACO2 PE=1 SV=2	-0.766	0.034

AMBP_HUMAN Protein AMBP OS=Homo sapiens OX=9606 GN=AMBP PE=1 SV=1	-0.779	0.035
SCMC1_HUMAN Calcium-binding mitochondrial carrier protein SCaMC-1 OS=Homo sapiens OX=9606 GN=SLC25A24 PE=1 SV=2	-0.625	0.036
AOFB_HUMAN Amine oxidase [flavin-containing] B OS=Homo sapiens OX=9606 GN=MAOB PE=1 SV=3	-0.939	0.036
SF3A1_HUMAN Splicing factor 3A subunit 1 OS=Homo sapiens OX=9606 GN=SF3A1 PE=1 SV=1	-0.718	0.036
ATP5L_HUMAN ATP synthase subunit g, mitochondrial OS=Homo sapiens OX=9606 GN=ATP5MG PE=1 SV=3	-0.750	0.038
TCPE_HUMAN T-complex protein 1 subunit epsilon OS=Homo sapiens OX=9606 GN=CCT5 PE=1 SV=1	-0.667	0.039
F162A_HUMAN Protein FAM162A OS=Homo sapiens OX=9606 GN=FAM162A PE=1 SV=2	-0.505	0.039
CALX_HUMAN Calnexin OS=Homo sapiens OX=9606 GN=CANX PE=1 SV=2	-0.568	0.040
HXK1_HUMAN Hexokinase-1 OS=Homo sapiens OX=9606 GN=HK1 PE=1 SV=3	-0.479	0.041
ACTN1_HUMAN Alpha-actinin-1 OS=Homo sapiens OX=9606 GN=ACTN1 PE=1 SV=2	-0.530	0.041
ADIPO_HUMAN Adiponectin OS=Homo sapiens OX=9606 GN=ADIPOQ PE=1 SV=1	-0.908	0.041
ILF3_HUMAN Interleukin enhancer-binding factor 3 OS=Homo sapiens OX=9606 GN=ILF3 PE=1 SV=3	-0.923	0.041
TPM4_HUMAN Tropomyosin alpha-4 chain OS=Homo sapiens OX=9606 GN=TPM4 PE=1 SV=3	-0.904	0.041
DHE3_HUMAN Glutamate dehydrogenase 1, mitochondrial OS=Homo sapiens OX=9606 GN=GLUD1 PE=1 SV=2	-0.862	0.041
ITA1_HUMAN Integrin alpha-1 OS=Homo sapiens OX=9606 GN=ITGA1 PE=1 SV=2	-0.722	0.041
PARVA_HUMAN Alpha-parvin OS=Homo sapiens OX=9606 GN=PARVA PE=1 SV=1	-0.509	0.044
TMX4_HUMAN Thioredoxin-related transmembrane protein 4 OS=Homo sapiens OX=9606 GN=TMX4 PE=1 SV=1	-0.975	0.046
KAD2_HUMAN Adenylate kinase 2, mitochondrial OS=Homo sapiens OX=9606 GN=AK2 PE=1 SV=2	-0.572	0.046
SFPQ_HUMAN Splicing factor, proline- and glutamine-rich OS=Homo sapiens OX=9606 GN=SFPQ PE=1 SV=2	-0.740	0.047
H2AV_HUMAN Histone H2A.V OS=Homo sapiens OX=9606 GN=H2AFV PE=1 SV=3	-0.680	0.047
MDHM_HUMAN Malate dehydrogenase, mitochondrial OS=Homo sapiens OX=9606 GN=MDH2 PE=1 SV=3	-0.625	0.047
1433T_HUMAN 14-3-3 protein theta OS=Homo sapiens OX=9606 GN=YWHAQ PE=1 SV=1	-0.376	0.047
GRP75_HUMAN Stress-70 protein, mitochondrial OS=Homo sapiens OX=9606 GN=HSPA9 PE=1 SV=2	-0.668	0.048
EF1D_HUMAN Elongation factor 1-delta OS=Homo sapiens OX=9606 GN=EEF1D PE=1 SV=5	-0.463	0.048
CAVN3_HUMAN Caveolae-associated protein 3 OS=Homo sapiens OX=9606 GN=CAVIN3 PE=1 SV=3	-0.738	0.048
RS3A_HUMAN 40S ribosomal protein S3a OS=Homo sapiens OX=9606 GN=RPS3A PE=1 SV=2	-0.666	0.048